Collision Processes of Low Charge Ions with Atoms in Fusion Plasma

Shi-Yang Zou

DOCTOR OF PHILOSOPHY

Department of Fusion Science
School of Mathematical and Physical Science
The Graduate University for Advanced Studies

2002(School Year)

To my wife, Yan, and our daughter, Qiushi

ACKNOWLEDGMENTS

I would like to express my gratitude to Professor Takako Kato (National Institute for Fusion Science) and Professor Mineo Kimura (Yamaguchi University) for their great patience and guidance on plasma spectroscopy and atomic physics.

I am also indebted to Dr. Lukáš Pichl (University of Aizu), Professor Takashi Fujimoto (Kyoto University) and Dr. Daiji Kato. Dr. Lukáš Pichl shared with me his knowledge on ion-atom collisions theory and provided much help on computation and scientific visualization. Professor Takashi Fujimoto taught me a lot on plasma spectroscopy. Dr. Daiji Kato (National Institute for Fusion Science) expressed his interest in my work and supplied me with numerous useful discussions and references.

My thanks are due to many people who have helped me in this research, particularly to Professor Katsumi Kondo (Kyoto University) and Professor Katsumi Ida (National Institute for Fusion Science) for the permission of using their spectral data and useful discussions, and to Professor Richard More (National Institute for Fusion Science) and Dr. Izumi Murakami (National Institute for Fusion Science) and Dr. Atsushi Iwamae (Kyoto University) for many useful discussions.

My thanks are also extended to all other members of Data and Planing Center of National Institute for Fusion Science for their help in my research, and to Mr. Katsuyuki Matsuura (National Institute for Fusion Science) and Ms. Masako Kishikawa (National Institute for Fusion Science) for their help during my stay in Japan.

The scholarship was awarded to me by the *Japan Society of Plasma Science and Nuclear Fusion Research* in the period of 2000-2002 and *Japanese Ministry of Education, Culture, Sports, Science and Technology* in the period of 2002-2003, was crucial to the successful completion of this project.

Finally, I wish to thank the following Drs. Norimasa Yamamoto (Rikkyo University), Wenbing Pei, Jinghong Li, Yuhong Xu and Mr. Beiwen Li (National Institute for Fusion Science) for their friendship.

ABSTRACT

Signature _____
Takako Kato, Ph.D.

Collision Processes of Low Charge Ions with Atoms in Fusion Plasma

Shi-Yang Zou , Ph.D.
The Graduate University for Advanced Studies

Collision processes of low charged ions with neutral atomic particles at low to intermediate energies play vital roles in various fields of applied physics such as plasma physics, astrophysics, and radiation physics. In ion-atom collisions, several inelastic processes can take place in addition to elastic scattering. Among these processes, excitation of target, electron capture, and ionization (the ejection of electrons from the target) are considered to be dominant in the energy range concerned fusion research. There is an amount of effort to fully understand the dynamics of ion-atom collisions from both the experimental and theoretical perspectives. As a result of these extensive experimental and theoretical investigations, most of the elastic and inelastic processes involving bound states of target and projectile ions are well described by current theories. However, ionization remains a challenge even for the most basic processes such as proton-hydrogen system especially at low energy. The discrepancy in ionization cross sections between two recent experiments [1, 2]* is as large as a factor of six. Reasonably reliable theoretical studies [3–5] predicted about 20% higher value

*Bracketed references placed superior to the line of text refer to the bibliography.

than those of experiments [6, 7] at the peak of ionization cross section, and there is a considerable disagreement among theoretical cross sections at low keV energies. The energy dependence of theoretical and experimental results are also different. In the present work, we have aimed to provide more insight into such unresolved problems.

Heavy-particle atomic collision is a complex quantum-mechanical problem. It involves interaction of many states both from the discrete and continuum parts of the energy spectrum and also strong couplings of many reaction channels. Obviously, the understanding of the collisional dynamics of ion-atom system would represent a considerable advance of our basic knowledge on atomic interactions, in general. Besides, this knowledge is essential for the understanding and interpretation of a large variety of phenomena taking part in many non-equilibrium plasmas. The importance of heavy-particle collisions in fusion research applications and the challenges for theory have motivated me to carry out this research.

In the first part of my research, I studied electron emission in H^++H(1s), He^{2+}+H(1s) and He^+(1s)+H^+ collisions at low energy (below 20 keV/amu), using the electron translation factor corrected molecular orbital close-coupling approach. Selection of the collision partners and energy range studied here ties closely with the application in fusion plasma experiments. Full convergence of ionization cross sections as a function of H_2^+ or HeH^{2+} molecular basis size was achieved by including up to twenty bound states, and more than three hundred continuum states. The results obtained by our calculation are compared with the available experimental data and various theoretical models. Excellent agreement with the recent experiments is found for the total ionization cross sections (TICS) where the experimental values are available. This study shows that for the ionization in He^{2+}+H(1s) and/or He^+(1s)+H^+ collisions, the higher-level ladder climbing processes (i.e. excitation via a sequence of upper levels) are dominant as compared to direct mechanism, in which the electron is liberated by one step promotion. On the contrary, in the H^++H(1s) collision process, H(1s) is ionized directly, and the higher levels, especially $2p\pi_u$, act as a temporary trap of the ionization flux.

The second part of this thesis is devoted to the calculation of spectral profiles of Li^{2+} ions emitted in magnetically confined plasma. In magnetic confined plasmas, Li^{2+} ions are populated by three kinds of mechanism; excitation from the ground state, electron-ion recombination from Li^{3+} and charge exchange with neutral hydrogen and

Li^{3+}. The nl-resolved population densities of exited Li^{2+} ions are calculated up to $n = 20$ using a collisional-radiative model including the charge exchange process. Since reliable cross sections for charge exchange processes in Li^{3+}+H(1s) collision are available, instead of attempting recalculations of charge transfer process, I adopt them from the recent literatures. In the calculation, the radiative transition probabilities and wavelengths of Li^{2+} ions are computed by diagonalizing the Hamiltonian including interactions with the magnetic field. This study shows that 1) spectral profiles emitted by excitation, recombination and charge exchange are quite different from each other, which is due to the different n and l-distributions of the rate coefficients of such basic atomic processes (i.e. excitation, recombination and charge exchange); and 2) in order to interpret properly low temperature spectra, the Zeeman effect has to be accounted for, especially for ion temperature diagnostics.

In summary, I have treated heavy-particle atomic collisions which are typical in plasma, obtaining new cross sections for charge transfer, excitation and ionization at low energies. The detailed discussions are made to collisions involving the partially or fully ionized main component of fusion plasmas (hydrogen and helium). Based on a detailed computation for spectral profiles of Li^{2+} ions, I have analyzed the spectra of hydrogen-like lithium measured from magnetic confinement fusion plasmas.

TABLE OF CONTENTS

1.0 Introduction

The collision processes of lowly charged ions with neutral atomic particles have challenged theoretical and experimental physicists for nearly seventy years. The constant interest in ion-atom collision processes is motivated both by the fundamental and practical reasons.

The heavy-particle atomic collision is an extremely complex quantum-mechanical problem. It involves interaction of many states both from the discrete and continuum parts of the energy spectrum and includes strong couplings of many reaction channels. Obviously, the understanding of the collisional dynamics of ion-atom system would represent a considerable advance of our basic knowledge on atomic interactions, in general. Besides, this knowledge is very much at the heart of a large number of application in such areas as magnetically or inertially confined fusion plasmas, laser systems, partially ionized gases and plasmas, chemical systems, surface interactions, channelling and energy loss in solids, energy and ionization balance in the earth's atmosphere, astrophysical studies on a broad front, and a host of other examples (see, e.g., Refs. [8–10] and references therein).

These important applications and other issues of interest continue to capture the attention of experimental and theoretical physicists, and keep the field instantaneously developing. As a result of extensive experimental and theoretical investigations, most of the elastic and inelastic processes involving bound states of target and projectile ions are well understood by current methods. However, the ionization remains a challenge even for the most basic processes such as proton-hydrogen system especially at low energy. At keV energies, the total ionization cross sections obtained by experimental studies of Pieksma *et al.* [2] were found to be quite larger than the recent measurements of Shah *et al.* [1] below 10 keV/amu, and to decrease much less rapidly with the energy decrease. At the lowest energy considered (1 keV/amu), the cross sections of Pieksma*et al* [2] exceed the values by Shah [1] by ~ 6 times. Numbers from experiments [6,7] and recent theoretical studies[3–5] disagree by 20% at the peak of ionization cross section. In the present work, we have provided more insight into the previously unresolved problems.

Before moving on to the details of my research, it is a suitable point to briefly describe some important applications of heavy-particle atomic collisions as illustra-

tions, and summarize the experimental and theoretical methods for investigations of lowly charged ion-neutral atomic particle collision processes[1].

1.1 Important applications of heavy-particle atomic collisions

Several areas of research, bringing important practical implications, have constantly stimulated particular investigations of low charged ion collision processes. Among the various applications of heavy-particle atomic collisions, the controlled thermonuclear fusion programme certainly has the dominant place. Controlled thermonuclear fusion for the isotopes of hydrogen in a high temperature plasma offers the prospect of a major source of energy with low environmental impact and virtually inexhaustible supplies of fuel. Over the past few decades a steady progress was seen towards practical realization based on schemes in which the plasma is heated during magnetic confinement. Attention has also been directed towards heating and inertial confinement by energetic laser or particle beams. While both these general approaches involve many atomic physics problems [11–14], in this thesis the scopes will be limited to aspects of magnetic confinement fusion.

Presently, neutral beam injection (NBI) has evolved to a very reliable heating technique operating successfully at almost all major fusion experiments. For heating by hydrogen neutral beams, the fast hydrogen atoms pass through the magnetic confining fields and undergo electron removal in collisions with the plasma constituents. Charge transfer

$$H^+ + H \rightarrow H + H^+ \tag{1-1}$$

and ionization

$$H^+ + H \rightarrow H^+ + H^+ + e \tag{1-2}$$

in collisions with plasma protons are important in this context. The resulting fast protons are then trapped in the confining field and give up their energy in further collisions with the plasma constitutes.

[1]Although the D and T isotopes of hydrogen are of great relevance than H in fusion research, most experimental measurements have been made with ions or atoms of H. For this reason and, since isotope effects do not arise for most of the processes considered, reference will generally be made to H in this discussion

The effectiveness of neutral beam heating can be strongly influenced by collisions with multiply charged impurity ions. High values of cross sections for both charge transfer

$$X^{q+} + H \rightarrow X^{(q-1)+} + H^{+} \tag{1-3}$$

and ionization

$$X^{q+} + H \rightarrow X^{q+} + H^{+} + e \tag{1-4}$$

can seriously modify the energy deposition profiles. In addition, electron capture into high n states which then decay radiatively can lead to substantial cooling of plasma, which is undesirable.

There is another aspect of the thermonuclear fusion programme, which is concerned with low charged ion-neutral atom collision processes. Power and particle control are the most promising concepts in magnetic confinement fusion experiments, which rely upon atomic processes to transfer the power and momentum from the plasma edge to the plasma facing components [15]. The symmetrical resonant charge transfer processes such as $H^{+} - H$ collisions are of particular importance in edge plasmas modelling, since they have large cross sections in the ~1 eV - 500 eV energy range of interest. Moderately exothermic charge transfer processes involving partially ionized impurity ions may also take place very effectively through curve crossing leading to the selective population of a limited number of excited states. Excited product states decay radiatively, and thereby cool the plasma. In present devices, additional magnetic fields allow the edge plasma to flow into the divertor region where it undergoes neutralization in collision with the divertor plates. The resulting neutrals are either pumped away or undergo further collisions. Charge transfer and ionization collisions are important in determining the degree of recycling of hydrogen and other species together with associated energy losses.

In further connection with the controlled thermonuclear fusion research, let us also mention the charge exchange recombination spectroscopy (CXRS). In this technique, which has been used extensively with both H heating beams and dedicated H probes [16] for diagnostics of fully ionized species (e.g. He^{2+}, C^{6+}, O^{8+}), spectroscopic observations are made of the decay of the H-like excited products formed by the state selective electron capture,

$$X^{z+} + H \rightarrow X^{(z-1)+}(n, l) + H^{+}. \tag{1-5}$$

Local ion densities, ion temperatures and plasma rotational velocities can be deduced from studies of the Doppler-broadened line profiles. In combination with the impurity pellet injection, CXRS has been extended to a study of particle transport in magnetically confined plasmas. As an example of such approach, Khlopenkov et al [17] have used the tracer-encapsulated solid pellet (TESPEL), the lithium hydride tracer covered by polystyrene ($(C_8H_8)_n$), to measure the diffusion coefficient of light impurities on a middle size device (i.e. the Compact Helical System (CHS)).

Another important practical motivation for the active study of ion-atom collision processes is the search for powerful lasers in the EUV and soft X-ray regions [18–20]. Line emission in these spectral regions can be produced by electronic transitions in the excited highly charged ions. The charge exchange process between ions and a neutral atom leading to a preferential population of highly excited levels, has been proposed as an effective mechanism for creation of inverted population. However, to obtain stimulated radiation in the EUV and X-ray regions one needs a very high density of excited particles. Within the ion beam approach to the problem, it is very difficult to achieve such densities. In plasmas produced by high power laser radiation, however, it is relatively easier to obtain the necessary density of inverted population [21]. The inverted populations of C^{5+} ion in capillary discharge [22] and N^{6+} ion in Z-pinches [23] were also reported, and the pump mechanism was attributed to the charge exchange reactions between the strong plasma jets (from pinch instabilities) and the lower charged residual plasma.

1.2 Experimental methods for studies of collisions involving H atoms

A brief summary of the main experimental techniques used in collision studies involving H atoms is appropriate since, unlike stable gases such as H_2 or He, well characterized targets of atomic hydrogen have had to be specially developed to facilitate accurate cross section measurements. Few of the measurements are absolute and most rely on normalization of relative cross sections to other data. The main techniques are:

1. *Crossed beam methods employing highly dissociated thermal energy hydrogen beams.*

The modulated crossed beam technique pioneered by Fite et al [24] provided most of the early data on charge transfer and ionization but the accuracy is severely limited by poor signal to background ratios. The crossed beam coincidence counting technique incorporating time of flight (TOF) spectroscopy developed by Shah and Gilboday [6] provides high sensitivity and accuracy. Studies of electron capture into excited states in $X^{q+} - H$ collisions have been carried out by using photon emission spectroscopy (PES), first by Ciric et al [25] with intense ion beams and hydrogen beams of high density from the Wood's tube discharge source. While of low sensitivity, the method provides results of moderate to high accuracy.

2. *Furnace target methods*

   In this approach, first used by Lockwood and Everhart [26], the primary ion beam is passed through highly dissociated hydrogen contained within a tungsten tube furnace. Many measurements of total electron capture cross sections have since then been based on this approach. Energy loss studies by Park et al [27] have provided data on direct excitation and ionization of H while translational energy spectroscopy (TES) (involving measurements of either energy gain or loss), first used by McCullough et al [28], has provided data on state-selected electron capture in $X^{q+} - H$ collisions.

3. *Fast intersecting beam methods*

   In this approach, a target beam of fast H atoms, usually produced by electron capture neutralization of an H^+ beam, is arranged to collide with the primary ion beam in an ultra-high vacuum region. While the use of keV energy beams facilitates collision product detection through particle counting, low signal levels and high signal to background ratios make such measurements difficult. Account must also be taken of the excited state population of the H atoms. Kim and Meyer [29] arranged the beams to control the H(n) state populations. Several experiments using a merged beam configuration have provided data for collision at very low c.m. energies. These include measurements by Newman et al. [30] of $H^+ - H(1s)$ charge transfer down to c.m. energies of 0.1 eV and studies by Koch and Rayfield [31] of electron removal in $H^+ - H(n)$ collisions for $n = 44$ to 50 in the c.m. energy range 0.4-61 eV.

1.3 Theoretical methods for studies of heavy-particle atomic collisions

Historically, the theoretical tool box used to study heavy-particle atomic collisions was divided into two broad compartments,

1. close-coupling methods based on an expansion of the wavefunction in terms of a set of functions chosen to describe the electronic coordinates of the colliding atomic systems, and

2. perturbartive methods such as a truncated Born series.

The first approach was generally believed to be valid for *low- to intermediate-energy collisions* (i.e. $v \leq v_{el}$ where v is the collision velocity and v_{el} is the electron orbital velocity), and the second for *high energy collisions* (i.e. $v \gg v_{el}$). In high-energy, heavy-particle collisions, ionization is generally the dominant channel, followed by target excitation processes. In contrast, in low- to intermediate-energy heavy-particle collisions, it is not possible to single out a dominant channel in general, because often many inelastic channels strongly couple with one another, exchanging flux and phase in a complex manner. As just one illustration, the major inelastic cross sections in $H + H^+$ collisions are shown in Fig. 1.1. It is apparent that certain electron capture, excitation, and ionization cross sections have the same magnitude at $E \geq 5$ keV, so that one process can be expected to significantly influence the others. Thus, without simultaneous inclusion of all important channels, an accurate determination of the transition probabilities is impossible. This is where non-perturbative scheme such as close-coupling method is indispensable.

The theoretical methods commonly used to study heavy-particle atomic collisions and the connections between them are given in Fig.1.2. It is not my intention to discuss the details of various theoretical models for ion-atom collisions here, but rather to refer the readers to the excellent review article on the topic by Kimura and Lane [8], and also the monograph of Bransden and McDowell [32]. The strengths and weakness of these methods were reviewed there. In the present thesis, I will focus particularly on the ionization processes in H^++H(1s) and He^{2+}+H(1s) collisions at low energies, and the spectroscopy of Li^{2+} ions in a magnetically confined fusion plasma.

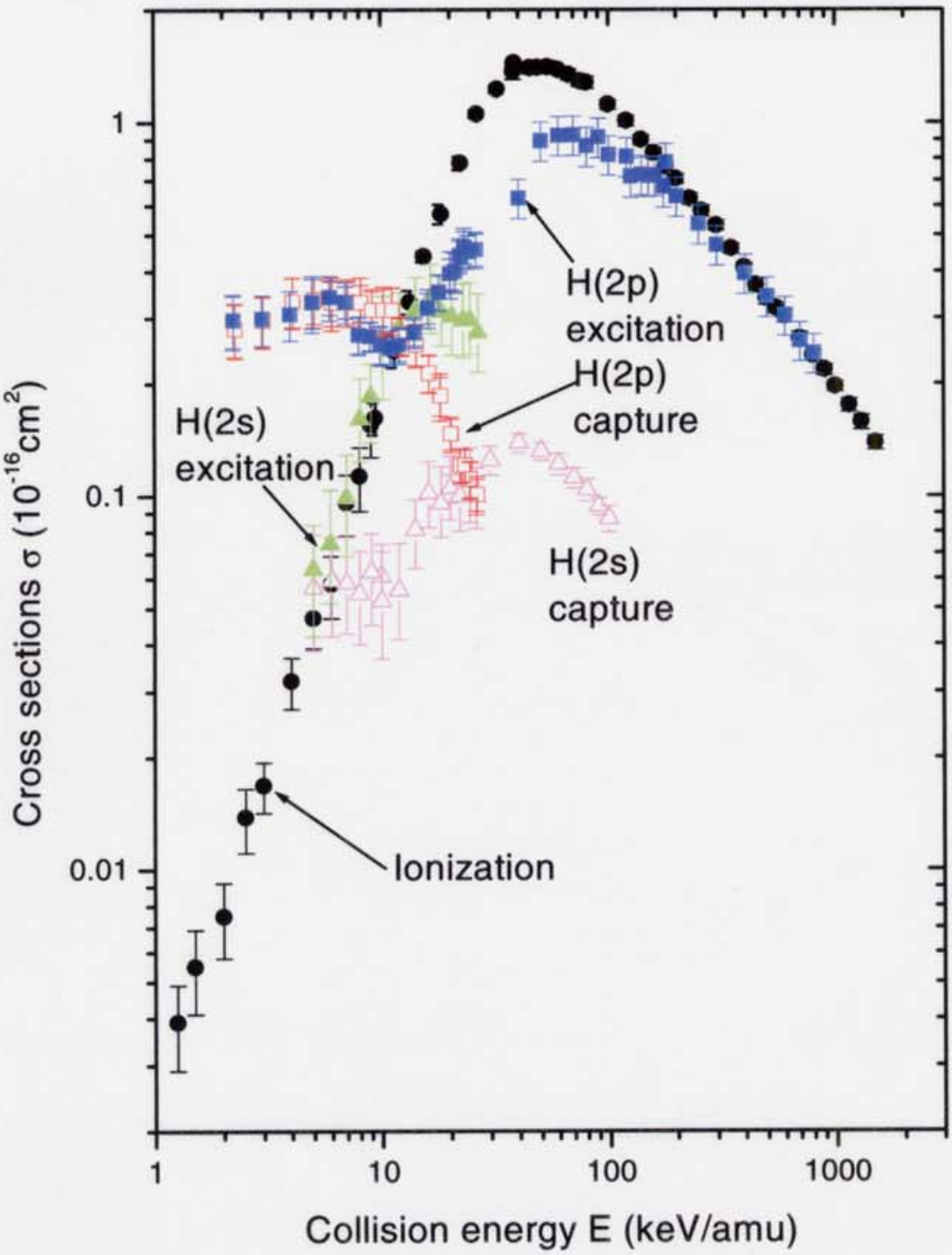

Figure 1.1 Major inelastic cross sections in $H + H^+$.

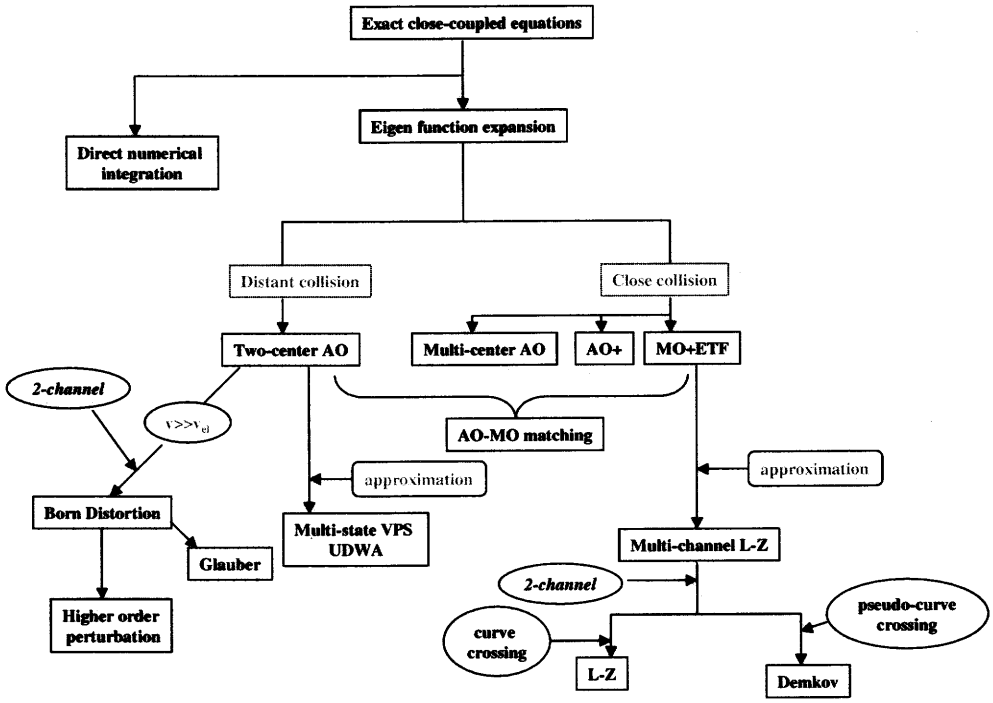

Figure 1.2 Schematic outline illustrating relations among the major theoretical models which are commonly used in ion-atom collision investigations [8]. AO: atomic orbital close-coupling proposed by Bates [33]; AO+: atomic orbital plus pseudo states close-coupling firstly proposed by Fritsch and Lin [34]; MO: molecular orbital close-coupling originally proposed by Massey and Smith [35]; ETF: electron translation factor [36]; AO-MO matching: atomic orbital- molecular orbital matching method, which is originally proposed by Kimura and Lin [37, 38], and Winter and Lane [39] L-Z: Landau-Zener model [40, 41]; Demkov: Demkov model [42]; UDWA: unitarized distorted wave approximation [43–46]; VPS: Vainstein-Presnyakov-Sobel'man method proposed by Vainshtein *et al.* [47, 48].

To give a concise guide, the structure of this thesis is summarized below. In the first part of my research, I have carried out the study on the electron emission in H^++H(1s), He^{2+}+H(1s) and He^+(1s)+H^+ collisions at low energy range (below 20 keV/amu), using the electron translation factor corrected molecular orbital close-coupling approach. Selection of the collision partners and energy range studied here ties closely with the application in fusion plasma experiments. Full convergence of ionization cross sections as a function of H_2^+ or HeH^{2+} molecular basis size was achieved by including up to twenty bound states, and more than three hundred continuum states. The present results are compared with the available experimental data and various theoretical models. An excellent agreement with the recent experiments is found for the processes where the experimental values are available. This study shows that in the ionization in He^{2+}+H(1s) and/or He^+(1s)+H^+ collisions, higher-level ladder climbing processes (i.e. excitation via a sequence of upper levels) are dominant than a direct mechanism (i.e. electron is liberated by one step promotion). On the contrary, for the ionization in H^++H(1s), H(1s) is ionized directly, and the higher levels, especially $2p\pi_u$, act as a temporary trap of the flux.

The second part of this thesis devotes to calculation of the spectral profiles of Li^{2+} ions emitted in magnetically confined plasma, where the excited Li^{2+} ions are populated by excitation from the ground state, electron-ion recombination from Li^{3+}, and charge exchange with neutral hydrogen and Li^{3+}. The nl-resolved population densities of exited Li^{2+} ions are calculated up to $n = 20$ using a collisional-radiative model including the charge exchange process. As the reliable cross sections for charge exchange processes in Li^{3+}+H(1s) collision are already available, we adopt them from the recent literatures. In the calculation, the radiative transition probabilities and wavelengths of Li^{2+} ions are computed by diagonalizing the Hamiltonian including interactions with the magnetic field. This study shows that 1) spectral profiles emitted by excitation, recombination and charge exchange are quite different from each other, which is due to the different n and l-distributions of the rate coefficients of these basic atomic processes (i.e. excitation, recombination and charge exchange); and 2) in order to interpret properly low temperature spectra, the Zeeman effect has to be accounted for, especially for ion temperature diagnostics.

PART I

Ionization in Low Energy Ion-Atom Collisions

2.0 Ionization: Current Status in Slow Ion-atom Collisions

In a collision of an ion with a neutral atom or molecule, the atomic process that involves the largest transfer of energy is ionization or, more specifically, the ejection of a free electron from the target. This process accounts for a large fraction of the energy loss of ions in materials. In such diverse fields as radiation damage and radiation biology, studies of the interaction of solar wind with the upper atmosphere, magnetic and inertial confinement fusion studies, plasma physics, and stellar physics, data on the cross sections for ionization of various targets are necessary. This process is the main subject of the first part of the thesis.

2.1 Experimental studies of ionization in slow ion-atom collisions

Comparing to numerous theoretical works for describing the ionization of atomic hydrogen by H^+ and/or He^{2+} ions,

$$H^+ + H(1s) \rightarrow H^+ + H^+ + e \tag{2-1}$$

$$He^{2+} + H(1s) \rightarrow He^{2+} + H^+ + e \tag{2-2}$$

only few experiments were performed over the past decades. That is because the $H^+ - H$ and/or $He^{2+} + H$ systems are difficult for experimental investigation due to the problems in making and characterizing the atomic hydrogen target[10]. At low energies, the difficulty also comes from making and controlling high current and low velocity proton (and/or α-particle) beams.

The pioneering experiments due to Fite *et al.* [49] measured the ionization cross section at 0.04-40 keV/amu, using the modulated crossed-beam technique. Protons in beam were arranged to intersect a thermal energy beam of highly dissociated hydrogen from a tungsten tube furnace source. By chopping the beam at fixed frequency, signals arising from the process in question could be distinguished from those arising from collisions in the background gas by their specific frequency and phase. The measurements provided the ratio of the cross sections in H to those in H_2. Cross sections for Eq. (2-1) were determined by reference to the sum of previously measured

cross sections for charge transfer and ionization in $H^+ + H_2$ collisions. Yet the results of Ref. [49] were found considerable higher than the general accepted data of Ref. [7]. Measurements based on the modulated crossed-beam technique have also been carried out by Gilbody and Ireland [50] in the energy range 50-400 keV. In this case, cross sections for Eq. (2-1) were determined by reference to known cross sections for the ionization of H_2 by proton impact.

The first experimental studies of differential cross section in collision (2-1) due to Park *et al* were based on an analysis of the differential energy-loss spectra in the passage of protons through highly dissociated hydrogen within a tungsten tube furnace. Cross sections in the energy range 25-200 keV were normalized to the theoretical estimates of the cross section for excitation of the $n = 2$ states of H by proton impact.

A crossed-beam method incorporating time-of-flight analysis and coincidence counting of the collision products was firstly used by Shah and Gilbody [6] to study $H^+ + H$ ionization in the intermediate- to high energy region. Cross sections obtained in the energy range 38-1500 keV were declared with very small experimental uncertainties. In their experiments, a momentum-analyzed beam of protons from an accelerator adjustable in energy 38-1500 keV (in 1998, 1.25 keV was reached as the bottom limit) was arranged to intersect (at right angles) in a high vacuum region a thermal energy beam of highly dissociated hydrogen. Slow ions and electrons formed as collision products in the crossed beam region were extracted by transverse electric field and separately counted by particle multipliers. Product H^+ ions arising from collisions with H_2 or other background gas species were recognized by their characteristic times of flight to multiplier. The required H^+ ions from the ionization process (1-2) could be distinguished from those arising from the charge transfer process

$$H^+ + H \rightarrow H + H^+ \tag{2-3}$$

by counting the H^+ ions with the electrons from the same ionizing events. Later, this approach was extended by Shah *et al.* to low [1] (1.25-9.4 keV) and intermediate [7] (9-95 keV) energy region. Cross sections for ionization (2-1) obtained in the wide energy range, about 1.25-1500 keV, with very small experimental uncertainties, have, for the first time, allowed a detailed appraisal of theoretical predictions. The same approach was also used by Shah and Gilbody [6] and Shah *et al.* [51] to study ionization process in $He^{2+} + H$ collisions. Cross sections obtained in the wide energy range, 18.4-2200 keV/amu, were found with very small experimental uncertainties again.

Experimental studies by Pieksma *et al.* [2], focusing on the identification of saddle-point electrons, produced the total ionization cross sections at 1-6 keV/amu, which were found to follow a v^2 dependence on the collision velocity near the threshold [52]. In the experiments, a pulsed stabilized proton beam is crossed with a partially dissociated thermal hydrogen beam. The atomic hydrogen beam is produced by a RF discharge source. Electrons are detected by means of a magnetic time-of-flight (TOF) spectrometer, which can collect essentially all electrons ejected in the forward hemisphere as long as the approximate transmission condition $k \sin\theta \leq 0.42$(a.u.) is satisfied, where k is the electron velocity and θ is the ejection angle with respect to the symmetry axis of the spectrometer. As an example, for $\theta = 90^o$ electrons with energies up to 2.4 eV are collected; for $\theta = 30^o$ this shifts to 9.6 eV. The RF source in use caused a severe background of slow electrons appearing as a constant term in the recorded TOF distributions, which was suppressed by subtracting the TOF measured with RF source switched off. However, a complete suppression was considered to be impossible [2]. Further, the difference spectrum is corrected for the constant background of uncorrelated RF source electrons. In addition, the electron spectrum of ionizing $H^+ - H_2$ collisions has to be corrected for. Integrating over the ejected electron velocity, total ionization cross sections are then obtained, which were found to be two times higher than that of ref. [1] at 6 keV/amu, and to decrease much more rapidly with energy decreasing. The discrepancy between the values of Ref. [2] and [1] are as large as the factor of ~ 6 at the lowest energy considered (1 keV/amu).

The available experimental data for ionization (2-1) are summarized in Fig. 2.1 together with some theoretical calculations. It can be seen that the results of these experiments are only in very rough general accord. Thus the theoretical values play an important role to recommend a set of cross sections for applications and to understand the collision dynamics.

Besides, the ejected electron energy, momentum and/or angular distributions are highly interesting to clarify the role of saddle-point ionization. The "Saddle-point" ionization mechanism was firstly suggested by Olson *et al.* [57], in which electrons stranded on or near the saddle point of the electronic potential between the positive target ion and the receding projectile emerge with roughly half the projectile velocity. The subject is full of controversial issues. Early experiments, which measured the energy distribution of the electrons for proton collisions with helium atoms in the energy range of tens to hundreds of keV, drew conflicting conclusions [58–68]. The

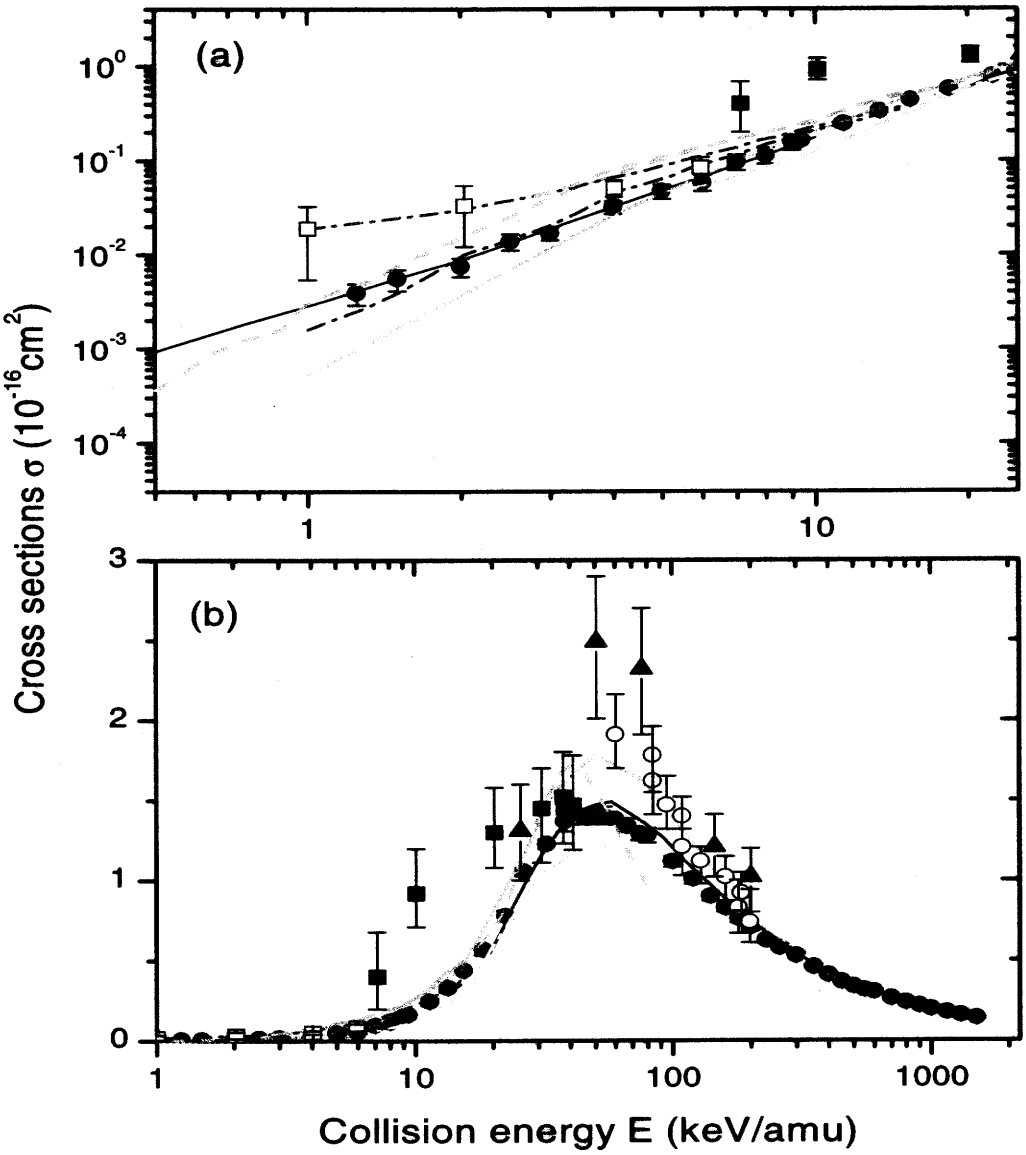

Figure 2.1 Total ionization cross sections of proton-hydrogen system: panels (a) and (b) are for low and high energy regions respectively. Solid squares, experiments of Fite *et al.* [49]; Open circles, experiments of Gilboday and Ierland [50]; Solid circles, experiments of Shah *et al.* [1,6,7]; Open squares, experiments of Pieksma *et al.* [2]; Blue dash-doted lines, hidden crossing with radial decoupling promotion mechanisms [52]; Red dash-dotted lines, hidden crossing results of without radial decoupling mechanisms [2]; Magenta dashed lines, 3CAO results of McLaughlin *et al.* [1,53]; Magenta dotted lines, 2CAO results of Toshima [4]; Cyen dash-dotted lines, 2CAO + pseudostate results of Fritsch and Lin [54]; Red solid lines, CDW-EIS results of Crothers and McCann [55] Black solid lines, MO results of Zou *et al.* [56]

controversy regarding the saddle-point electrons involved ion-atom collisions, where the projectile velocity was above the "matching" velocity (i.e., the average speed of the target's valence electron). Early quantum mechanical calculations [69] and the later ones [53, 70, 71] based on the triple-centered close-coupling approximation revealed the importance of describing the electron probability saddle point in the calculation of total ionization cross sections for ion-atom collisions involving projectile velocity below the matching velocity. Hidden crossing theory [2, 52] also predicts that saddle-point electrons comprise a large fraction of the total ionization cross section. However, the recent quantal calculations based on the numerical solving of Schrödinger in momentum space [3, 72, 73], and based on molecular-orbital close-coupling method with large scale basis sets[56], all show that the contribution from saddle-point emission to the total ionization is small even down to low keV energies. In the recent years, the novel technique of cold target recoil-ion momentum spectroscopy (COLTRIMS) allows experimentalists to map out the full momentum distributions of the ejected electrons. COLTRIMS experiments have been performed on helium or neon target with different projectiles [74–77], and the ejected-electron momentum distributions appear to depend strongly on the system studied. Recent reliable measurement [1] for the total ionization cross sections shows that saddle-point ionization is found not to be important down to 1.25 keV in $H^+ - H$ collision.

2.2 Theoretical studies of ionization in slow ion-atom collisions

The proton-hydrogen collisions, in particular for impact ionization, are a prototype of the break up of three charged particles, which has been extensively studied theoretically in the past decades (see Refs. [1, 3, 10, 56] and references therein). It is not my intention to discuss the numerous studies of proton-hydrogen collisions here, but rather to briefly describe some of the important works to show a simple map of this field.

The first attempt at calculating ionization cross sections in slow p-H collisions was performed by SethuRaman *et al.* [78]. They employed the electron translation factor (ETF) modified molecular orbital as zero-order basis to compute the first-order couplings, and then solved the system in the perturbation approximation. It

is a sensible thing to do if the cross section is small (*i.e.* if the coupling is weak). In such an approach, they calculated the energy distributions of ejected electron at collision energies 50-500 eV, but the total ionization cross sections were not presented. Later, Thorson and his coworkers [79–82] have studied extensively the base of ETF-modified molecular orbital close-coupling approach. They took into account suitable electron translation factors based on the molecular state switching functions in order to correct the asymptotic behavior of nonadiabatic couplings. Thorson *et al.* also gave a formulation of molecular basis close-coupling expansion, in which the flux loss from the truncated basis space has been accounted for. However, the observable quantities, total ionization cross sections, are still not presented by them.

Winter and Lin [69, 83] proposed a triple center atomic state expansion method for describing ionization at low energies. This method accounts for the mechanism in which the electron is not removed until it is asymptotically located at the point of unstable equilibrium between the nuclei (the third center-saddle point). Further, elaboration of the triple-center atomic orbitals method by McLaughlin *et al.* [53] showed a good agreement with the previous method of Ref. [69, 83] for all energies considered. Both these calculations predict values larger than the experimental cross sections of Refs. [1, 7], but the discrepancy is the smallest at the lowest energy region which they considered. The values obtained by Fritsch and Lin [54] in their double-center 46 atomic-state-plus-pseudostate (AO+) calculations (which were extended down to 4 keV/amu) were found to be smaller, on the opposite, but they also exhibit closer agreement with the experiment in the lowest energy region. Kuang and Lin further developed the two-center atomic orbital plus pseudostates expansion method [84, 85], ionization cross sections reported from them are $\sim$ 10% higher than the experimental data [6, 7] at maximum of ionization cross sections. Later, a very detailed study of the two-center atomic orbital expansion approach by Toshima [4] provided the ionization cross sections at the energy range 1-800 keV/amu, which were found to be 20% higher than the experiments of Shah *et al* [6, 7] at the peak of ionization cross section. In the three calculations above [4, 84, 85], motion of electron, in the double continuum of the target and the projectile, is represented by a large set of L^2 functions with positive eigenvalues, which may cause double-counting [86]. Recently two more calculations [3, 5] claimed that they are in good agreement with Toshima [4] and about 20% higher than the experimental values [6, 7] at the maximum. The cross sections from

Toshima [4] agree well with the measured data of Ref. [1] at energies 4-10 keV/amu, but decrease more rapidly than those of Ref. [1] below 4 keV/amu.

Pieksma *et al.* [2] calculated the velocity distributions of ejected electrons and total ionization cross sections based on the hidden-crossing model with the contributions from T-type crossing (connected with the saddle-point ionization mechanism) and S-type crossing (associated with the transition from quasi-molecular to united-atom behavior). In their work, the additional low-energy contributions from radial decoupling mechanism proposed by Ovchinnikov and Macek, which involve the decoupling of electron on nuclear motion within the united-atom limit, were also considered. At that time, the calculations of Pieksma *et al* came in below the available experimental data [2] and decreased more rapidly with the decreasing energy. Later, the contributions of radial decoupling mechanism were recalculated in a recent paper of Pieksma *et al* [52]. The new values include the contributions from this recalculated radial decoupling mechanism, and therefore they are in a better agreement with the experimental values of Ref. [2], but disagree with the more recent experimental data by Shah [1]. The cross section data in Ref. [1] decrease much more rapidly than those of Pieksma *et al*, both for the calculated [52] and measured [2] values, but agree well with the old version of hidden crossing calculations [2].

The one-electron ion-atom collision system $He^{2+} - H$ also captures many interests, which is the simplest asymmetric system. Total ionization cross sections of Winter [70] by triple-center atomic orbital expansion were found to agree well with the measured data[6, 51] above 40 keV/amu, but to decrease much slowly with the energy decreasing and to be higher by two times than that of Refs. [6, 51] at 18.4 keV/amu. The classical trajectory Monte Carlo simulation studies[57, 87–89] resulted a different peak position of ionization cross sections on incident energy. At low energy side ($v < 2$ a.u.), the ionization cross sections lie at the half of experimental values [6, 51]. Errea *et al.* proposed a triple-center molecular orbital expansion method for investigation of ionization of atoms by heavy particle, where the continuum states were represented by a set of Gaussian states center on the internuclear axis. Their results were found to be in good agreement with those of Shah *et al.* [6, 51], but to oscillate at $E \sim 10$ keV/amu. Hose [90] employed a multichannel perturbed-stationary-state propagator method to study the collision of $H(1s) + He^{2+}$. In his description, the continuum states are represented by the L^2 pseudostates of the linear combination of atomic

orbitals type. Ionization cross sections of Hose [90]were found to be less satisfactory compared to experimental data [6, 51].

Direct solution methods of the time-dependent Schrödinger equation for the electron system, but with the classical trajectory description of the nuclear motion, have also been used to investigate the ejected electron spectrum during ion-atom collision [73, 91]. However, their calculations provide mainly the momentum distribution of the ejected electron, and were done for the prototype proton-hydrogen system, whereas the momentum distribution experiments are only available for the multi-electron systems such as p+He or $p+H_2$ [74–77] due to the difficult in making H atom target. Thus a quantitative comparison between these calculations and experiment is not possible in present.

3.0 Molecular Orbital Close-Coupling Theory

Since the pioneering work of Bates *et al* [92] and Ferguson and McCarroll [93, 94], *molecular orbital* (MO) expansions have been employed in close-coupling processes, when the impact velocity v_p is regarded as small, relative to the orbital velocity of the active electron v_e. These MO wavefunctions are exact solutions for the Hamiltonian in which the nuclear motion is neglected. Hence, the relative motion of the nuclei is an perturbation causing the transition between *adiabatic* (or *stationary*) states. The extensive study of the MO method over past decades by several groups has demonstrated its applicability to a wide class of atomic collisions. It has been very successful in interpreting qualitatively (and *quantitatively*) various experimental findings.

The MO method, however, possesses an intrinsic problem, since the system scattering wavefunction is expanded in terms of adiabatic MOs, and does not generally satisfy the correct asymptotic boundary conditions, which specify (in the separated-atom limit) that the bound electron is moving either with the projectile or with the target. This translation motion of the electron is not accounted for in the conventional MO method (i.e., known as the *perturbed stationary state* (PSS) method [35]). It results in nonadiabatic coupling matrix elements which do not vanish asymptotically. Further, the resulting coupled equations are not Galilean invariant; i.e., they depend on the origin of the coordinates. To avoid these defects in the conventional MO method, 'electron translation factors (ETFs)' were first introduced by Bates and McCarroll [36]. In their description, each MO is assumed to translate exactly the same way as does its corresponding atomic orbital (AO) in the separated-atom limit, and the basis functions are chosen as

$$\Phi_j = \chi_j^{A,B} \exp\left(\mp i \frac{1}{2} \vec{v} \cdot \vec{r}\right) \exp\left[-i \int_0^t (\epsilon_j + \frac{1}{8} v^2) dt'\right] \tag{3-1}$$

However, this makes the basis function non-orthogonal, and while it is acceptable at large internuclear separations, where the electron is expected to be well localized around one or the other center, at short internuclear separations the electron motion has a molecular nature and each electron is shared by both nuclei.

To overcome this general criticism, the "molecular aspect" of electron motion has to be incorporated into the ETF. This can be done by constructing MO-ETF using the *local* propagation velocity for an electron in an molecular orbital [95]. Basing on

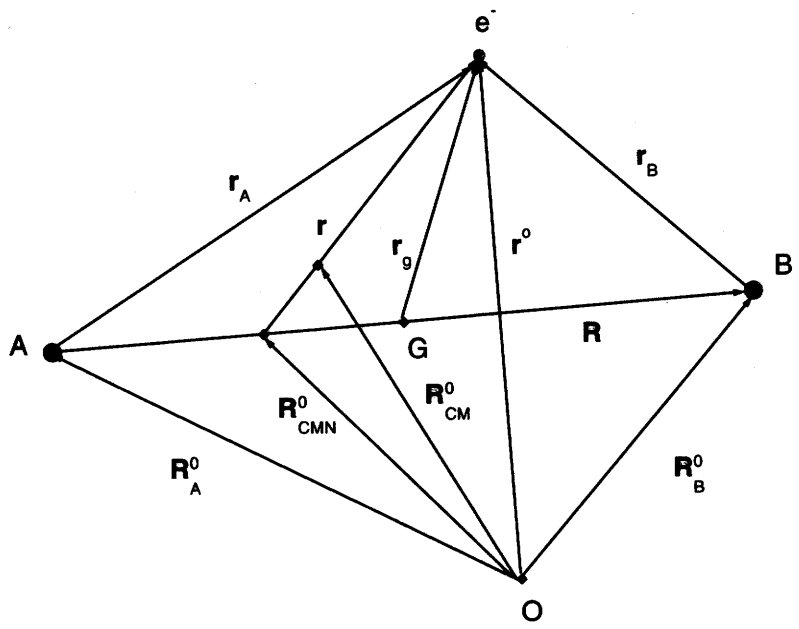

Figure 3.1 Coordinates for the one-electron-two nuclei system. O is an external origin. CMN is the center of mass of the two nuclei A and B. CM is the center of mass of the whole system. $\vec{r}_g$ is a vector from the geometric center (G) of the nuclei to the electron. It is assumed that $M_A > M_B$.

this idea, the theory of near-adiabatic (*slow*) collisions has been formulated by Delos, Thorson and others [80, 96], correctly taking into account the translational motion of electrons with the nuclei. A complete derivation of the coupled equations is presented in the review article by Delos [96]. Here I survey the main results to provide a simple, and I hope clear, relation between those equations and physics behind, with a loss of some rigor in the mathematical derivation.

3.1 Full quantum close-coupled equations

Consider the one-electron two-nuclei system described in Fig. 3.1, A is a projectile with charge Z_A and mass M_A, which collides with a target of charge Z_B and mass M_B, (in what follows I assume $M_A \geq M_B$). $\vec{R}$ is the nuclear coordinate taken from

A to B. The electronic coordinate can be chosen as $\vec{r}$, which connects the center of mass of the two nuclei with the electron, or $\vec{r}_g$, which connects the geometric center of the nuclei with the electron.

The total Hamiltonian for the two nuclei and one electron, after subtracting off the center of mass contribution, can be written in atomic units as

$$H = -\frac{1}{2\mu}\vec{\nabla}_R^2 - \frac{1}{2m}\nabla_r^2 - \frac{Z_A}{r_A} - \frac{Z_B}{r_B} + \frac{Z_A Z_B}{R} \tag{3-2}$$

where $\vec{\nabla}_r$ means the gradient with respect to $\vec{r}$ holding $\vec{R}$ fixed, and $\vec{\nabla}_R$ means a gradient with respect to $\vec{R}$ holding $\vec{r}$ fixed. The masses are defined by

$$\mu = \frac{M_A M_B}{M_A + M_B}$$

$$\frac{1}{m} = \frac{1}{m_e} + \frac{1}{M_A + M_B}$$

where m_e is the mass of electron, and r_i $(i = A, B)$ is the distance between the nucleus i and the electron. The Schrödinger equation takes the form

$$H\Psi(\vec{r}, \vec{R}) = E\Psi(\vec{r}, \vec{R}) \tag{3-3}$$

and the wave function Ψ can be expanded in the adiabatic basis set of electronic wave functions,

$$\Psi(\vec{r}, \vec{R}) = \sum_k \varphi_k(\vec{r}, \vec{R}) F_k(\vec{R}) \tag{3-4}$$

where $\varphi_k(\vec{r}, \vec{R})$ are the electronic wave functions and $F_k(\vec{R})$ are the nuclear wave functions.

The electronic Hamiltonian is given by

$$h_{el} = -\frac{1}{2m}\nabla_r^2 - \left[\frac{Z_A}{r_A} + \frac{Z_B}{r_B}\right] = T + V \tag{3-5}$$

The set of electronic wave functions $\{\varphi_k(\vec{r}, \vec{R})\}$ consists of eigenfunctions of the electronic Hamiltonian which obey the eigenvalue equation

$$h_{el}\varphi_k(\vec{r}, \vec{R}) = \epsilon_k(R)\varphi_k(\vec{r}, \vec{R}). \tag{3-6}$$

In general, the electronic potential energy ϵ_k depend only upon the internuclear distance $R = |\vec{R}|$ and electronic wave function φ_k is a function of internuclear *vector* $\vec{R}$.

However, if $\vec{r}$ is expressed in coordinates rotating with the axis $\vec{R}$, φ_k again depends only upon $R = |\vec{R}|$.

Inserting Eq. (3-4) into the Schrödinger equation, multiplying on the left by an electronic function and integrating over all electronic coordinates, this results into a set of coupled differential equations for the nuclear wave function $F_k(\vec{R})$,

$$\left\{\frac{1}{2\mu}\left[(-i\vec{\nabla}_R)^2 + 2\vec{\mathbf{P}}\cdot(-i\vec{\nabla}_R) + \mathbf{B}\right] + \mathbf{U}\right\}\mathbf{F}(\vec{R}) = -E\mathbf{F}(\vec{R}) \tag{3-7}$$

where $\vec{\mathbf{P}}$ and $\mathbf{B}$ are the first and second derivative coupling matrices given by

$$\vec{P}_{k'k}(R) = \langle\varphi_{k'}(\vec{r},\vec{R})| - i\vec{\nabla}_R|\varphi_k(\vec{r},\vec{R})\rangle \tag{3-8}$$

and

$$B_{k'k}(R) = \langle\varphi_{k'}(\vec{r},\vec{R})| - i\vec{\nabla}_R^2|\varphi_k(\vec{r},\vec{R})\rangle \tag{3-9}$$

The potential energy matrix $\mathbf{U}$ is given by: $U_{k'k}(R) = (\epsilon_k + (Z_A Z_B/R))\delta_{k'k}$.

Equations (3-7) can also be written in an alternative form. Using the closure relation of MO wavefunctions, $\mathbf{B}(R)$ can be eliminated in favor of $\vec{\mathbf{P}}$, and Eqs. 3-7 become

$$\left\{\frac{1}{2\mu}\left[(-i\vec{\nabla}_R) + \vec{\mathbf{P}}\right]^2 + \mathbf{U}\right\}\mathbf{F}(\vec{R}) = E\mathbf{F}(\vec{R}). \tag{3-10}$$

In a finite set of states, the closure relation is not exact, but it should be sufficiently accurate for most purposes.

It is well known that the individual terms in the expansion Eq. (3-4) do not satisfy the scattering boundary conditions [8, 96] and several difficulties appear in Eqs. (3-10) (or (3-7)) which are evident upon calculations of the matrix elements of the first derivative coupling matrix $\vec{\mathbf{P}}$.

1. *The first derivative coupling matrix* $\vec{\mathbf{P}}$ *does not vanish asymptotically as* $R \to \infty$.

   This is because in the calculation of matrix elements of $\vec{\nabla}_R$, the electronic coordinate is held fixed with respect to the geometric center of the nuclei rather than with respect to either nucleus. It is shown that as $R \to \infty$, $\vec{P}_{k'k}(R) \to$ const which is not necessarily to be zero. Physically, this represents the motion of the atomic orbitals relative to center of mass of the nuclei as R changes. These findings do not allow a scattering theory to be formulated, since boundary conditions are not obeyed.

2. *The first derivative coupling term* $\vec{\mathbf{P}}$ *also contains fictitious "origin dependent" couplings.*

   This is evident when one calculates the nonzero $\vec{\mathbf{P}}$ matrix between states with different parity (g, u), which is the result of the inappropriate formulation of the theory. This is particularly important in the ground state manifold of HD^+, where the only contribution to the matrix $\vec{\mathbf{P}}$ is fictitious. Calculations of $\vec{\mathbf{P}}$ matrix show a non-negligible contributions between the states $1s\sigma_g$ and $2p\sigma_u$, whose order of magnitude is much too large. These contributions are eliminated in the corrected theory described below.

The common source of the above problem is the lack of a proper formulation of the asymptotic coupling between the electronic motion and the motion of nuclei. To elaborate on this point, we note that the coupling matrix $\vec{\mathbf{P}}$ represents the total change of the basis functions with respect to the nuclear coordinate $\vec{R}$. The effect of the coupling matrix $\vec{\mathbf{P}}$ can be divided into two parts,

1. Rotation, distortion, polarization, which result in physical change of the basis set functions with $\vec{R}$.

2. Translational motion of the electron along with one atomic nucleus.

The first part is responsible for nonadiabatic transitions. Couplings originating from the second part are not physical, as shown by Thorson and his co-workers [8, 79, 80, 96].

Steps to overcome this problem have been taken into account by incorporating an ETF into the MO basis functions,

$$\exp\left[i(m/\mu)(-i\vec{\nabla}_R)\cdot\vec{s}_k\right]\varphi_k \tag{3-11}$$

where

$$\vec{s}_k = \frac{1}{2}(f_k+\lambda)[\vec{r}-\frac{1}{4}(f_k+\lambda)\vec{R}] \tag{3-12}$$

$f = f(\vec{r}, \vec{R})$ [1] is a switching function which varies smoothly as a function of electron position $\vec{r}$; typically it may approach -1 near nucleus A and $+1$ near nucleus B, and these limiting values must hold as $R \to \infty$. The mass asymmetry factor λ

[1] In general, switching function f can be a function of *internuclear vector* $\vec{R}$. In the studies presented here, the switching function f is taken only as a function of internuclear distance R.

is given by $\lambda = (M_A - M_B)/(M_A + M_B)$ (note that $0 \leq \lambda < 1$ since $M_A \geq M_B$). Here $\exp[i(m/\mu)(-i\vec{\nabla}_R) \cdot \vec{s}_k]\varphi_k$ may be called as "ETF-modified MO" wave functions, which satisfy the scattering boundary conditions by the individual terms.

With the aid of Eq. (3-11), the expansion of total wave function on the MOs now is replaced by the ansatz:

$$\Psi(\vec{r}, \vec{R}) = \sum_k \exp[i(m/\mu)(-i\vec{\nabla}_R) \cdot \vec{s}_k]\varphi_k(\vec{r}, \vec{R})F_k(\vec{R}) \tag{3-13}$$

To obtain coupled equations for the heavy-particle wave function $F_k(\vec{R})$, let us put Eq. (3-13) in the Schrödinger equation (3-3) and multiply by $\langle\varphi_{k'} \exp[-i(m/\mu)(-i\vec{\nabla}_R) \cdot \vec{s}_{k'}]$:

$$\sum_k \langle\varphi_{k'}| \exp[-i(m/\mu)(-i\vec{\nabla}_R) \cdot \vec{s}_{k'}](H - E) \exp[i(m/\mu)(-i\vec{\nabla}_R) \cdot \vec{s}_k]|\varphi_k\rangle = 0 \tag{3-14}$$

Here the integration implied by the angular brackets is only over the electronic coordinates, and operators $\exp[i(m/\mu)(\pm i\vec{\nabla}_R) \cdot \vec{s}_k]$ act implicitly on both φ_k and F_k.

If we express the Hamiltonian in powers of m/μ and neglect terms of order $(m/u)^2$ ($\approx 10^{-6}$ for H^{2+}) and higher powers, and also neglect terms of order m/μ which are proportional to derivatives of the switching function or related factors [e.g., $(f^2 - 1)$], a new set of coupled equations for the $F_k(\vec{R})$ is obtained

$$\left\{\frac{1}{2\mu}\left[(-i\vec{\nabla}_R) + \vec{\mathbf{P}} + \vec{\mathbf{A}}\right]^2 + \mathbf{U} + \left[\mathbf{\Delta} - (2\mu)^{-1}\vec{\mathbf{A}} \cdot \vec{\mathbf{A}}\right]\right\}\mathbf{F}(\vec{R}) = E\mathbf{F}(\vec{R}) \tag{3-15}$$

where $\vec{\mathbf{P}}$ and $\mathbf{U}$ are as before, and the matrices $\vec{\mathbf{A}}$, $\mathbf{\Delta}$ are given by

$$\begin{aligned}
\vec{A}_{k'k}(R) &= i\langle\varphi_{k'}(\vec{r}, \vec{R})|[h_{el}, \vec{s}]|\varphi_k(\vec{r}, \vec{R})\rangle && (3\text{-}16)\\
&= i(\epsilon_{k'} - \epsilon_k)\langle\varphi_{k'}(\vec{r}, \vec{R})|\vec{s}|\varphi_k(\vec{r}, \vec{R})\rangle && (3\text{-}17)\\
\Delta_{k'k}(R) &= \langle\varphi_{k'}(\vec{r}, \vec{R})|V(\vec{r}, \vec{R} - (m/\mu)) - V(\vec{r} - \vec{R})|\varphi_k(\vec{r}, \vec{R})\rangle && (3\text{-}18)
\end{aligned}$$

The most important modification produced by the ETF's in these equations is the replacement if the nonadiabatic couplings $\vec{\mathbf{P}}$ by the corrected coupling $\mathbf{P}\vec{+}\mathbf{A}$ in the kinetic-energy term. The term $\mathbf{\Delta} - (2\mu)^{-1}\vec{\mathbf{A}} \cdot \vec{\mathbf{A}}$ is much smaller [79], which describes the reduced-mass effects on electron binding energies $\sim (m/\mu)\epsilon_k$ and can be neglected for nearly all scattering problems. Thus the coupled equations (3-15) can be simplified as

$$\left\{\frac{1}{2\mu}\left[(-i\vec{\nabla}_R) + \vec{\mathbf{P}} + \vec{\mathbf{A}}\right]^2 + \mathbf{U}\right\}\mathbf{F}(\vec{R}) = E\mathbf{F}(\vec{R}), \tag{3-19}$$

which has the same *form* as (3-10).

The solution of Eq. (3-19) is performed in two steps. First, Eq. (3-6) is solved to get the basis set functions $\{\varphi_k\}$ and the potential energies ϵ_k as a function of the internuclear coordinate. This is done by transforming the problem into prolate spheroidal coordinates in which the electronic Hamiltonian is separable [97] (see also Appendix A). In the second step, Eqs. (3-7) is converted to a radial equation by transformation to a rotating coordinate system, and expansion of the wave function in symmetric-top eigenfunctions followed by integration over the angular coordinates, as explained, e.g., in Refs. [96] and [32]. The resulting nuclear wave function $\mathbf{G}(R)$ is a function of the magnitude of the nuclear coordinate only. The radial equation is then solved to obtain the wave function, the transition amplitude and so forth.

Consider that electronic transitions seldom involve the transfer of more than one or two units of angular momentum while typically the collisional angular momentum of the heavy particles is very large. Classically this means that angular momentum transfer to the electron system has nearly negligible deflection effect on the heavy particles, i.e. the collision occurs in a plane and the heavy particle angular momentum K is approximately conserved. Then the differential equation for the heavy-particle wave function $\mathbf{G}(R)$ is given by

$$\left\{\frac{1}{2\mu}\left[-i\frac{d}{dR}+\mathbf{P}^R+\mathbf{A}^R\right]^2+\frac{K(K+1)}{2\mu R^2}\mathbf{1}+\frac{\sqrt{K(K+1)}}{\mu R}\left[\mathbf{P}^\Theta+\mathbf{A}^\Theta\right]\right\}\mathbf{G}(R) = \left[\mathbf{1}E-\mathbf{U}(R)\right]\mathbf{G}(R) \quad (3\text{-}20)$$

where $\mathbf{P}^R+\mathbf{A}^R$ and $\mathbf{P}^\Theta+\mathbf{A}^\Theta$ are the radial and angular parts of corrected nonadiabatic coupling term $\vec{\mathbf{P}}+\vec{\mathbf{A}}$, defined by Eqs. (B-9) and (B-10). For more details see Appendix B.

3.2 Semi-classical close-coupled equations

The ion-atom collision system is essentially described by two parameters, namely the de Broglie wavelengths of the proton and the electron, and in particular the magnitude of these wavelengths relative to typical atomic dimensions. The de Broglie wavelength of the proton is very small in comparison to the size of an atom, and for this reason a very large number of partial waves contribute to the cross sections,

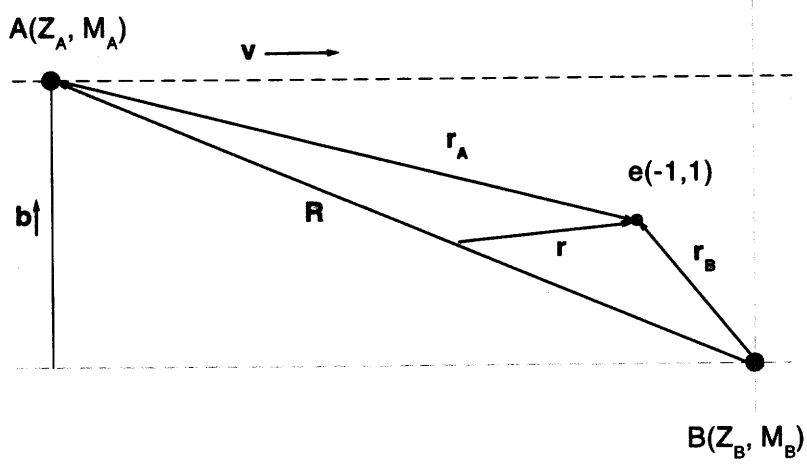

Figure 3.2 The definition of impact parameter.

typically thousands, even at collision velocities of a few keV/amu. Partial wave expansions are thus very heavy as a means of calculating the cross sections, and one is forced to use other methods. The very small de Broglie wavelength of the proton does however admit a major simplification of practical importance, namely the relative motion of the heavy particles may be treated classically. In the case of the electron, the de Broglie wavelength is comparable to atomic dimensions and therefore the motion of the electron must be treated quantum mechanically. This semi-classical approach, i.e. treating the relative motion of the heavy particles classically and the electronic motion quantum mechanically, is adopted hereinafter.

Within the semi-classical impact parameter picture, a projectile of charge Z_A and mass M_A collides with a target of charge Z_B and mass M_B. The heavy particles move along rectilinear (or curvilinear) trajectories so that their equation of relative motion is $\vec{R}(t) = \vec{b} + \vec{v}t$, where $\vec{b}$ is the impact parameter and $\vec{v}$ is the collision velocity. The vectors $\vec{b}$ and $\vec{v}$ define the collision plane. In general, the vectors $\vec{r}_A$, $\vec{r}_B$ and $\vec{r}$

(the position vector of the electron with respect to the center-of-mass of the target and the projectile) lie outside this plane. Let us note that the Hamiltonian is now time-dependent, that is

$$H = -\frac{1}{2}\nabla_r^2 - \frac{Z_A}{r_A} - \frac{Z_B}{r_B} + \frac{Z_A Z_B}{R(t)}, \tag{3-21}$$

and we are required to solve the time-dependent Schrödinger equation,

$$\left(H - i\frac{d}{dt}\right)\Psi(\vec{r},t) = 0. \tag{3-22}$$

After the trajectory is specified, the internuclear potential energy term $Z_A Z_B/R(t)$ is just a (time-dependent) parameter multiplied by the unit matrix in this Hamiltonian, (3-21), and it can be eliminated by adjusting the phase of the wave function by the factor $\exp\int^t Z_A Z_B/R(t')dt'$. Then the time evaluation of this system is described by

$$i\hbar\frac{d}{dt}\Psi(\vec{r},t) = h_{el}(\vec{r},\vec{R}(t))\Psi(\vec{r},t), \tag{3-23}$$

where h_{el} is the Hamiltonian of the electron system defined as before.

We expand the state vector Ψ in an ETF-modified molecular basis set,

$$\Psi(\vec{r},t) = \sum_n a_n(t)\varphi_n(\vec{r},\vec{R})\exp\left[i\vec{v}\cdot\vec{s}_n\right]\exp\left[-i\int^t\left(\epsilon_n(t') + \frac{mv^2}{8}\right)dt'\right] \tag{3-24}$$

where $\vec{v} = d\vec{R}/dt$ is the relative nuclear velocity. Substituting Eq. (3-24) in the time-dependent Schrödinger equation, Eq. (3-23), then multiplying by

$$\varphi_k^* \exp\left(-i\vec{v}\cdot\vec{s}_k\right)$$

and integrating over electron coordinates yields the coupled equations for the coefficients $a_k(t)$; after expanding those in powers of velocity $\vec{v}$, one obtains

$$i\frac{da_k(t)}{dt} = \sum_{n\neq k}\vec{v}\cdot(\vec{P}+\vec{A})_{kn}a_n(t)\exp\left[-i\int^t\left(\epsilon_n(t') - \epsilon_k(t')\right)dt'\right] \tag{3-25}$$

(up to the first order), where $\vec{\mathbf{P}}$ is the nonadiabatic couplings and $\vec{\mathbf{A}}$ is the corrections rising from ETFs. They are very same as those in full quantum-mechanical formulation, (3-8) and (3-16).

Although in the present context the quantum and classical trajectory description are developed as separate frameworks, the relationship between the two approach

has be studied in detail [32]. The quantum-mechanical form of the coupled equations can be reduced to the classical trajectory form by the systematic use of semiclassical approximations. These approximations define the strength and the limitations of the classical trajectory method.

The solutions of Eqs (3-25) are found by similar procedure for solving Eqs. (3-19): i) firstly to find the basis wave functions by solving the eigenvalue problem of Eq. (3-6), ii) then to separate the "radial" from the "angular" terms by transforming to molecular body fixed rotating frame; iii) finally to integrate the resulted equations

$$i\hbar\frac{da_k(t)}{dt} = \sum_{n\neq k}\left[\dot{R}(P^R + A^R) + R\dot{\Theta}(P^\Theta + A^\Theta)\right]_{kn} a_n(t) \times \exp\left[-i\int^t \left(\epsilon_n(t') - \epsilon_k(t')\right) dt'\right], \tag{3-26}$$

where Θ is the angle between relative velocity and internuclear axis $\Theta = \angle(\vec{v}, \vec{R})$, and the radial $\mathbf{P}^R + \mathbf{A}^R$ and angular $\mathbf{P}^\Theta + \mathbf{A}^\Theta$ coupling terms are defined as before (see Appendix B).

Before we move on to solve the close-coupled equations (3-26), a subtle point associated with the ETF's modified molecular orbital expansion approach needs to be discussed. This is the non-Hermitian Hamiltonian matrix $(\vec{P}+\vec{A})$ in Eq. (3-26). In any calculation, we need to replace the full Hilbert space spanned by the true discrete and continuum states with a truncated subspace. As a result, certain operators in the equations of motion cannot be fully represented, and unless great care is taken they may not even be accurately represented within the truncated subspace. This is true in particular for the propagator itself. Thus, a theory should consider the flux loss from the truncated subspace, and then, in contrast with the exact close-coupled equations, the close-coupled equations for the wave function in the truncated subspace are necessarily non-unitary, *i.e.* they should not conserve probabilities. Our locally non-Hermitian Hamiltonian matrix $(\vec{P} + \vec{A})$ allows us to consider the escape of electron from the subspace spanned by the truncated basis. Importantly, the flux loss effects decrease with the basis size increase, and the probability conservation is satisfied approximately on a sufficiently large basis set. By implementing the ETF's, the basis sets of relatively small size can be considered as complete with sufficient accuracy. In the present studies, I find the probability conservation is better than

1×10^{-3} with a basis set including 10 bound states and 11 continuum partial waves (for proton-hydrogen system).

3.2.1 Perturbative solutions of close-coupled equations

The close-coupled equations, Eq. (3-25), can be solved by numerical integration in full dimension, but also possibly using a perturbation approach. Accounting for the fact that all the discrete-continuum couplings are very weak (see Sec. 4.1), we could thus construct a faster algorithm for ionization problems.

Let us now consider a system which contains n-bound states plus one continuum state, then the time-dependent Schrödinger equations for $n+1$-channels reads,

$$i\hbar \begin{pmatrix} \dot{a}_1 \\ \dot{a}_2 \\ \vdots \\ \dot{a}_n \\ \dot{\alpha}_\epsilon \end{pmatrix} = \begin{pmatrix} 0 & C_{12}(t) & \cdots & C_{1n}(t) & \aleph_{1\epsilon}(t) \\ C_{21}(t) & 0 & \cdots & C_{2n}(t) & \aleph_{2\epsilon}(t) \\ \vdots & \vdots & \ddots & \vdots & \vdots \\ C_{n1}(t) & C_{n2}(t) & \cdots & 0 & \aleph_{n\epsilon}(t) \\ \aleph_{\epsilon 1}(t) & \aleph_{\epsilon 2}(t) & \cdots & \aleph_{\epsilon n}(t) & 0 \end{pmatrix} \begin{pmatrix} a_1 \\ a_2 \\ \vdots \\ a_n \\ \alpha_\epsilon \end{pmatrix}, \tag{3-27}$$

where α_ϵ is the ionization amplitude, and ϵ stands the continuum state energy. Matrix elements $\aleph_{\epsilon i}(t)$ are

$$\aleph_{\epsilon i}(t) = \kappa_{\epsilon i}(t) \exp\left[-\frac{i}{\hbar}\int_{-t_0}^{t} (\epsilon_i(t') - \epsilon)\, dt'\right]$$

, where $\kappa_{\epsilon i}(t)$ denotes the coupling from i-th bound state to continuum ϵ. Suppose the ionization probability is small, we then solve Eq. 3-27 in a first-order perturbation approximation for transition amplitudes. Finding first the $n \times n$ bound state solutions $a_i(t)$, we see that

$$\alpha_\epsilon(t_0) \simeq \sum_{i=1}^{n} \int_{-t_0}^{t_0} \kappa_{\epsilon i}(t) \exp\left[-\frac{i}{\hbar}\int_{-t_0}^{t} (\epsilon_i(t') - \epsilon)\, dt'\right] a_i(t) dt \tag{3-28}$$

The phase factor above rapidly oscillates with t, which makes the results small, and the method of Eq. (3-28) applicable. Hence we can calculated at once the ionization cross sections for whole energy distribution ϵ of ejected electron, changing only the couplings $\kappa_{\epsilon i}(t)$. In general, the method of Eq. (3-28) is ~ 100 times faster than that of solving the differential Eq. (3-27).

Although the perturbation solutions reproduce the final state amplitudes much faster, it should be noted that the accuracy decreases with the transition probability

increasing. In a collision with $E > 5$ keV/amu, $\epsilon < 0.1$ Ry, and $b \sim 1.0$, the ionization probability can be higher than 0.1 even 0.2 in some case ($p - \mathrm{H}$ system). Since integration of differential equations (3-26) in our case is tractable, we prefer to solve Eq. (3-26) directly to ensure that no important interactions are missing. A Runge-Kutta-Vener method with 10^{-6} accuracy has been employed in the present study, to keep the overall numerical inaccuracy confined to cross sections smaller than 10^{-3} after integrating the transition probabilities over all impact parameters.

Once the final-state amplitude $a_k(t = +\infty)$ has been calculated with proper initial conditions, we can then define the probability of excitation/or ionization to the molecular state k as

$$P_k(E, b) = |a_k(t = +\infty)|^2, \tag{3-29}$$

and the corresponding individual cross section is

$$Q_k(E) = 2\pi \int P_k(E, b) b db. \tag{3-30}$$

In ionization problems, $P_k(E, b)$ is the ionization probability and $Q_k(E)$ is the partial ionization cross section. They are labelled by the ejected electron energy ϵ, and two more spheroidal prolate quantum numbers λ, and μ. Hence the differential ionization cross section is determined by summing $Q(\epsilon, \lambda, \mu; E)$ over quantum numbers λ, μ,

$$\frac{d\sigma}{d\epsilon} = \sum_{\lambda,\mu} Q(\epsilon, \lambda, \mu; E), \tag{3-31}$$

and the total ionization cross section,

$$\sigma = \int \frac{d\sigma}{d\epsilon} d\epsilon, \tag{3-32}$$

is obtained by integrating the energy distribution of ejected electrons.

3.3 Discretization of continuum

The key component in describing electron emission in ion-atom collisions is an adequate representation of the continuum. To be more specific, in order to calculate accurate ionization, excitation and capture cross-sections it is necessary to describe the electron in the double continuum of the target and the projectile. A pragmatic

approach to this problem is to represent the continuum by a large set of L^2 functions with positive eigenvalues. By including enough of these non-physical *pseudostates* a good approximation to the continuum wavefunctions is ought. Such an approach is not however without its difficulties. In particular:

- Positioning:

  On which center should the pseudostates be placed? On the target? On the projectile? On both centers? Or on a third center?

- Double-counting:

  If pseudostates are placed on both centers is the basis now over-complete? This must be certainly true in the limiting case of an infinite number of pseudostates.

- Linear dependence:

  There is no rigorous test to ensure that the pseudostate basis is free from linear dependence which becomes more likely as the basis gets very large.

- Convergence:

  For a given collision system and a given set of bound states there is no a priori determination of the number of pseudostates required for convergence. Thus it is not possible to know whether structures in the cross sections are physical features or due to the basis set.

In a recent series of very detailed coupled-channel pseudostate calculations using an even-tempered basis, Kuang and Lin [84, 85] have concluded that in order to calculate excitation cross sections all the pseudostates should be centered on the target, so called Bound Bound Continuum-Target (BBC-T), and conversely, in order to calculate the capture all the pseudostates should centered on the projectile, so called Bound Bound Continuum-Projectile (BBC-P). This indicates that pseudostates on both centers engender over-completeness.

However even these large scale asymmetric calculations can produce spurious oscillations in the cross sections for weaker transitions-see, for example, figure 1 of Kuang and Lin [84]. A shoulder at 40 keV in the 1s-3d cross sections appears in proton-hydrogen collisions when 56 pseudostates are used. This feature is absent when 154 pseudostates are used (see figure 2 of Kuang and Lin [84]).

This example is taken not to denigrate the pseudostate approach, but merely to point out that attempting to represent what is in effect an infinite number of partial waves, by a finite basis set, and indeed trying to represent the infinite range Coulomb potential by a series of short range potentials, has inherent difficulties. It is also appropriate to question whether an asymmetric expansion, however large, can truly model the three-body nature of the collision. What is certain is that the symmetry of the Hamiltonian under reflection in the electronic co-ordinate $\vec{r} \rightarrow -\vec{r}$, is not preserved by such an expansion.

To avoid these inherent difficulties of L^2 pseudostate expansion, I have chosen the exact continuums as basis functions in the close-coupled equations (3-25) and/or (3-19). Then the expansion of total wave function reads

$$\Psi(\vec{r}, \vec{R}(t)) = \sum_n \varphi_n(\vec{r}, \vec{R}) a_n(t) + \int_0^\infty \varphi_\epsilon(\vec{r}, \vec{R}) a_\epsilon(t) d\epsilon. \tag{3-33}$$

As stated in the Appendiex A, the molecular eigenstates φ_n (and φ_ϵ) are labelled by two more quantum numbers λ, μ, in addition to energy. Bound states are denoted $\phi(n\lambda\mu; \vec{r}; \vec{R})$, with energy eigenvalues $\epsilon(n\lambda\mu; R) < 0$, and continuum states $\phi(\epsilon\lambda\mu; \vec{r}; \vec{R})$ with continuous eigenvalues $\epsilon > 0$. At each R these wave functions satisfy the orthogonality relations

$$\begin{aligned} \langle \phi(n'\lambda'\mu'; \vec{R}) | \phi(n\lambda\mu; \vec{R}) \rangle &= \delta_{n'n}\delta_{\lambda'\lambda}\delta_{\mu'\mu} \\ \langle \phi(\epsilon'\lambda'\mu'; \vec{R}) | \phi(n\lambda\mu; \vec{R}) \rangle &= 0 \\ \langle \phi(\epsilon'\lambda'\mu'; \vec{R}) | \phi(\epsilon\lambda\mu; \vec{R}) \rangle &= \delta(\epsilon' - \epsilon)\delta_{\lambda'\lambda}\delta_{\mu'\mu} \end{aligned} \tag{3-34}$$

and the closure relation

$$\sum_{n\lambda\mu} \varphi_{n\lambda\mu}(\vec{r}, \vec{R}) \varphi_{n\lambda\mu}(\vec{r}', \vec{R}) + \sum_{\lambda\mu} \int_0^\infty \varphi_{\epsilon\lambda\mu}(\vec{r}, \vec{R}) \varphi_{\epsilon\lambda\mu}(\vec{r}', \vec{R}) d\epsilon = \delta(\vec{r} - \vec{r}'). \tag{3-35}$$

Here the prolate spheroidal quantum numbers λ, μ are analogous to spherical polar quantum number l, m. Expanding in the eigenstates of one-electron diatomic molecule, the difficulties related to pseudostate expansion such as "positioning", "double-counting" and linear dependence of basis functions are completely avoided.

The energy of continua electrons is explicitly included in the equations of motion via the coupling terms in Eqs. (3-26), whilst the total ionization cross section requires a formal integration over the whole continuum. Therefore, we need to revert to a

discrete sampling scheme as described further. This work assumes the electronic continuum basis states are "simple" in certain ways, namely vary smoothly without displaying any "fine structure" of the sort associated with Feshbach resonances (and arising from the mixing with specific alternative physical configurations). Then the continuum states can be interpolated well by the B-spline,

$$\varphi_\epsilon(\vec{r}, \vec{R}) = \sum_i B_i^k(\epsilon)\phi_i(\vec{r}, \vec{R}). \tag{3-36}$$

Thus the close-coupled equations (3-26) are solved firstly on a specific knot sequence of B-spline, and integrated over continuum energies in the exact equations. In the present study, 4-th order B-spline with equally spaced logarithm knots is employed.

Our study and also previous works in literature [81, 82, 98] find couplings with continuum states to be generally weak, and the full close-coupled equations 3-26 can be partitioned into separate groups. Each group contains the strongly coupled symmetry allowed discrete states (cf. Table 4.1) and several partial waves for continuum electron with the same energy; these are coupled by weak radial or angular interactions. Truncation in the partial wave expansion of the continuum electron is based on a rapid decrease of the couplings with the increasing angular momentum number ($\sim$ 3 orders of magnitude for ejected electron with l=5). Therefore, we calculate the differential ionization cross sections at a certain set of separate energy points, interpolate these with B-splines, and finally integrate the spline function over the whole continuum analytically. Thus the convergence in the number of continuum states can be controlled through the convergence of B-spline interpolation. Ionization cross sections decrease rapidly with the ejected electron energy increase, and the necessary number of interpolation points derives from the number of B-spline terms which can accurately represent this function shape. The differential cross sections (see Fig. 4.15) already vary smoothly with free electron energies on the 32 point grid (checked also with 64, and 128 points), yielding sufficiently converged and accurate results.

4.0 Study of Ionization in H(1s)+H$^+$ collision

"To understand hydrogen is to understand all physics"[99]. This short statement is easily extended to summarize the motivation of studying proton-hydrogen collisions, in particular, for impact ionization which is a prototype of the break up of three charged particles. However, discrepancies are still quite large among experiments [1,2] and among theories [3–5]. The energy dependence of theoretical and experimental results are also different. I will concentrate on this fundamental problems in this chapter.

4.1 Potential curves and couplings

Figure 4.1 shows electronic energy $\epsilon_k(R)$ versus R for 21 molecular states of H_2^+. Since the collision Hamiltonian is rigorously centrosymmetric for p-H system, the state vector Ψ in Eq. (3-23) is composed of noninteracting g (gerade) and u (ungerade) components (indicated by red and blue lines respectively in Fig. 4.1), and thus there are corresponding sets of g and u close-coupled equations 3-26. If index "1" designates the initial states in each set ($1s\sigma_g$ or $2p\sigma_u$, respectively), then the initial conditions for Eqs. (3-26) (corresponding to "proton A plus atom B") is

$$a_k(t = -\infty) = 1/\sqrt{2}\delta_{1k}, \tag{4-1}$$

and (for given energy E and each impact parameters b) the final-state amplitudes $a_k(E, b)$ is computed.

To compute the ionization cross sections, we have carried out systematic calculations with basis sets A, B, and C, as listed in Table 4.1. Comparing the numerical results with different basis sets allows us to study the convergence of ionization cross sections with the basis size. In addition, some selected calculation have been done on the ungerade component of basis set C without $2p\pi_u$ (set D) to understand the role of upper levels in the ionization dynamics. The continuum component is common in the basis sets A (direct ionization), B, C (indirect ionization), and D, which contains 32 energies below 1.0 Ry for each partial wave; then the total continuum states are accounted for up to 352. Within the straight-line approximation, we have solved the

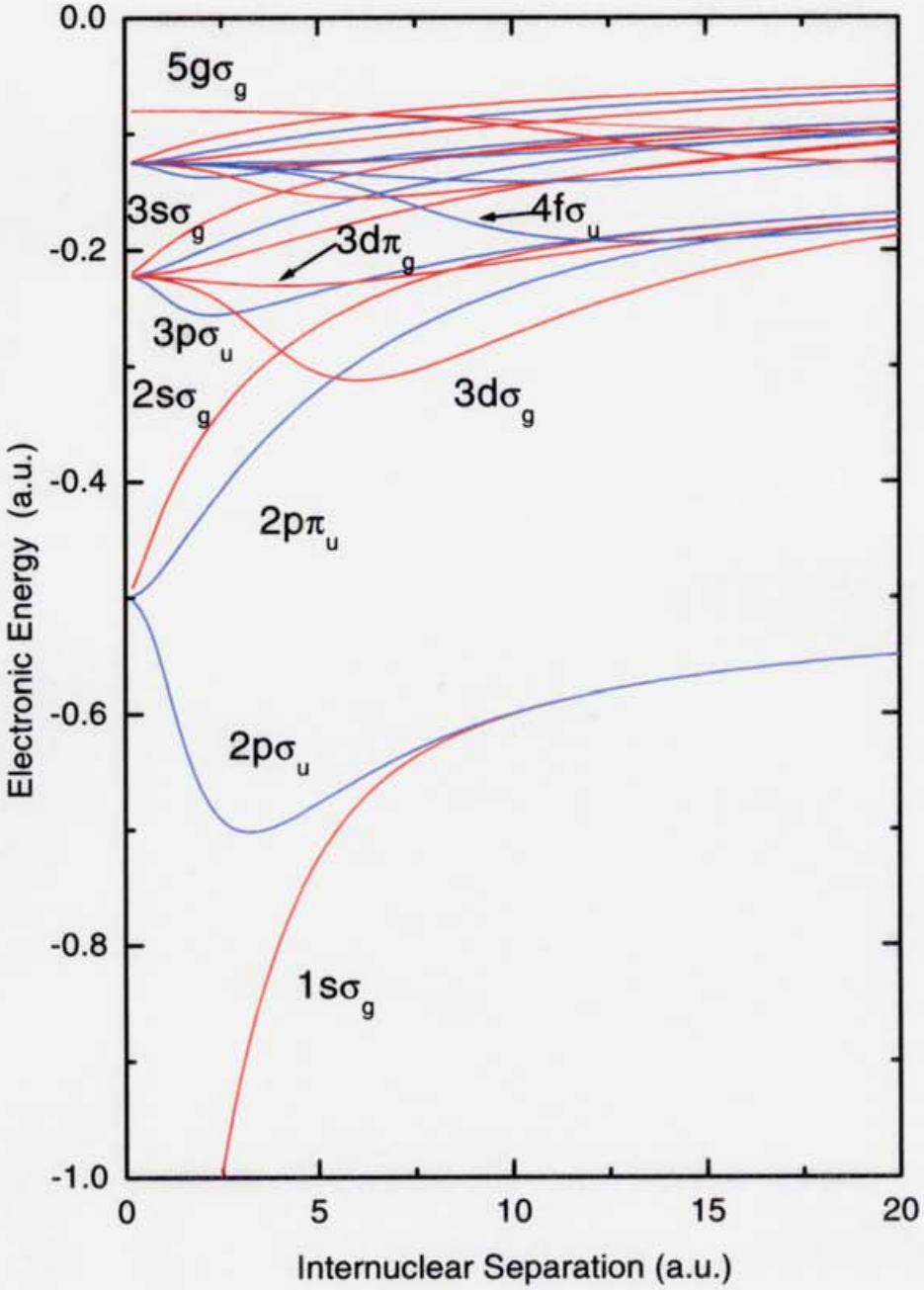

Figure 4.1 Electronic energy $\epsilon_k(R)$ (a.u.) versus R, for 21 molecular states of H_2^+

Table 4.1 Molecular basis sets of calculations for $H^+ + H(1s)$ collision.

Sets	Gerade basis states	Ungerade basis states	Number of all states
continuum:	$\|\epsilon s\sigma_g\rangle$	$\|\epsilon p\sigma_u\rangle$, $\|\epsilon p\pi_u\rangle$	
	$\|\epsilon d\sigma_g\rangle$, $\|\epsilon d\pi_g\rangle$	$\|\epsilon f\sigma_u\rangle$, $\|\epsilon f\pi_u\rangle$	
	$\|\epsilon g\sigma_g\rangle$, $\|\epsilon g\pi_g\rangle$	$\|\epsilon h\sigma_u\rangle$, $\|\epsilon h\pi_u\rangle$	
	5 partial waves, for 32 energies	6 partial waves, for 32 energies	11×32 =352
and bound:	all above, plus	all above, plus	
A:	$\|1s\sigma_g\rangle$	$\|2p\sigma_u\rangle$	354
B:	all above, plus	all above, plus	
	$\|3d\pi_g\rangle$	$\|2p\pi_u\rangle$	
	$\|3d\sigma_g\rangle$	$\|3p\sigma_u\rangle$	
	$\|2s\sigma_g\rangle$	$\|3p\pi_u\rangle$	360
C:	all above, plus	all above, plus	
	$\|4d\pi_g\rangle$	$\|4f\sigma_u\rangle$	362
D:	-	all above, minus	
		$\|2p\pi_u\rangle$	[1] 196

coupled differential equations, Eq. (3-26), for 100 impact parameters arranged in $0.0 - 10.0$ a.u. at 32 collision energies from 0.1-10 keV/amu.

Employing the ETF's of Ref. [100], we have computed the nonadiabatic coupling for both discrete to discrete and discrete to continuum transitions. The corrections arising from ETF's exactly cancel the spurious asymptotic couplings and produce substantial reductions in the size and effective range of most coupling matrix elements. Since the discrete-discrete couplings have been discussed in detail by Kimura *et al.* [101], we only show the discrete-continuum couplings in Figs. 4.2 and 4.3.

The ETF-corrected couplings from $1s\sigma_g$ and $2p\sigma_u$ to the lowest partial waves are plotted in Figs. 4.2 and 4.3 for the ejected electron energies $\epsilon = 0.01$ and 1.0 Ry, respectively. It can be seen that the corrected couplings are significant only for the first two or three partial waves and their range is less than 10 a.u., whereas the uncorrected perturbed stationary state (PSS) theory predicts large couplings to 30-40

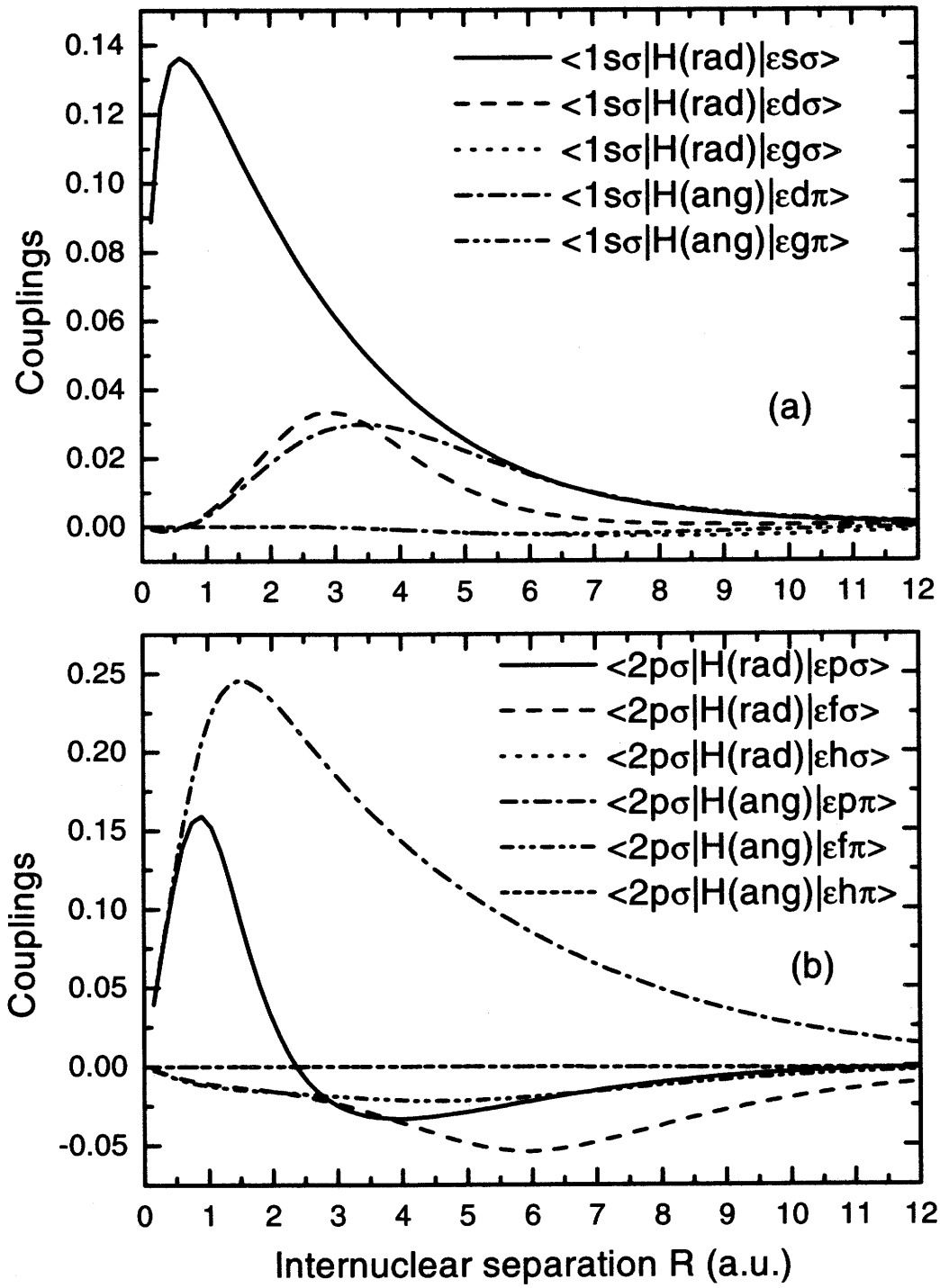

Figure 4.2 Couplings to the lowest partial waves for final electron energies $\epsilon = 0.01$ Ry from the $1s\sigma_g$(a panel) and $2p\sigma_u$(b panel) states in H_2^+ molecule, where H(rad) and H(ang) are the radial and angular coupling operators with ETF-corrections added, respectively.

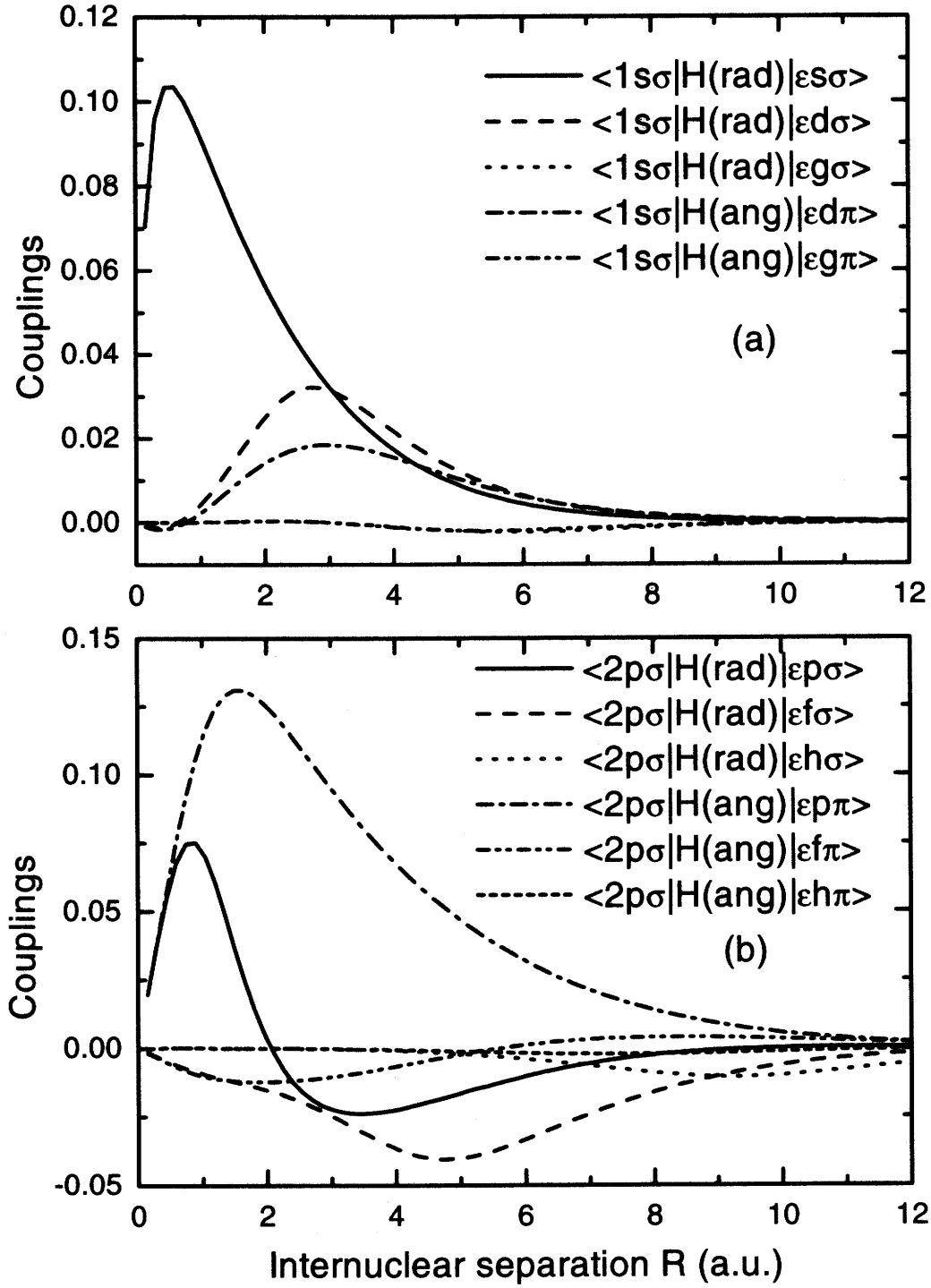

Figure 4.3 Same as Fig. 4.2 except $\epsilon = 1.0$ Ry.

continuum and an envelope of PSS couplings that has a range of 40 a.u.(see also Ref. [102]). The strongest coupling from $2p\sigma_u$ is $\langle 2p\sigma_u|H(ang)|\epsilon p\pi\rangle$ caused by rotation of the quasi-molecule, and it exceeds the radial coupling of $2p\sigma_u$, $\langle 2p\sigma_u|H(rad)|\epsilon p\sigma\rangle$, by 40% at the maximum. However, for the $1s\sigma_g$ coupling, $\langle 1s\sigma_g|H(rad)|\epsilon s\sigma\rangle$ also dominates the other couplings from $1s\sigma_g$.

The energy dependence of couplings $\langle 1s\sigma_g|H(rad)|\epsilon s\sigma\rangle$ and $\langle 2p\sigma_u|H(rad)|\epsilon p\sigma\rangle$ are shown in Fig. 4.4. The couplings from $2p\sigma_u$ are much sensitively dependent on the energy of continua electron than those from $1s\sigma_g$; the size of couplings from $2p\sigma_u$ is reduced by about factor of two with the continua electron energy increase from 0.01 Ry to 1.0 Ry; however couplings from $1s\sigma_g$ are changed only by $\sim$ 25% in size, see also Figs. 4.2 and 4.3. The sensitive energy dependence of couplings from $2p\sigma_u$ is understood by the potential curve of $2p\sigma_u$: near the united atom limit, $2p\sigma_u$ lies about 1.0 Ry below the ionization limit, in contrast to the 4.0 Ry deep potential of $1s\sigma_g$. Then the change of couplings in size is analogous to the potential curves of bound states, as indicated in Eqs. B-9 and (B-10).

Referring to Figs. 4.2, 4.3 and 4.4, we can say that ETF's simultaneously and systematically reduce the couplings from discrete state to all continuum states, and the couplings are significant only for small internuclear separations. Considering the potential curves of $1s\sigma_g$, $2p\sigma_u$ and the corresponding couplings, we may predict tentatively without detailed numerical calculations: (i) ionization cross sections of $2p\sigma_u$ electrons are much larger than those of $1s\sigma_g$ electrons, (ii) ionization is mainly caused by close collisions.

4.2 Ionization probabilities

Collision history [molecular-state probability vs time] of $p\sigma$ and $p\pi$ ionization channels is shown in Fig. 4.5 at collision energy $E = 2$ keV/amu for impact parameter $b = 1.0$ a.u. and final electron energy $\epsilon = 0.01$ Ry. The state probabilities, $P(b)$, oscillate with collision time vt which shows the electron transition in molecular states. The magnitude of oscillation decreases with vt increasing and becomes stable after propagating over a sufficiently long period. Ionization probabilities with basis set A are higher than those of basis set C, by $\sim$ 30% in $p\sigma$ channel, and by one order of magnitude in $p\pi$ channel. This is due to the important flux loss from $2p\sigma_u$

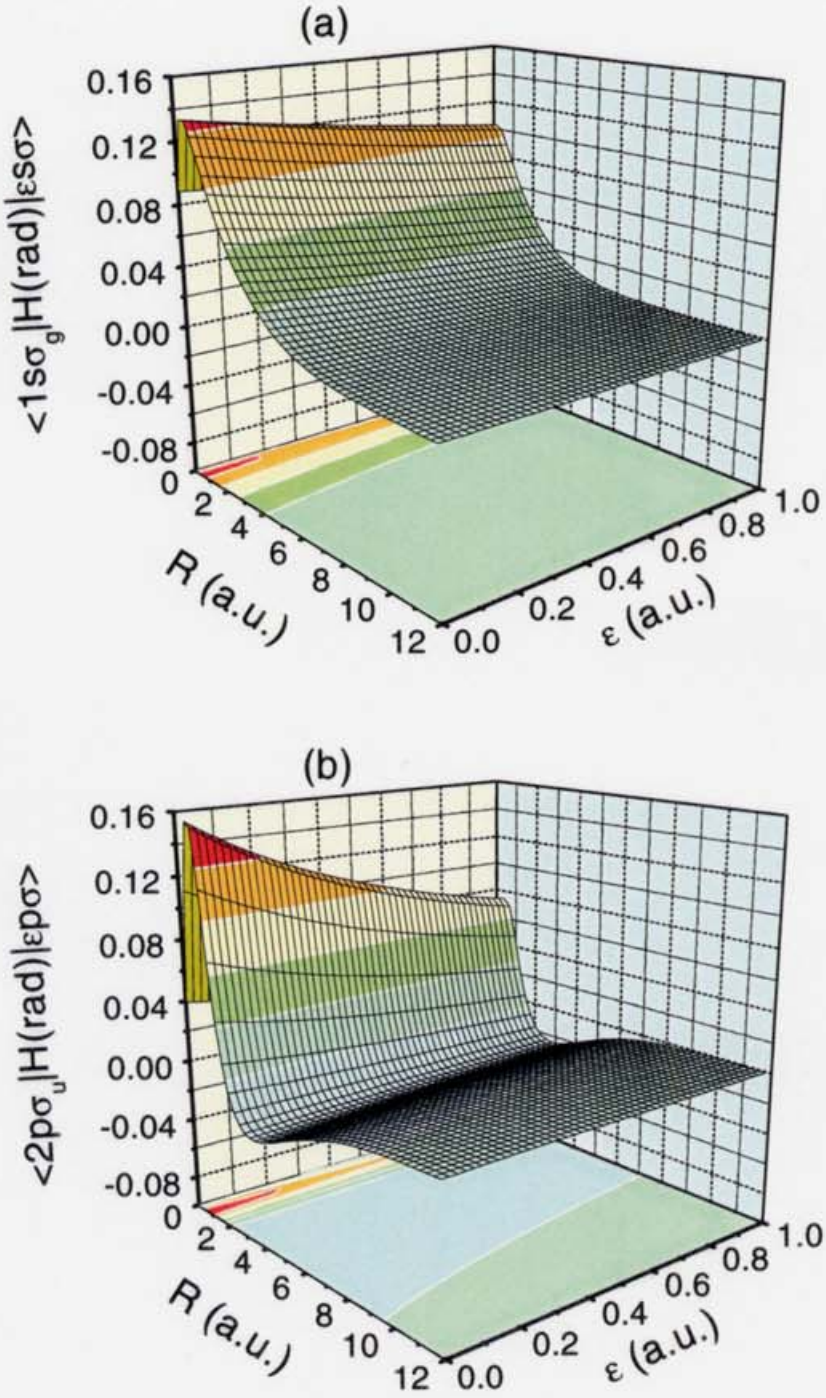

Figure 4.4 Energy dependence of ETF-modified couplings $\langle 1s\sigma_g|H(rad)|\epsilon s\sigma\rangle$: upper panel, and $\langle 2p\sigma_u|H(rad)|\epsilon p\sigma\rangle$: lower panel.

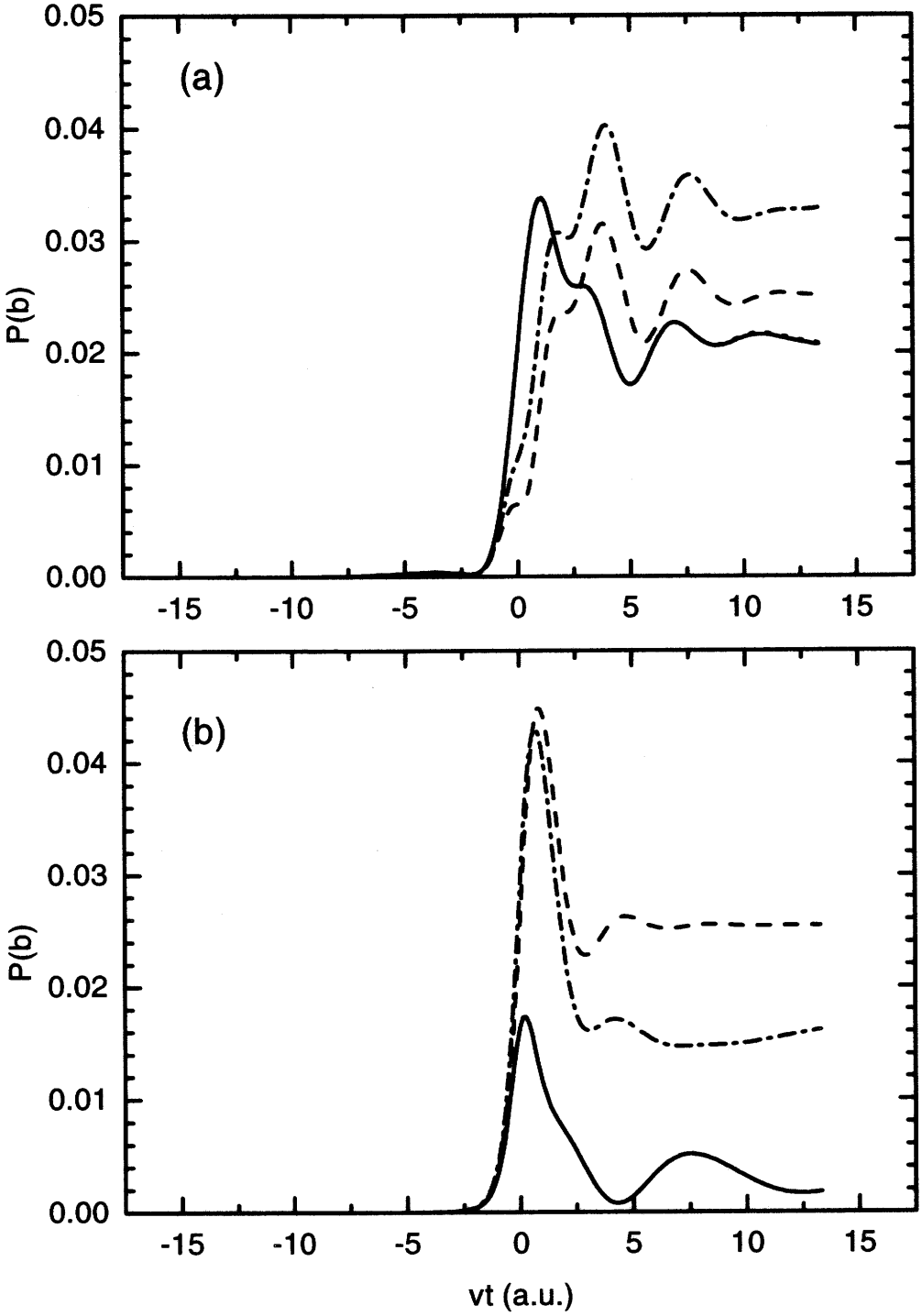

Figure 4.5 Collision history [molecular-state probabilities vs weighted time $(v \times t)$] for the $p\sigma$ (upper panel) and $p\pi$ (lower panel) ionization channels. Collision energy is $E = 2$ keV/amu, impact parameter $b = 1.0$ a.u, and the ejected electron energy $\epsilon = 0.01$ Ry. Dashed lines, basis set A; dotted lines, set B; solid lines, set C; dash dotted lines, set D.

to $2p\pi_u$. The two states $2p\sigma_u$, $2p\pi_u$ are degenerated in the united-atom limit and strongly coupled by the rotation of quasi-molecule. Since couplings to continuum states are significant only for small internuclear separation R, an excitation to $2p\pi_u$ does not reduce the energy gap to continuum much. Thus the strong angular coupling $\langle 2p\sigma_u|H(ang)|2p\pi_u\rangle$ efficiently depopulates the initial state $2p\sigma_u$ and eliminates the maximum appearing in set A near vt =3.5 a.u. To confirm this point, a calculation is done on the basis set D in which $2p\pi_u$ has been removed, and the results are shown as dash dotted lines in this figure. We can see that the upper levels except $2p\pi_u$ increase the ionization probability to $p\sigma$ channel by $\sim$ 25% and decrease the ionization in $p\pi$ channel by $\sim$ 40% comparing to set A. However, $2p\pi_u$ produces much stronger effect than all the others. In this figure, Fig. 4.5, we also plot the ionization probabilities with the basis set B, which is difficult to distinguish from values of set C by eyes. It means that the calculations are already converged with the basis set including 5 bound states and 6 continuum partial waves for ungerade component at the low keV energies.

Figures 4.6 and 4.7 show the weighted ionization probabilities $P(b)b$ of u components as a function the impact parameter b at the ejected electron energies $\epsilon = 0.01$, 0.1 and 1.0 Ry with the collision energies E =2 and 4 keV/amu, respectively. Area below each curve is proportional to the value of partial cross section. From these two figures, it can been seen that only $p\sigma$ or $p\pi$ channel is important for electron emission in this energy range. The ionization probabilities decrease rapidly with the ejected electron energy increasing and with the collision energy decreasing. With the ejected electron energy increasing from 0.1 Ry to 1.0 Ry, the ionization probabilities drop down by one order of magnitude at the maximum of $bP(b)$ for collision energies E =2 or 4 keV/amu. Peak of ionization probabilities shifts to the left hand side (*i.e.* to small impact parameters) with continua electron energy increasing. At the top panel in Fig. 4.6 or 4.7, $\epsilon = 0.01$ Ry, ionization to $p\sigma$ channel predominates others, while at the bottom panel, $\epsilon = 1.0$ Ry, the $p\pi$ channel is the most important. It should also be noted that distribution of ionization probabilities in channels depends on the collision energy E; $p\pi$ electron ionization probability is order of magnitude higher than that of $p\sigma$ at $E = 2$ keV/amu and by factor of two at $E = 4$ keV/amu for $\epsilon = 1.0$ Ry. At low keV energies, ionization mainly produces slow electrons in $p\sigma$ channel by the relative long-range interactions, while the fast electron can only be

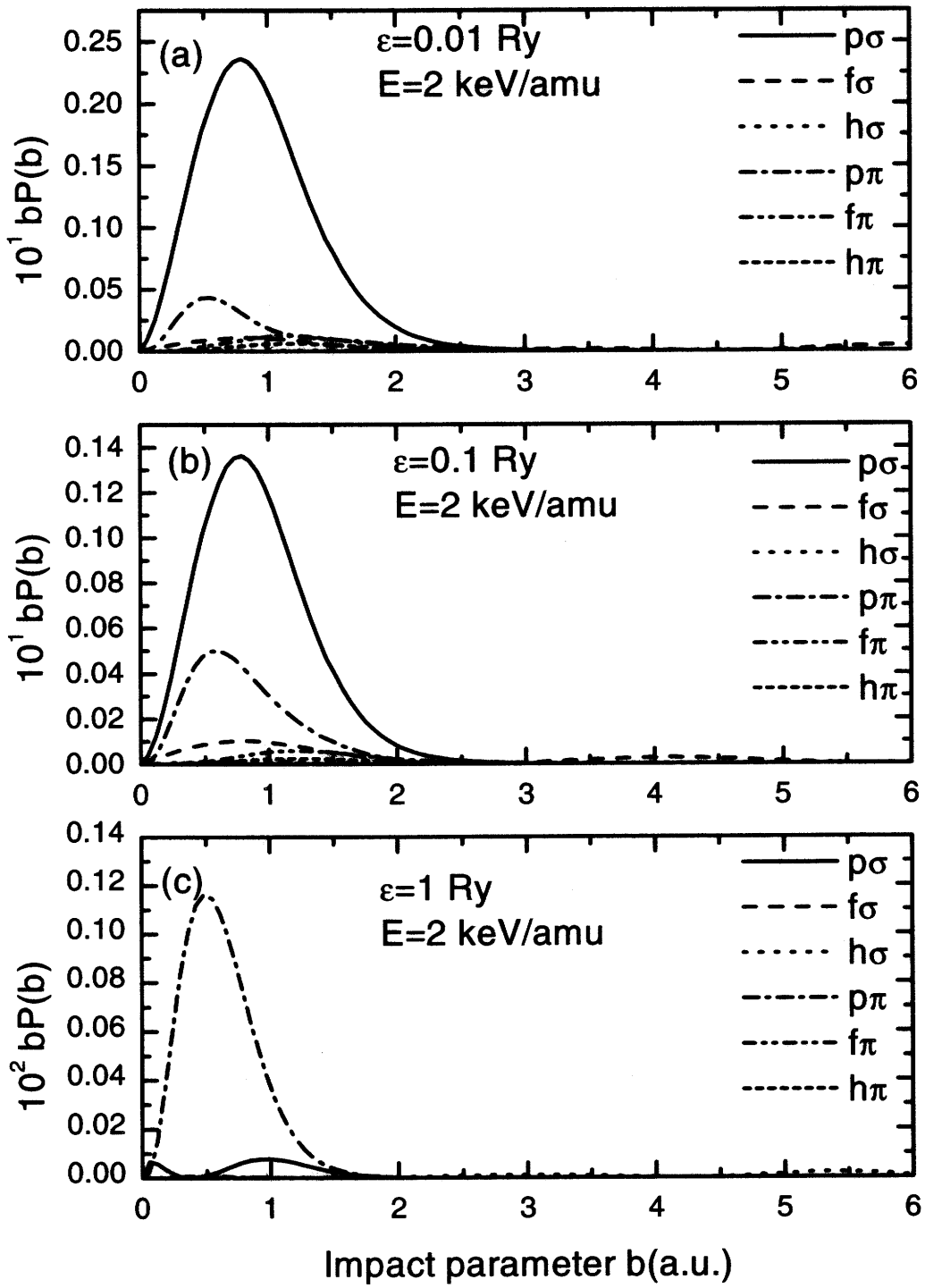

Figure 4.6 Weighted ionization probabilities as a function of the impact parameter b (atomic units) at the collision energy of 2 keV/amu. The three figures are for the ejected electron energies ϵ =0.01, 0.1 and 1 Ry from top to bottom. Calculations are performed on the basis set C.

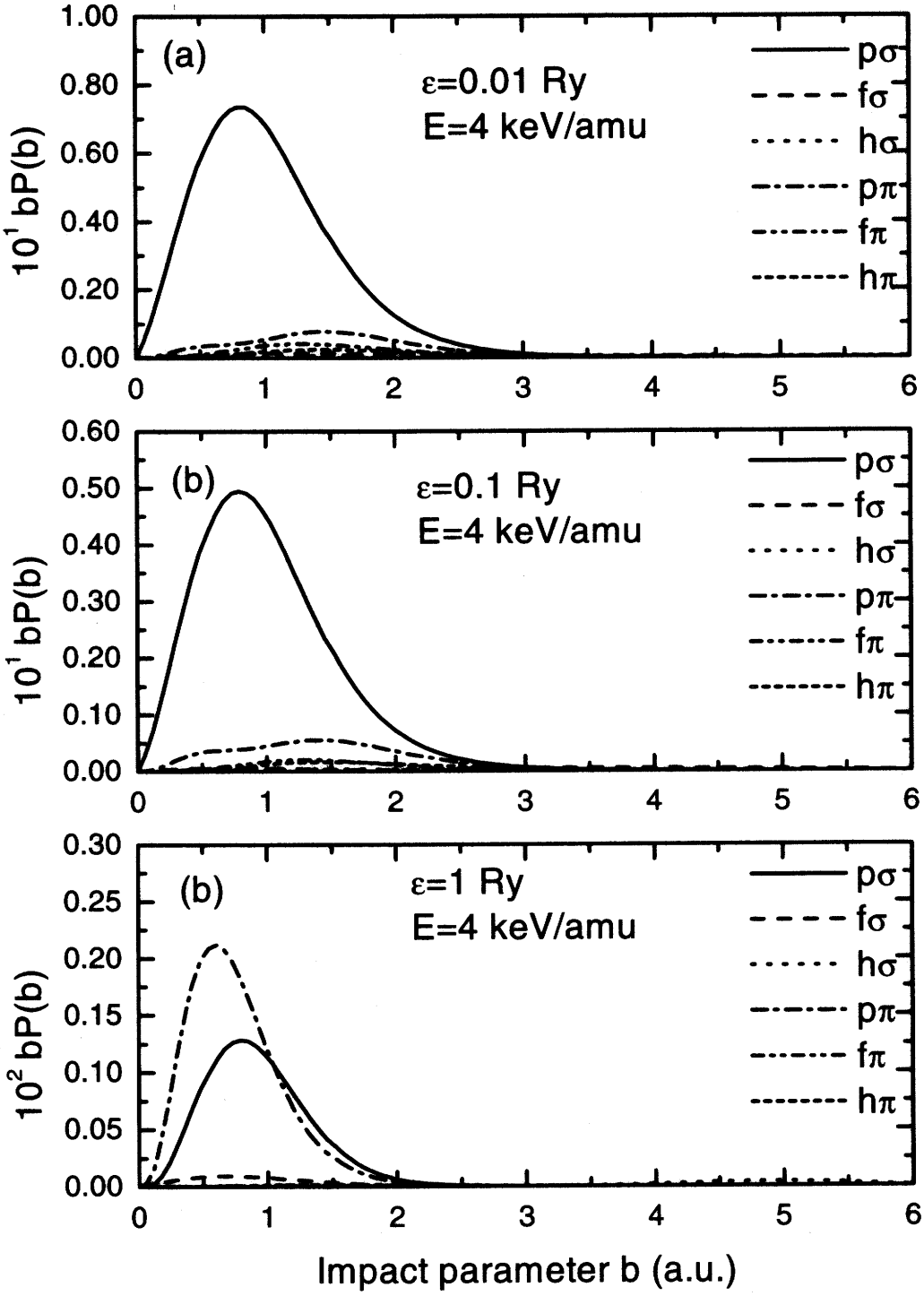

Figure 4.7 Same as Fig. 4.6 except $E = 4$ keV/amu.

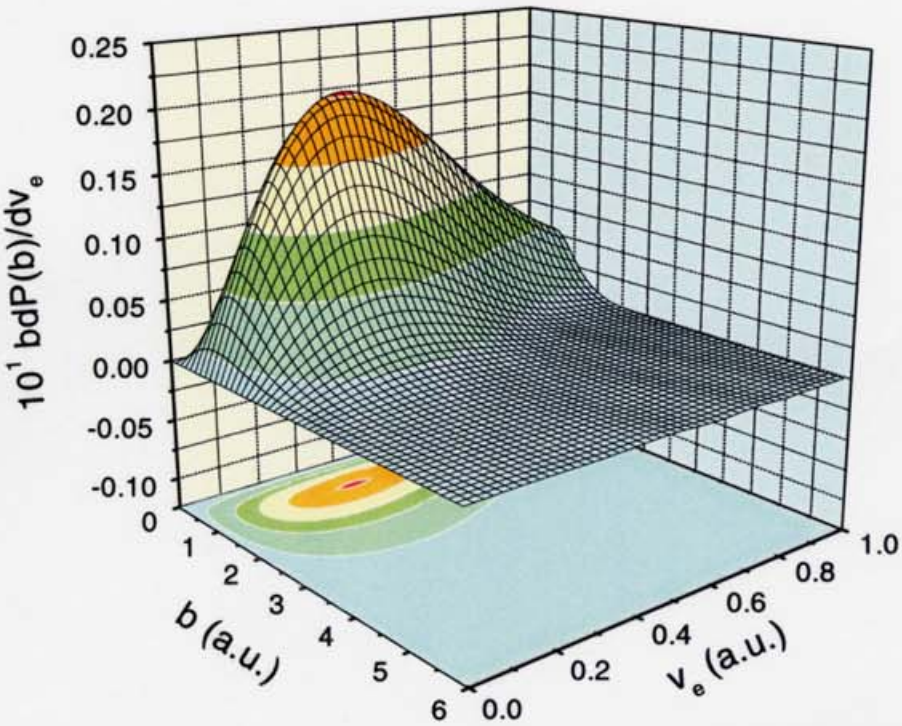

Figure 4.8 Weighted ionization probability $bP(b, E)$ as a function of ejected electron velocity v_e and impact parameter b at a collision energy $E = 4$ keV/amu (*i.e.* $V_p/2 = 0.28$ a.u.). In this figure, calculations are carried out with basis set C.

produced by the close collision through the angular coupling mechanism, as shown in the bottom panel of figures 4.6 and 4.7. The fast free electrons are in π states.

The distribution of ionization probability $bP(b, E)$ is shown in Fig. 4.8 as a function of ejected electron velocity v_e and impact parameter b for a collision energy $E = 4$ keV/amu. It can be seen that the $bP(b, E)$ peaks at $v_e \simeq 0.31$ a.u, $b \simeq 1$ a.u. and decreases rapidly with the increase of impact parameter b and final electron velocity v_e. Ionization probabilities are negligibly small for $b > 3$ a.u., and most of electron emissions take place as a results of close collisions with $b \sim 1$ a.u. The distribution of ejected electron is antisymmetric, a fast electron tail at $v_e \sim 1$ a.u. can be found, which is produced only by collisions with $b \sim 1$ a.u. Let us note at the moment that the mean radius of hydrogen atom is 1.0 a.u. and the half of collision velocity is about $V_p/2 = 0.28$ a.u. at $E = 4$ keV/amu. Thus the ionization is mainly caused by

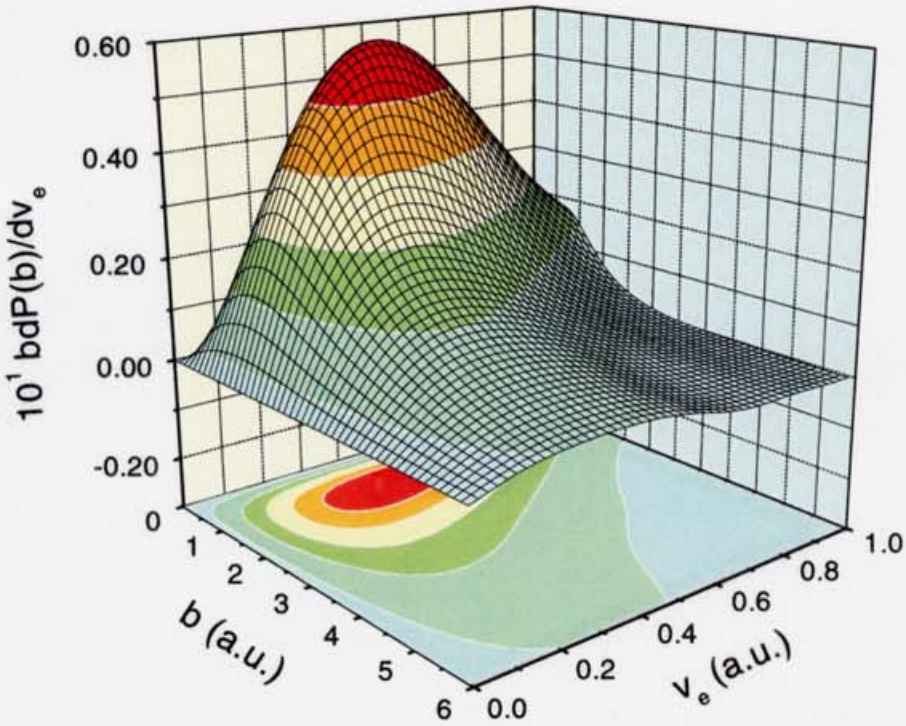

Figure 4.9 Same as Fig. 4.8 except $E = 10$ keV/amu (*i.e.* $V_p/2 = 0.45$ a.u.).

"head on" (on electron) collisions and results a free electron with half of the collision velocity, i.e. $v_e \simeq V_p/2$.

For a collision energy $E = 10$ keV/amu, we have plotted the ionization probability $bP(b, E)$ against the electron velocity v_e, and impact parameter b in Fig. 4.9. The maximum of $bP(b, E)$ is near $v_e \simeq 0.40$ a.u., $b \simeq 1.2$ a.u. on the final electron velocity and impact parameter plane. Now the half of collision velocity $V_p/2$ is about 0.45 a.u., and ejected electron velocity v_e is slightly smaller than $V_p/2$, on the opposite to Fig. 4.8. Spectra of the electrons emitted in ion-atom collisions have been recognized with peaks corresponding to soft electrons $v_e \simeq 0$, electron capture to the continuum $v_e \simeq V_p$, and binary encounter collisions $v_e \simeq 2V_p$, and perhaps an additional peak corresponding to the "saddle point" electrons $v_e \simeq V_p/2$ [2, 52]. Although the electron distributions in Figs. 4.8 and 4.9 peak near $v_e \simeq V_p/2$, there is no linear response to V_p for electron velocity v_e at the peak, say $v_e > V_p/2$ at the collision energy $E = 4$ keV/amu and $v_e < V_p/2$ at $E = 10$ keV/amu. Thus the maxima of ionization

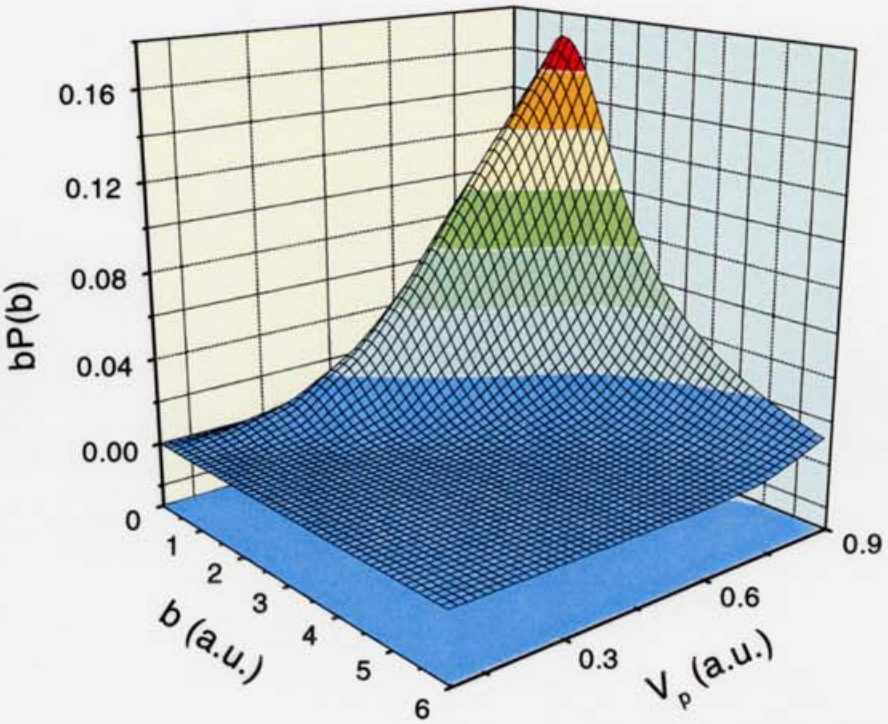

Figure 4.10 Weighted ionization probabilities $bP(b, E)$ as a function of impact parameters b and collision velocities V_P. In this figure, the ejected electron energy is $\epsilon = 0.1$ Ry, i.e. $v_e \simeq 0.32$ near the maximum of $bP(b, E)$ in the final electron velocity space. This calculation is performed on the basis set C.

probabilities in Figs. 4.8 and 4.9 should not be considered as a "saddle point" electron emission. With the collision energy increase, an amount of slow electrons can be produced by a collision with large impact parameter $b \geq 3$, as shown in this figure. These soft electrons are in $p\pi$ state. The height of fast electron tail increases to $\sim 35\%$ of the peak, comparing to 20% in Fig. 4.8, at $E = 4$ keV/amu.

Figure 4.10 shows the ionization probability distribution as a function of collision velocity V_P and impact parameter b for the given final electron energy $\epsilon = 0.1$ Ry, i.e. $v_e \simeq 0.32$ a.u. near the peak of $bP(b)$ in Figs. 4.8 and 4.9. Ionization probability increases with collision velocity increasing not only in magnitude, but also in the effective range of impact parameter b. At a relatively high collision energy, electrons can be ejected by a long-range interaction, in contrast to the slow collision emitting electrons only through "head on" collisions.

4.3 Ionization cross sections

As mentioned above, target excitation and charge transfer are important processes in the collision energy range below 10 keV/amu, which may influence the hydrogen ionization cross sections. Hence we compared our results with various calculations and experiments, namely for the excitation and capture into $2s$ and $2p$ levels of atomic hydrogen in Fig. 4.11. Our results are in good agreement with the measured data [103, 104] for collision energies between 1 and 7 keV/amu for target excitation or capture to projectile. Yet, at higher energies, our calculated $2p$ excitation cross section increases more quickly than the measured values of Barnett [103] (cf. Fig. 4.11). The agreement with the double-center close-coupling calculations of Toshima [4] is better than 20% in all cases. A very good agreement for electron capture to the projectile is found in case of the previous calculations by Kimura [101]: for instance the cross section at 5 keV in Ref. [101] agrees with our result within 5% for $2s$ charge transfer, and within 6% for $2p$ charge transfer. These are the upper bounds for all ejected electron energies; e.g. the 6% difference for $2p$ charge transfer corresponds to the ejected electron energy $\epsilon = 0.01$ Ry, and it decreases to only $1\sim 2\%$ difference at $\epsilon = 1.0$ Ry.

Transitions between discrete states, which occur at large values of R in fact do cause a slower convergence of the capture/excitation cross sections. This particular case, however, does not influence our ionization cross sections, because the ETF-corrected couplings to the ionization continuum practically vanish at large values of R.

The total ionization cross sections computed with the basis sets A, B, and C are shown in Fig. 4.12: g components in the upper panel, and u components in the lower panel. The corresponding ratios of TICS's with different basis set are plotted in Fig. 4.13. From the two figures, it is clearly seen that in case of g components the upper levels incorporated in basis set C enhance the total ionization cross sections by ~ 2 times at the collision energies above 2 keV/amu. This means that the dominant mechanism for ionizing a $1s\sigma_g$ electron does not involve direct excitation by a single impulse, but a "ladder-climbing" process in which the electron is gradually detached in a series of small impulses, and electron does not come out with large amounts of excess energy. However, the case of u components is completely different, TICS's with basis set C are much smaller than those of basis set A below 6 keV/amu, at $E = 2$

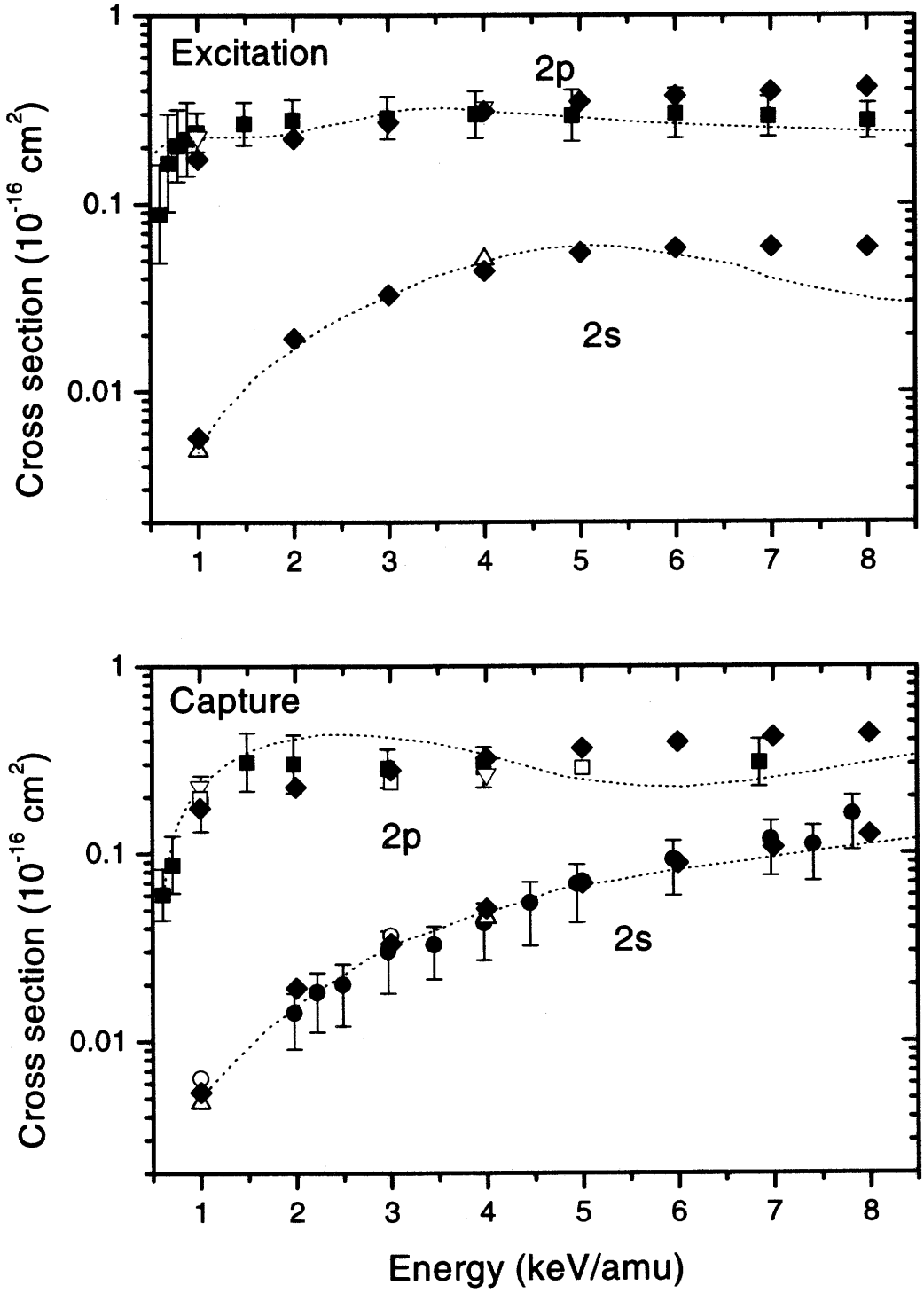

Figure 4.11 Cross section comparison (H-p system) for (a) excitation to 2s and 2p levels and (b) capture into 2s and 2p levels of atomic hydrogen in collisions with slow protons. Solid squares, measured values of Barnett [103]; solid circles, measured values of Morgan *et al.* [104]; dotted lines, 3ACO results of Mclaughlin *et al.* [53]. open triangles, 2ACO results of Toshima [4]; open circles, MO results of Kimura *et al.* [101]; solid diamonds, present calculations

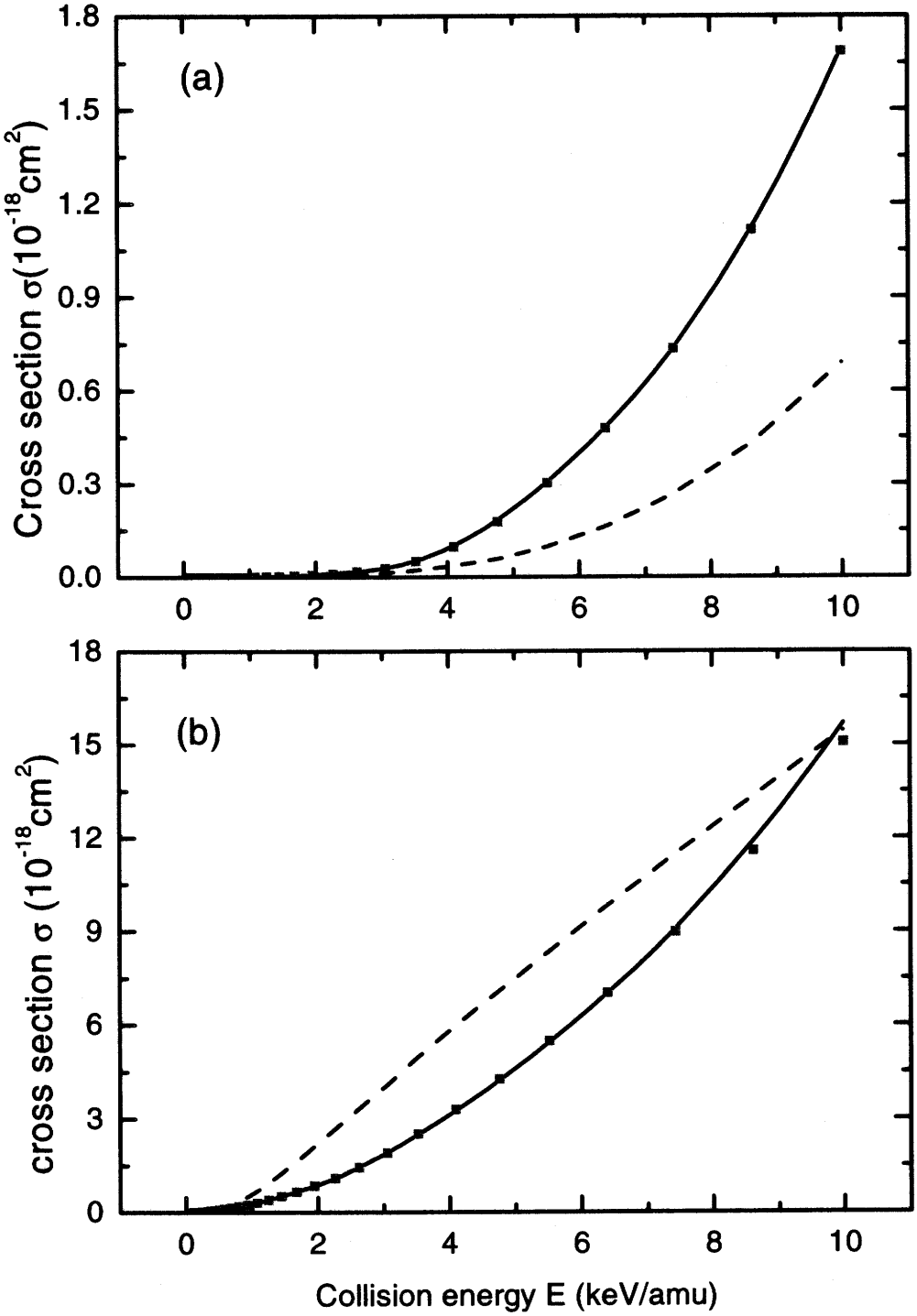

Figure 4.12 Total ionization cross sections in p-H collisions: dashed lines, set A; solid scatters, set B; solid lines, set C. In the figure, g components are plotted in the upper panel and u components in the lower panel.

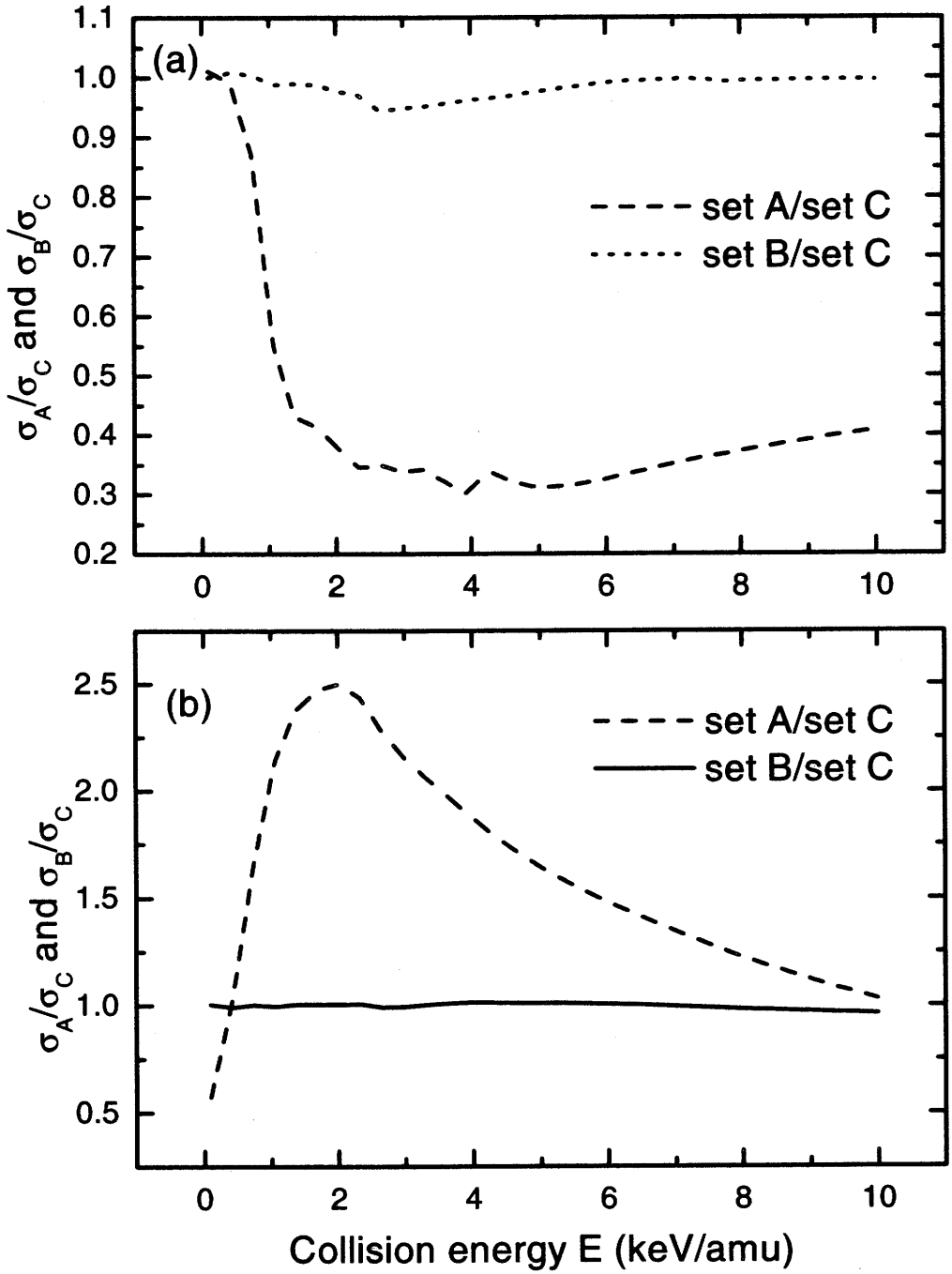

Figure 4.13 Ratios of total ionization cross sections in p-H collisions: dashed lines, set A over set C; solid lines, set B over set C. In the figure, g components are plotted in the upper panel and u components in the lower panel.

keV/amu with the discrepancy up to factor of 2.5. In this case, the upper levels are a trap instead of a step stone. As stated in Sec. 4.1, ionization is driven by short range couplings and takes place only at small internuclear separations. The potential curves of bound states, especially near the united atom limit, play an essential role in interpretation of ionization dynamics. $1s\sigma$ lies at far below of any other bound or continuum states, but the excitation to an upper lying state significantly reduces the energy distance to the continuum, and thus effectively enhances the interaction with continuum states. In u family, the strongly coupled states $2p\pi_u$ and $2p\sigma_g$ are degenerated in the united atom limit, therefore excitation to $2p\pi_u$ does not reduce the potential much. The strong angular coupling $\langle 2p\pi_u|H(ang)|2p\sigma_u\rangle$ introduces an important flux loss to $2p\sigma_u$ and decreases ionization probabilities, see also Fig. 4.5. Then the completely different roles of upper levels in ionization of g and u electrons is determined by the potential curves of bound states in H_2^+ at the united-atom limit. The difference between basis sets B and C is rather small, the ratios of TICS's differ from unit not larger than a few percent.

Fig. 4.14 shows the total ionization cross sections which we computed using the basis set C in comparison with the various theoretical calculations and the available experimental data. Our cross sections are one time smaller than those of the triple-center atomic orbital close-coupling calculations of Ref. [1] above; they exhibit closer agreement at collision energies lower than 1.5 keV/amu. The hidden crossing calculation including S and T promotions and the radial decoupling mechanism [52] is 30% higher than our results at 10 keV/amu. Their cross section decreases more slowly with the energy decreasing, and thus at 1 keV/amu the difference from our calculations is as high as a factor of 6. Yet, our values are in better agreement with the hidden crossing method including only S and T promotions [2], with the discrepancies better than 30% in usual. This holds except for the collision energy below 2 keV/amu, where the hidden crossing calculations decrease faster, and the cross sections of Ref. [2] are by a factor of two smaller than the present results at 1 keV/amu. Our calculations agree well with the two center close-coupling calculation of Toshima [4] in the range 4-10 keV/amu, but Toshima's values become smaller than us and dropped much faster below 4 keV/amu. The present results are also compared with the measurements of Pieksma *et al.* [2] and Shah *et al.* [1]. Our values come at 25% below the measured cross sections of Ref. [2] at 6 keV/amu, and decrease much more rapidly with collision energy decreasing, the discrepancies up to a factor of 6 at lowest considered collision

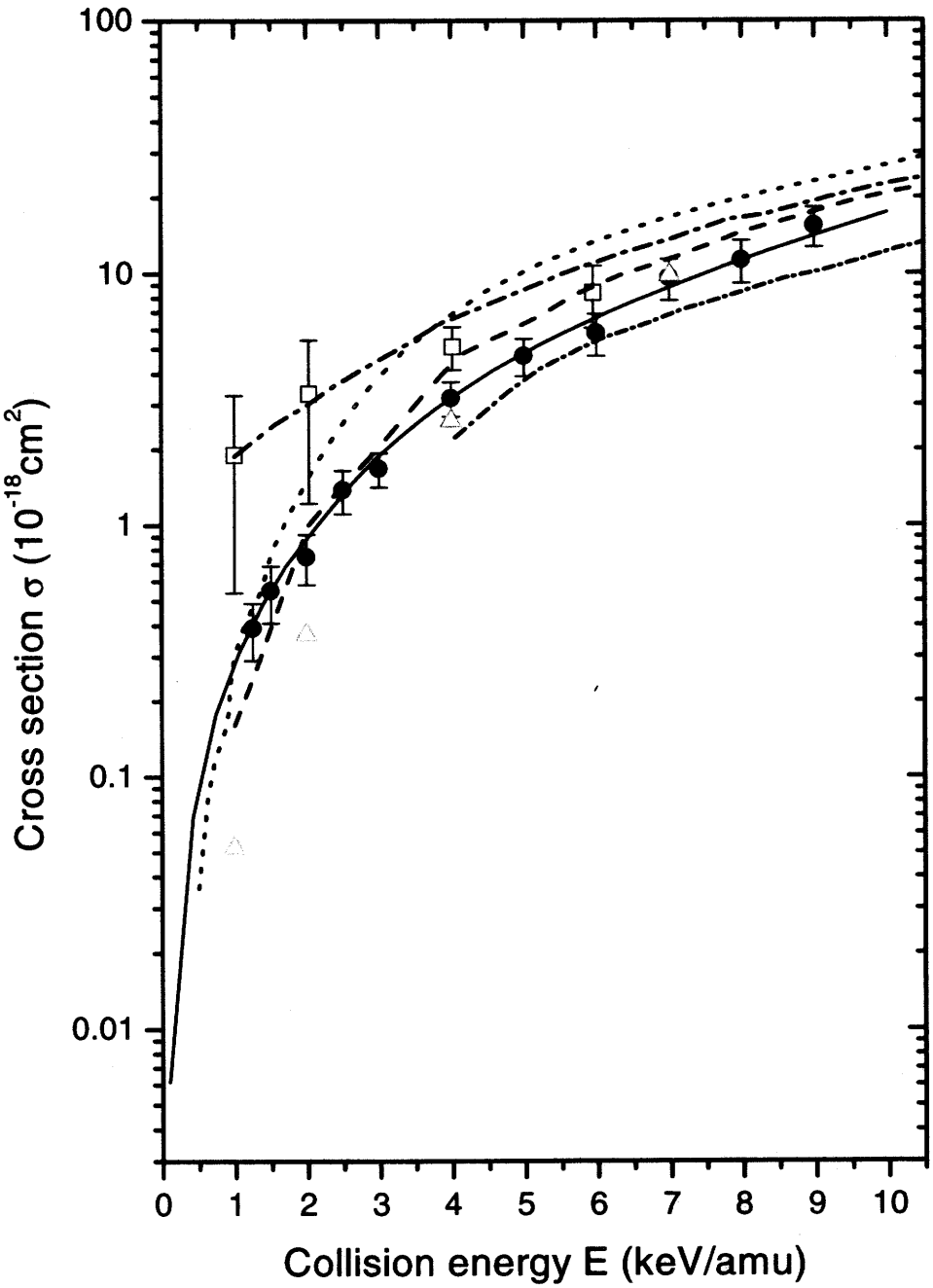

Figure 4.14 Total ionization cross sections of proton-hydrogen system: solid circles, measured data of Shah *et al.* [1]; open squares, measured data of Pieksma *et al.* [2]; dash-dotted lines, results of hidden crossing with radial-decoupling[52]; dashed lines, hidden crossing without radial-decoupling[2]; dotted lines, 3CAO of Machauglin et al.[1]; up triangles, 2CAO of Toshima [4]; short dash dotted lines, 2CAO of Fistsch et al.[54]; solid lines, present MO with basis set C.

energy 1 keV/amu. However, our results are in an excellent agreement with the recent experimental data of Shah *et al.* [1], since they lie within the experimental error bars in the entire energy range considered. Such an agreement should be expected when the important direct and indirect ionization mechanisms are all included, boundary conditions treated properly, and the numerical accuracy of all calculations sufficiently maintained.

The total ionization cross section in p-H system were already plotted in Fig. 2.1 for a broader energy range 0.1-1000 keV/amu, in which various calculations are compared. TICS's from Toshima [4] are 20% higher than the experimental values [6,7] around $E = 100$ keV/amu, and they are in a good agreement at the high energy region. Triple center close-coupling calculations [1,53] predicted the cross sections at low to intermediate energies to be larger than the measurement data [1,7] up to a factor of 2, and they decrease much faster at collision energies above 50 keV/amu. They are also found to oscillate with collision energies. CDW-EIS, the continuum distorted wave eikonal initial state approximation, is a high energy theory by Crothers and McCann [55], who obtained their cross sections in a good agreement with the measurements by Shah *et al.* [6,7] for energies above 25 keV/amu. All the above theories predicted TICS's decreasing much more rapidly than our results and the experimental data [1] below 1.5 keV/amu.

The accurate total ionization cross sections by the ETF-modified close-coupling expansion in Fig. 4.14 is not the only principal result of this section. In Fig. 4.15, we plot the single-differential cross sections as a function of ejected electron energies ϵ and collision energies E. Cross sections of g and u components are shown in the upper and lower panels respectively. Ionization cross section decreases rapidly with the final electron energy increasing and collision energy decreasing. Ionization is significant only when collision energies E is above 3 keV/amu for g components and 1 keV/amu for u components. At a collision energy $E = 10$ keV/amu, the differential cross sections of $\epsilon = 0.01$ Ry is about two orders of magnitude greater than that of $\epsilon = 1.0$ Ry. Differential cross section $d\sigma/d\epsilon$ of u components is about one order of magnitude greater than that of g components at their maxima. We have projected the differential cross sections $d\sigma/d\epsilon$ on the bottom plane in this figure. There is a region in the two projections in which for a constant $d\sigma/d\epsilon$ the ratio of ϵ/E is a constant. It shows that a small amount of electrons gains energies from incident protons in a single impulse, and those electrons come out with large excess energy. Such process

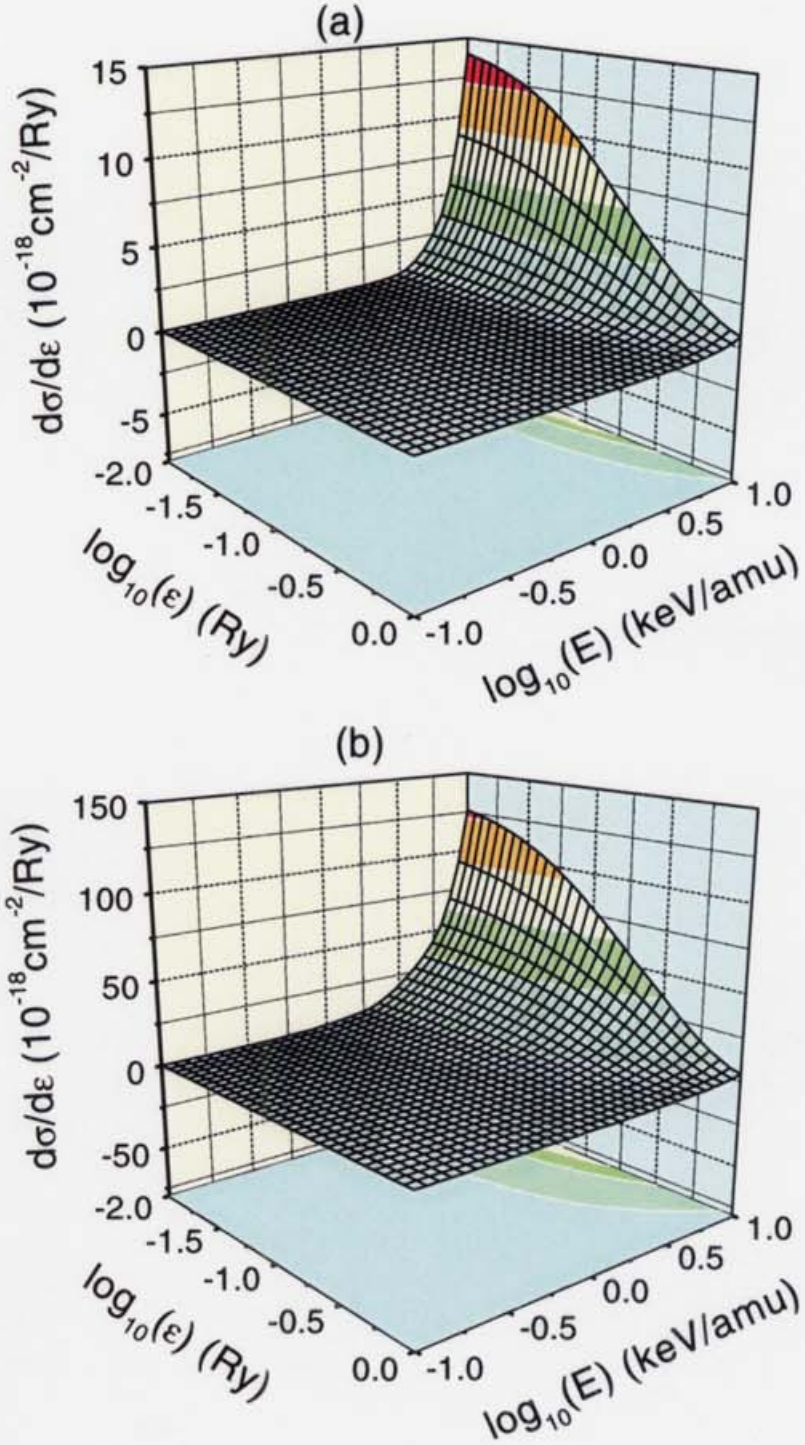

Figure 4.15 Single-differential ionization cross sections of proton-hydrogen system: the g and u components are shown in the upper and lower panels, respectively. Numerical values are obtained by present ETF-modified molecular close-coupling calculations with basis set C.

is analogous to electron capture to continuum in which the projectile transfers a part of its kinetic energy to the target in a constant rate and results free electron with $v_e \sim V_p$.

Fig. 4.16 shows the distribution of partial ionization cross sections as a function of collision energy. The energy of ejected electron is taken as $\epsilon = 0.01\ Ry$. This figure represents our previous statement that the ionization cross sections are significant only for two or three channels either for g components or for u components. In case of g components, $s\sigma$, $d\sigma$ and $d\pi$ are the important channels below 4 keV/amu, but the partial ionization cross sections of $s\sigma$ channels increase much more rapidly than the other two, and exceed them by order of magnitude at E=10 keV/amu. The channels $p\sigma$, $p\pi$ and $f\pi$ are important in the case of u components, and the partial ionization cross sections of $p\pi$ and $p\sigma$ are almost the same at the highest energy considered, 10 keV/amu.

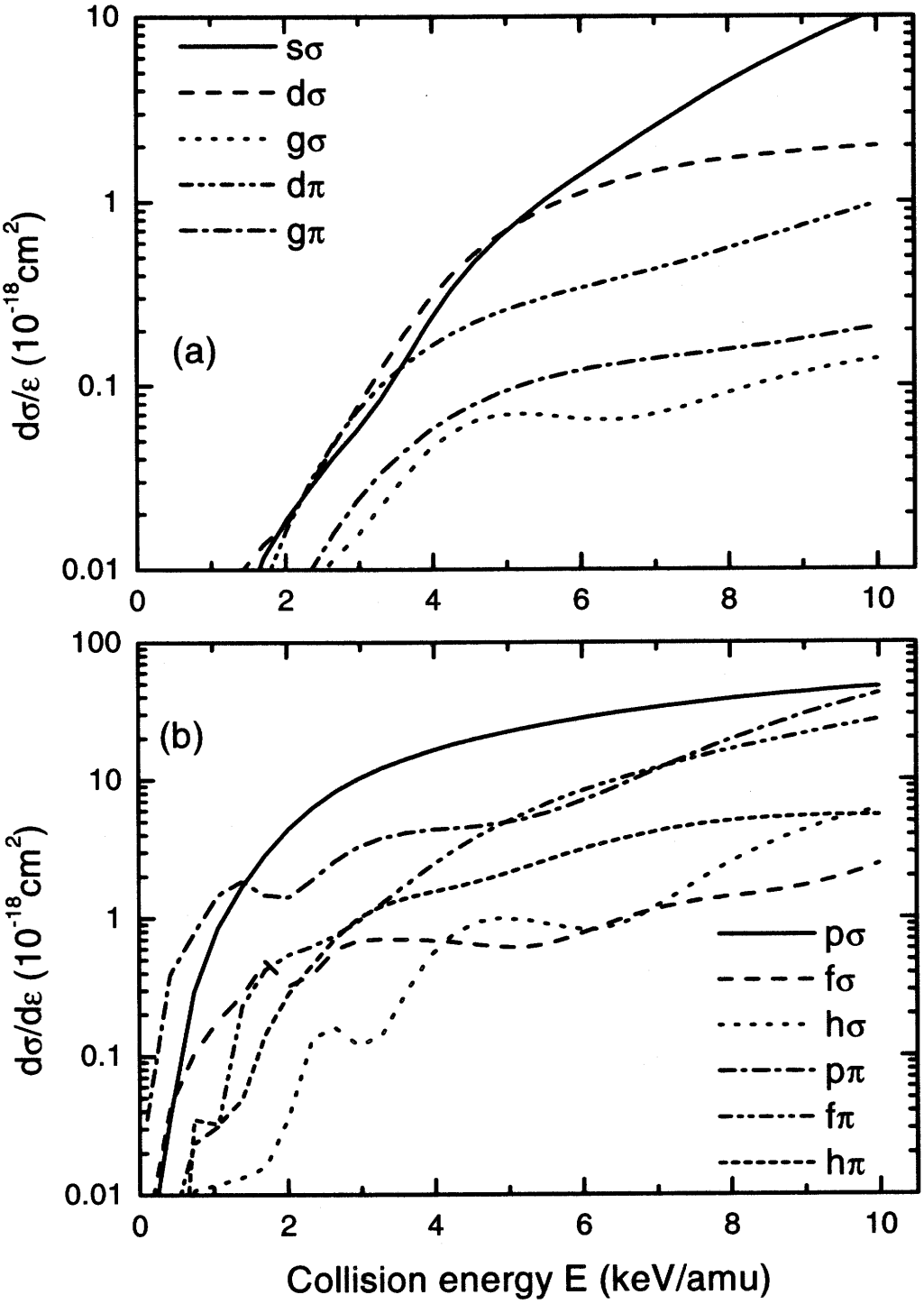

Figure 4.16 Partial ionization cross sections as a function of the collision energy E for the ejected electron energy $\epsilon = 0.01$ Ry. Upper panel: g components, lower panel: u components.

5.0 Study of Ionization in $He^{2+} + H(1s)$ collisions

5.1 Potential curves and couplings

Figure 5.1 shows electronic energy $\epsilon_k(R)$ versus R for 21 molecular states of HeH^{2+}. Now the initial condition is replaced by

$$a_k(t = -\infty) = \delta_{1k}, \tag{5-1}$$

where index "1" designates the initial states, which is $2p\sigma$ for He^{2+} + H collision. To compute the ionization cross sections, we have carried out systematic calculations with basis sets A and B, as listed in Table 5.1. Comparing the numerical results with different basis sets allows us to study the convergence of ionization cross sections with the basis size. The continuum component is common in the basis sets A (direct ionization), and B (indirect ionization), which contains 32 energies below 2.0 Ry for each partial wave; then the total continuum states are accounted for up to 352. Within the straight line approximation, we have solved the coupled differential equations, Eq. (3-26), for 100 impact parameters ranged in $0.0 - 10.0$ a.u. at 32 collision energies from 1-16 keV/amu.

Employing the ETF's of Ref. [105], we have computed the nonadiabatic couplings for both discrete to discrete and discrete to continuum transitions. The corrections arising from ETF's exactly cancel the spurious asymptotic couplings and produce substantial reductions in the size and effective range of most coupling matrix elements. Since the discrete-discrete and discrete-continuum couplings have been discussed by Kimura *et al* [101] and Rankin *et al.* [102] respectively, these couplings are not shown in detail here. Rather as an survey of some of the results and as an illustration, see Figs. 5.2 and 5.3.

The energy dependence of couplings $\langle \epsilon s\sigma | H(rad) | 1s\sigma \rangle$ and $\langle \epsilon p\sigma | H(rad) | 2p\sigma \rangle$ can be seen from Figs. 5.2 and 5.3. The couplings both from $2p\sigma$ and $1s\sigma$ are much less sensitively dependent on the energy of continua electron than those of H_2^+ system; the size of couplings from $2p\sigma$ is reduced by about one-third with the continua electron energy increase from 0.02 Ry to 1.0 Ry; couplings from $1s\sigma$ are changed only by $\sim 10\%$ in size. The less sensitive energy dependence of couplings is still analogous to the potential curves of bound states, as indicated in Eqs. B-9 and (B-10).

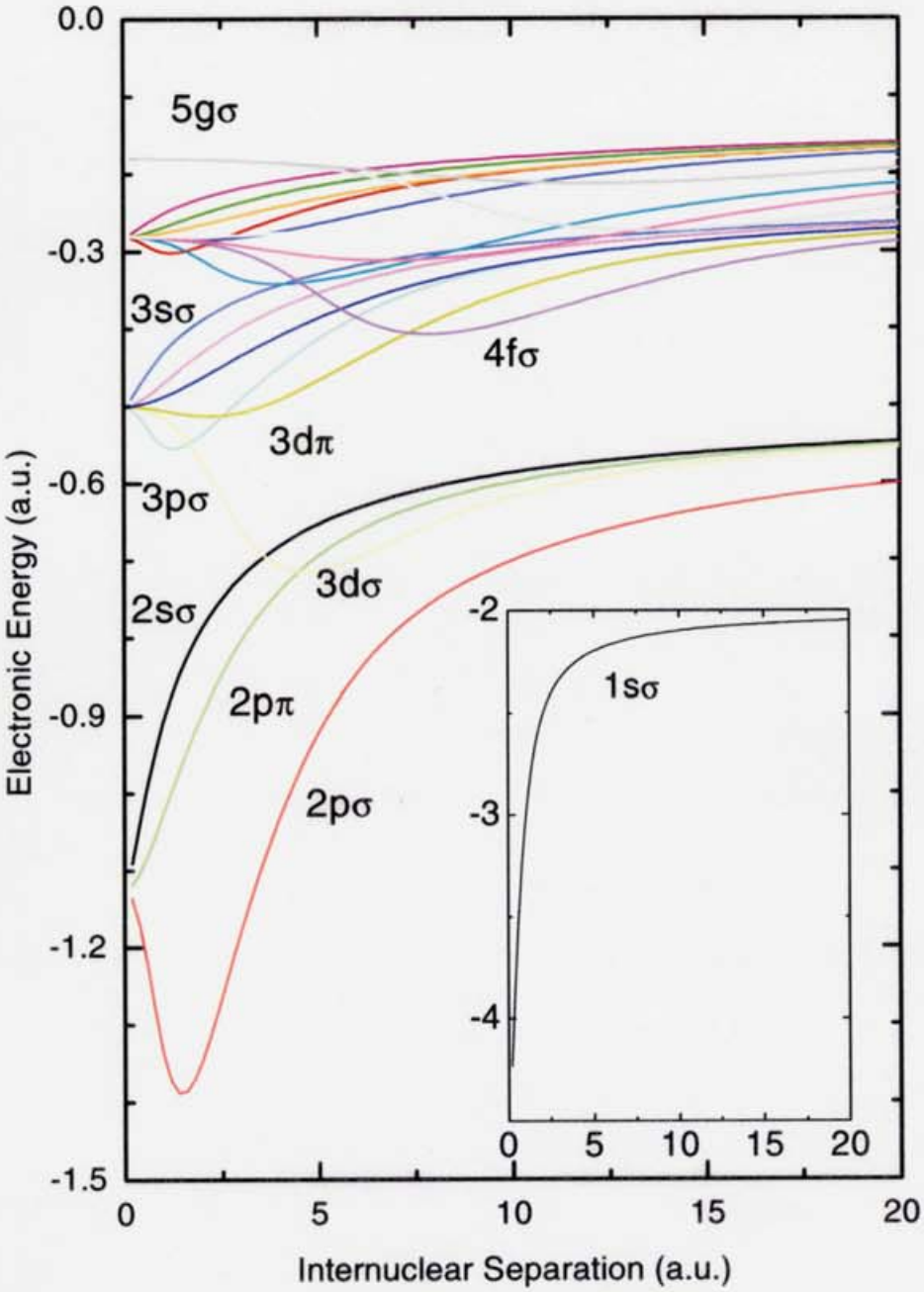

Figure 5.1 Electronic energy $\epsilon_k(R)$ (a.u.) versus R, for 21 molecular states of HeH^{2+}

Table 5.1 Molecular basis sets of calculations for $He^{2+} + H(1s)$ collision.

Sets	Molecular basis states	Limiting atomic levels	Number of all states
continuum:	$\|\epsilon s\sigma\rangle$		
	$\|\epsilon p\sigma\rangle$, $\|\epsilon p\pi\rangle$		
	$\|\epsilon d\sigma\rangle$, $\|\epsilon d\pi\rangle$		
	$\|\epsilon f\sigma\rangle$, $\|\epsilon f\pi\rangle$		
	$\|\epsilon g\sigma\rangle$, $\|\epsilon g\pi\rangle$		
	$\|\epsilon h\sigma\rangle$, $\|\epsilon h\pi\rangle$		
	11 partial waves, for 32 energies		11×32 =352
and bound:	all above, plus	all above, plus	
A:	$\|2p\sigma\rangle$	$H(1s) + He^{2+}$	353
B:	all above, plus		
	$\|3d\sigma\rangle$	$H + He^{+}(n = 2)$	
	$\|2p\pi\rangle$	$H^{+} + He^{+}(n = 2)$	
	$\|2s\sigma\rangle$	$H^{+} + He^{+}(n = 2)$	
	$\|1s\sigma\rangle$	$H^{+} + He^{+}(1s)$	
	$\|3p\sigma\rangle$	$H^{+} + He^{+}(n = 3)$	
	$\|3p\pi\rangle$	$H^{+} + He^{+}(n = 3)$	
	$\|3d\pi\rangle$	$H^{+} + He^{+}(n = 3)$	
	$\|4f\sigma\rangle$	$H + He^{+}(n = 3)$	
	$\|4d\sigma\rangle$	$H(n = 2) + He^{2+}$	
	$\|4f\pi\rangle$	$H(n = 2) + He^{2+}$	
	$\|5g\sigma\rangle$	$H(n = 2) + He^{2+}$	364

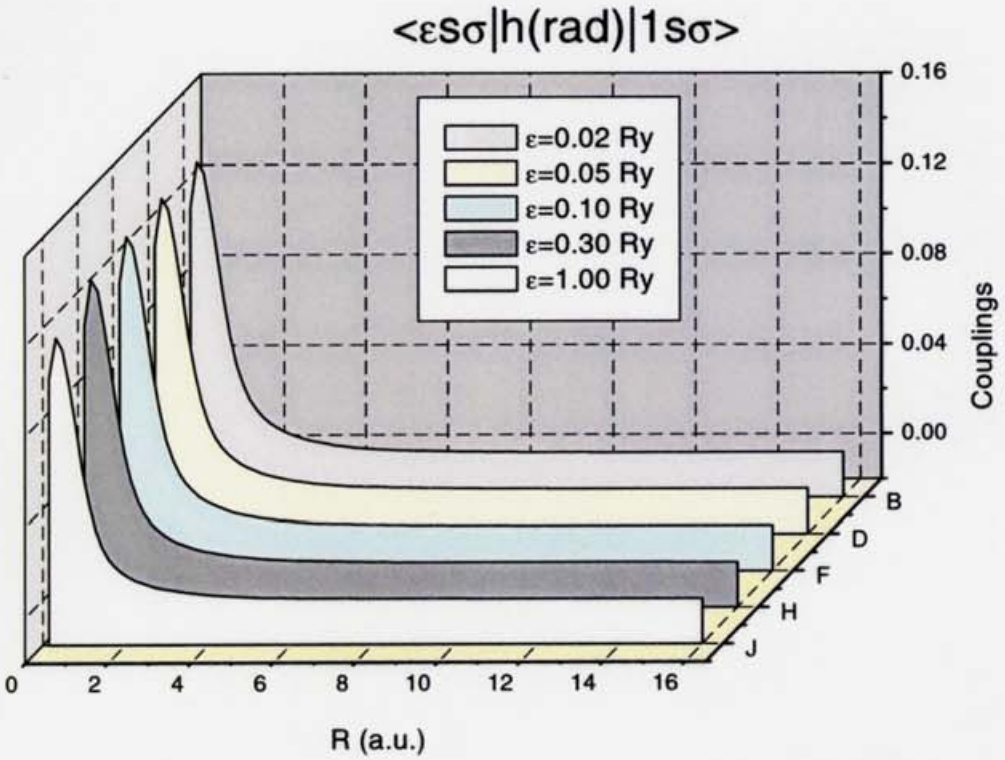

Figure 5.2 Couplings to the $|\epsilon s\sigma\rangle$ state for the final electron energies $\epsilon = 0.02$, 0.05, 0.10, 0.30 and 1.00 Ry from the $1s\sigma$ states in HeH^{2+} molecule, where the corrections arising from the MO-ETFs have included.

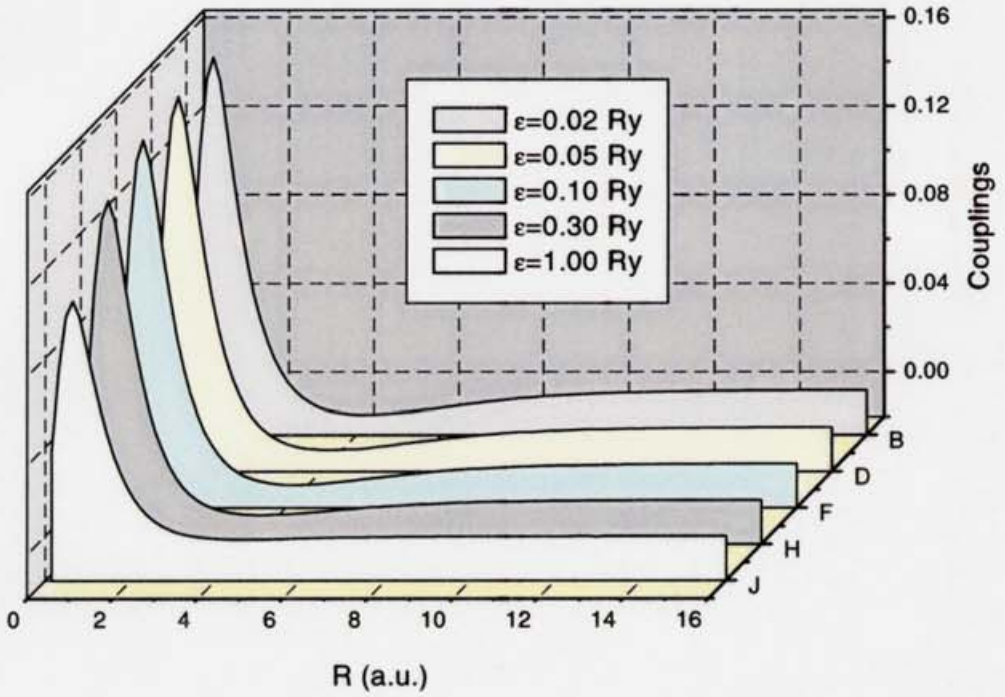

Figure 5.3 Same as Fig. 5.2 except initiated from $2p\sigma$.

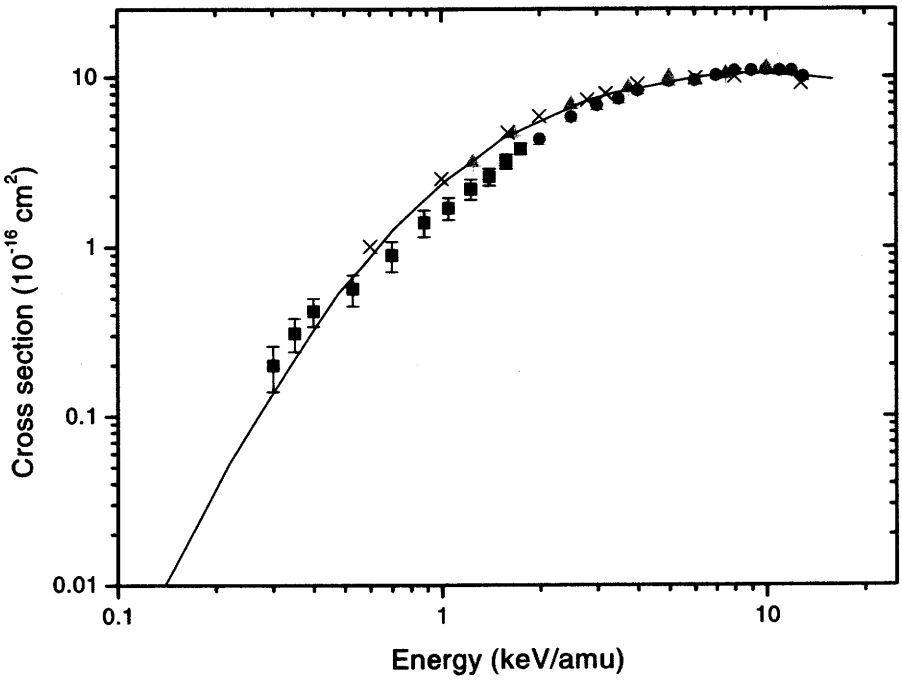

Figure 5.4 Charge transfer cross sections for He^{2+}+H(1s) $\rightarrow$ He^{+}(2p)+H^{+} collision at low energies. In the figure, solid squares: measured data of Hoekstra *et al* [106]; solid circles: measured data of Hoekstra *et al*[107]; upward triangles: measured data of Ciric *et al*[108]; crossing symbols: results of MO expansion with common translation factors by Errea *et al* [109]; solid lines: present results.

5.2 Ionization cross sections

Charge transfer cross sections of present study are shown in Fig. 5.4 for the collision $He^{2+} + H(1s) \rightarrow He^{+}(2p) + H^{+}$, and in Fig. 5.5 for the collision $He^{+}(1s) + H^{+} \rightarrow He^{2+} + H(1s)$ at low- to intermediate-energy region. The very good agreement with experimental results [106, 107] can be found for both collisions, and a good agreement is also seen as compared to other theoretical calculations [109]. The good charge transfer cross sections support partly the ionization cross sections, since the direct comparison to measured data is limited (experimental values are not available below 18.4 keV/amu).

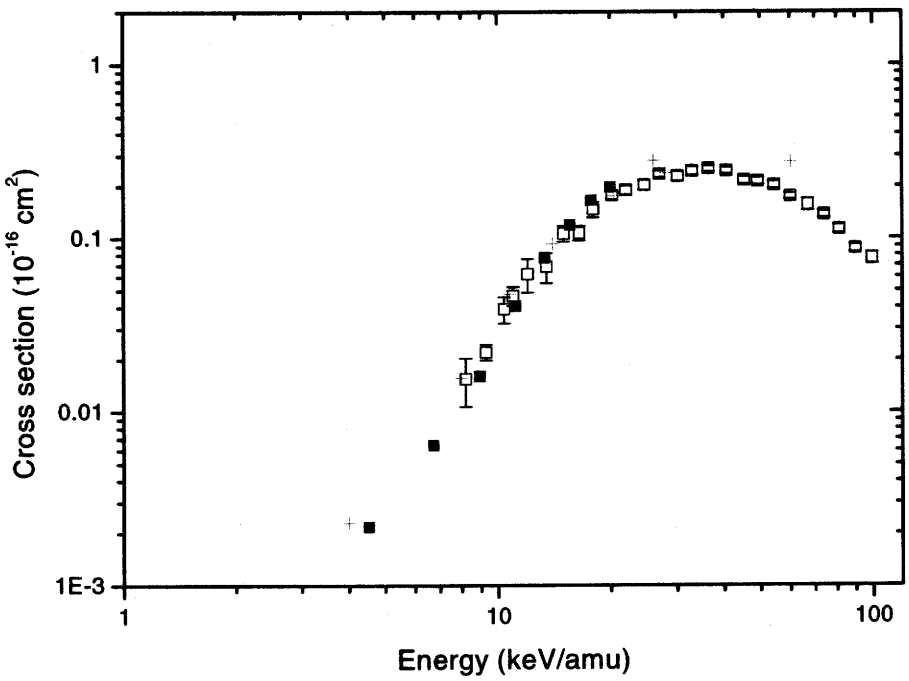

Figure 5.5 Charge transfer cross sections for $He^+(1s)+H^+ \rightarrow He^{2+}+H(1s)$ collision at low energies. In the figure, open squares: measured data of Rinn *et al* [110]; cross symbols: results of MO expansion with common translation factors by Errea *et al* [109]; solid squares: present results.

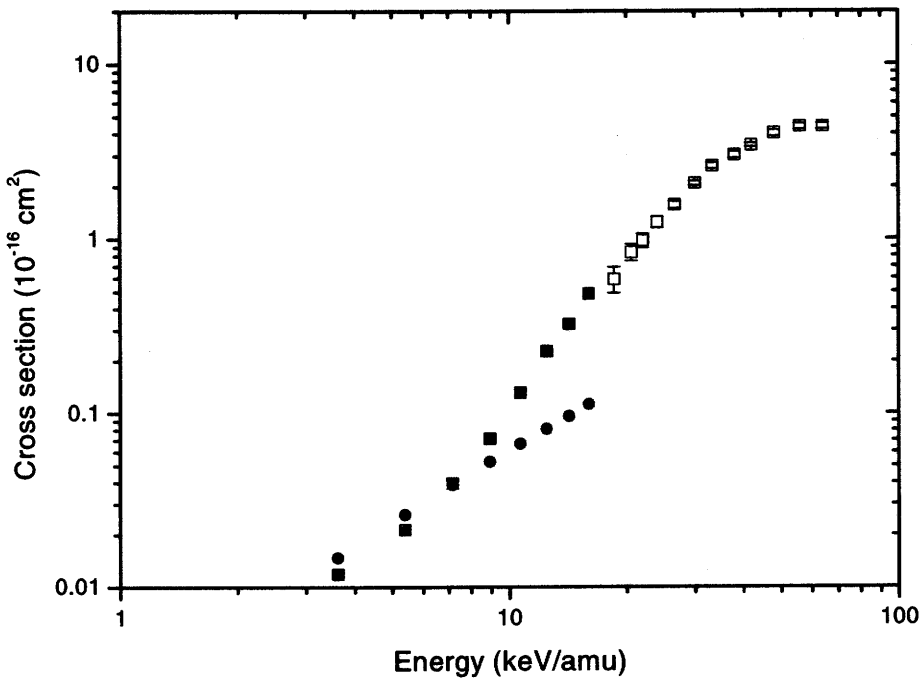

Figure 5.6 Total ionization cross sections in $He^{2+}H(1s)$ collision at low energies. Open squares: experimental results of Shah *et al* [51]; solid circles: calculation results from this study with basis set α (direct ionization); solid squares: calculation results from this study with basis set β (with contributions through intermediate states)

.

I note that the charge transfer transition probabilities in He^{2+}+$H(1s) \rightarrow He^{+}(2p)$+ H^{+} and $He^{+}(1s) + H^{+} \rightarrow He^{2+} + H(1s)$ were found to oscillate very quickly below 1 keV/amu, and the interaction region is also large due to the energy degeneracy among $H(1s)$ and $He^{+}(n = 2)$. So the calculation is quite heavy for the low energy part especially below 1 keV/amu. In the above calculations 400 impact parameters in the range $0 - 15.0$ are employed, and further checked by calculation on 1000 impact parameters in the same range. Resulted cross sections are plotted in Figs. 5.4 and 5.5. To avoid the heavy calculations for slow collisions, the total ionization cross sections are calculated for energies above 1 keV/amu, which are more practicaly important.

Total ionization cross sections of atomic hydrogen by slow He^{2+} are shown in Fig. 5.6, and compared with the experimental values of Shah *et al* [51]. Unfortunately,

the measured ionization cross sections are not available at low energies, and my calculation can not be easily extended to that high energy range. And hence, the quantitative comparison is limited. Although the energy ranges of my calculation and experimental data do not overlap, we can still point out that the trend of the calculated results is similar to the measured data. They connect smoothly near 18 keV/amu. The total ionization cross sections from calculation with basis set α are much smaller than those from converged basis set β. Here excitation via a sequence of higher levels, which may be called as indirect ionization, is the dominant mechanism for liberating the bound electron from hydrogen atom during the collision with He^{2+}. It is completely different from the case of ionization of hydrogen atom by proton, where the direct ionization is much more important. The difference is due to the complex interference between the intermediate states and the initial states.

6.0 Conclusion

In the first part of the thesis, I have provided accurate single-differential and total ionization cross sections on proton-hydrogen collision system at 0.1-10 keV/amu. The close-coupling expansion with ETF's modified H_2^+ molecular states was used. It is the first calculation using this method for the ionization problem, based on the direct evaluation of all couplings between the bound and continuum states. The results are in an excellent agreement with the recent experiments of Shah *et al.* [1], but differ from the other measurements by Pieksma *et al.* [2].

From a methodological point of view, we show that the appropriate ETF's not only exactly cancel the spurious asymptotic behavior of nonadiabatic couplings, but also systematically reduce the size and effective range of most coupling matrix elements. With the ETF-corrected molecular basis, the accurate ionization cross sections can be obtained by a calculation in a small region of configuration space and coordinate space. For H_2^+ system in the range 0.1-10 kev/amu, a good convergence has been achieved with a basis including 10 bound states and 11 continuum partial waves.

In addition, we find that the upper levels play a completely different role in H ionization for the g and u components. In case of g components, an excitation sequence via upper levels is the dominant mechanism for the ionization, which enhances the total ionization cross sections (as compared to the direct ionization process) by more than two times at the collision energy E =10 keV/amu. In case of u components, the excitation to upper levels reduces the total ionization cross section significantly, especially the excitation to $2p\pi_u$ molecular state. Since the total ionization cross section is mainly decided by u components, we conclude here that the upper levels are a "trap" on the way of electron going to ionization continuum, in contrast the general recognized "ladder". Using the ETF-modified MOCC method, we have a tool to examine the role of each molecular state in the ionization process in a systematic way.

Within the same approach, collision system of atomic hydrogen by slow He^{2+} was also treated at the energy range 1-16 keV/amu. A good convergence has been achieved with a basis including 12 bound states and 11 continuum partial waves at 32 continua electron energies, which resulted in accurate charge transfer and ionization cross sections. The present electron capture cross sections in $He^{2+} + H(1s)$ are found

to be in a very good agreement with the experimental values [25, 106, 107, 110] and other theoretical calculations. Although the energy range of this study does not overlap with the experiment of Ref. [51], the calculated ionization cross sections tie smoothly with the experimental ones from below, at about ~ 18 keV/amu. It is found that the indirect ionization is a more important mechanism than the direct process, which is dominant in the $p - \mathrm{H}$ system. The present method is readily applicable to further physical systems of interest, such as $p + \mathrm{Li}$ and/or $\mathrm{He} + \mathrm{Li}$.

PART II

Charge exchange recombination spectroscopy

7.0 Review of Charge Exchange Spectroscopy and Pellet Injection

Charge exchange recombination spectroscopy (CXRS) is based on the atomic process in which a fully ionized ion (A^{q+}) captures an electron from a hydrogen atom present in a neutral heating beam, results in a lower charged ion ($A^{(q-1)+}$) in an excited state (nl), and then this excited ion ($A^{(q-1)+}(nl)$) decays through photon emission. The emitted photons carry the information about the spatial and velocity distributions of fully ionized A^{q+} ions. The technique has been widely used to diagnose the ion temperature, the plasma rotation, the radial electric field and so on (see references [111–115] and references therein). Recently, in combination with the impurity pellet injection, CXRS has been extended to a study of particle transport in magnetically confined plasmas. Several successful experiments have been reported from Heliotron E [111], CHS [17] and LHD [116] plasmas based on lithium pellet injection. The injected lithium pellet ablates near the plasma center, depositing exotic impurities which are predominated by fully ionized Li^{3+} in a localized region. From the time dependent behavior of the line emisson of hydrogen-like lithium, Li^{2+} or Li III, the diffusion coefficient of the ions is obtained as well as plasma parameters. Details of the lithium pellet injection experiments are given in [17, 111, 116].

In the experiments mentioned above, the visible lines of Li III ($n = 5 \rightarrow n = 4$) is observed, and high resolution spectral profile data are given in Ref. [111]. Examples of the observed profiles are shown in Figs. 7.1 and 7.2 (squares and other symbols). These profiles are obtained during neutral beam injection (NBI) and after the turn off of NBI, respectively. It is seen that the observed spectral profiles strongly depend on whether NBI is present or not; the location where the lines are emitted. The line width and the peak wavelength change significantly for different conditions. Besides the difference in ion temperatures, these differences should reflect differences in the population mechanisms of the upper level of this line. The objective of the present study is to establish the theoretical basis for interpretation of the spectral data obtained in such experiments.

It would be natural to expect that, during NBI, the Li^{2+} ions are populated mainly by charge exchange reaction with the neutral H atoms in the heating beam:

$$Li^{3+} + H^0 \rightarrow Li^{2+}(nl) + H^+. \tag{7-1}$$

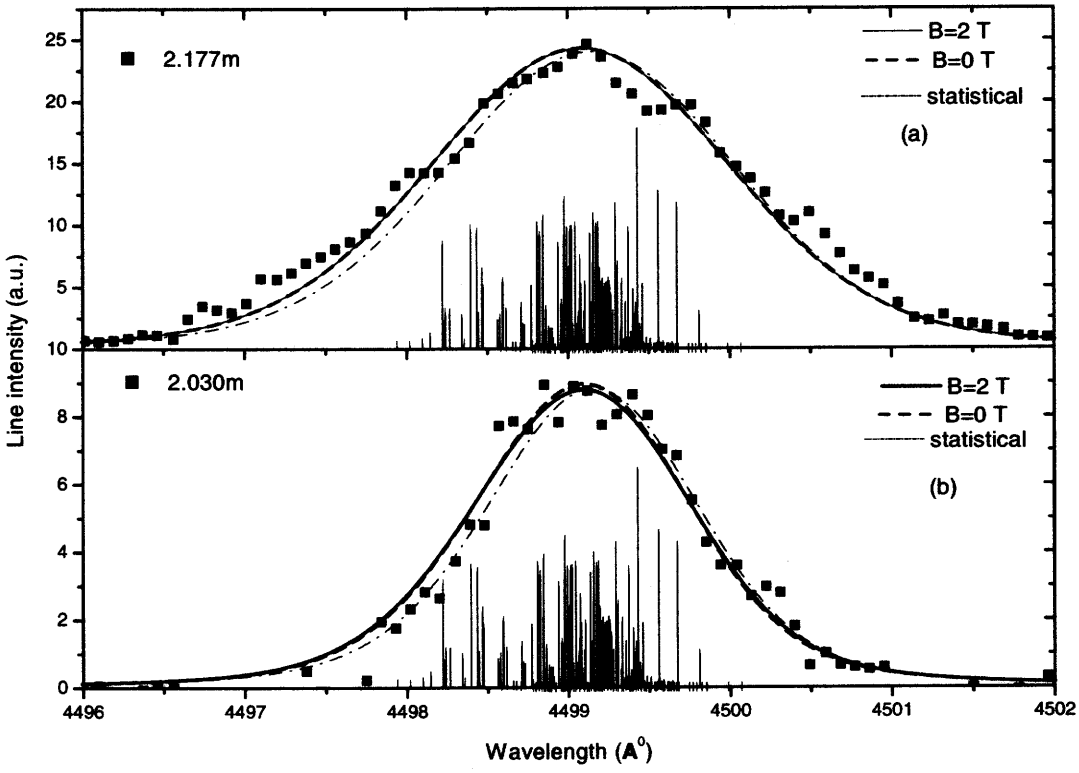

Figure 7.1 Comparison with theoretical (solid line) and experimental (squares) spectral profiles during neutral beam injection. Experimental data were taken by Kondo *et al.* [111]. The line positions and intensities for the charge exchange component are shown with the vertical lines. The line profiles assuming only statistical weight l-distribution are shown by the dash-dotted lines. The dashed line is the best fit with the neglect of the Zeeman effect. The numbers in the figure are the positions where the spectra are measured, i. e., center (a) and edge (b). Ion temperatures are $T_i = 200 \pm 14$ eV in the center and $T_i = 80 \pm 9$ eV in the edge by theoretical calculations with 2T magnetic field (solid lines).

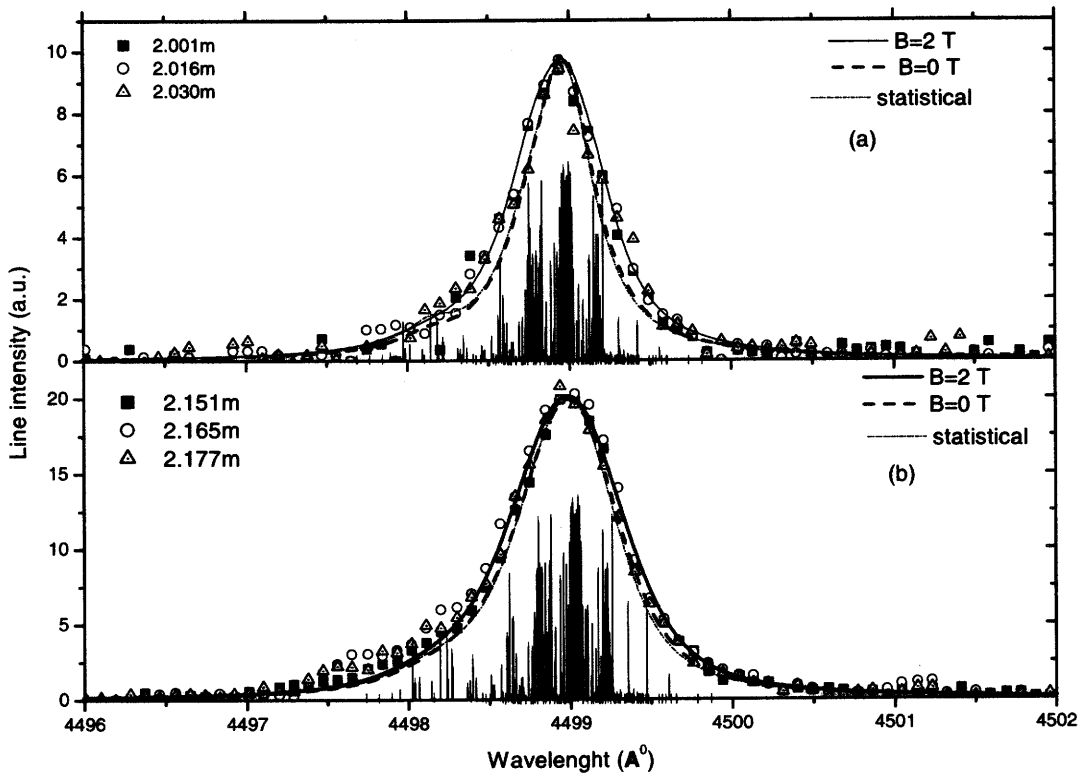

Figure 7.2 Comparison with theoretical (solid line) and experimental (symbols) spectral profiles after neutral beam injection. The line positions and intensities for the recombination component are shown with the vertical lines. The line profiles assuming the statistical weight l-distribution are shown by the dash-dotted lines with the neglect of the Zeeman effect. The numbers in the figure are the positions where the spectra are measured, i. e., center (a) and edge (b). Ion temperatures are $T_i = 8 \pm 2$ eV in the center and $T_i = 5 \pm 1$ eV in the edge are derived with 2T magnetic field by theoretical fit (solid lines).

When the neutral beam is turned off, the plasma temperature drops rapidly, radiative recombination is expected to be the dominant populating mechanism:

$$\mathrm{Li}^{3+} + \mathrm{e}^- \rightarrow \mathrm{Li}^{2+}(nl) + h\nu. \tag{7-2}$$

Whether NBI is present or not, electron collisional excitation/deexcitation is always an important populating mechanism:

$$\mathrm{Li}^{2+}(n'l') + \mathrm{e}^- \rightarrow \mathrm{Li}^{2+}(nl) + \mathrm{e}^-. \tag{7-3}$$

For a correct interpretation of the observed profiles like those in Figs. 7.1 and 7.2, besides the ion temperature and the populating mechanism, we also have to take account of: (i)the presence of fine structure which is large enough to affect the profile of the line between these highly excited states, (ii) the Zeeman effect and motional Stark line splitting which arise from the strong magnetic field in the plasma, (iii) the background line emission produced by electron collisional excitation, Eq. (7-3), of the ground-state Li^{2+} ions in the plasma periphery, and (iv) the presence of secondary low-energy H atoms in the vicinity of neutral beam in the plasma. From these considerations, we decided 1) to conduct an accurate Zeeman effect calculation and 2) to construct a collisional-radiative (CR) model in which these three (charge exchange recombination, radiative recombination and electron collisional excitation) population mechanisms are taken into account.

8.0 Line Splitting and Broadening in Magnetic Field

Let us now consider the effect of an external magnetic field on single-electron atoms. In this chapter, we shall restrict ourselves to the special case of a low Z ion (i.e. $Li^{2+}(nl)$) in a time-independent homogeneous magnetic field $\vec{B}$ [1]. Thus the state of an electron can be described by the Pauli approximation, and the Hamiltonian reads

$$H = H_0 + \Sigma + W \tag{8-1}$$

where H_0 is the non-relativistic Hamiltonian, Σ is the spin-orbit interaction energy, and W is the interaction energy with the magnetic field $\vec{B}$. We put $\vec{S}$ for the spin operator, $\vec{L}$ for the orbital angular momentum, in atomic units, and take our z-axis along the magnetic field. We then have the explicit form of Σ and W as,

$$\Sigma = \frac{1}{2}\alpha^2 Z\overline{r^{-3}}\vec{L}\cdot\vec{S}, \tag{8-2}$$

$$W = \mu_0\vec{B}\cdot\left(\vec{L} + g_s\vec{S}\right), \tag{8-3}$$

where α and μ_0 are the fine structure constant and the Bohr magneton, respectively. The Lande factor g_s is exactly 2 in the Dirac theory. We consider the operator $(\Sigma + W)$ as a perturbation to the nonrelativistic Hamiltonian (H_0) and find the perturbed eigenfunctions and eigenvalues [2]. This procedure will be discussed below.

Besides $\vec{L}^2$, $J_z = (\vec{L} + \vec{S})_z$ is exactly constant of motion. Thus the eigenstates of $(H_0 + \Sigma + W)$ are labeled with the quantum numbers n, l and m (eigenvalue of J_z). The general wave function with these quantum numbers can be written as a superposition of two linearly independent spin wave functions. We take for these two independent states the two eigenstates of the field-free Hamiltonian $(H_0 + \Sigma)$. We denote these two eigenstates and their eiegnvalues by u_+, u_- and E_+, E_-, respectively. They are the eigenstates of the total angular momentum operator $\vec{J}^2$ $(\vec{J} = \vec{L} + \vec{S})$ with inner quantum number $j = l + \frac{1}{2}$ and $j = l - \frac{1}{2}$, respectively. We further define

[1] If $\vec{B}$ is uniform over distances of the order of several atomic radii 0.52917×10^{-8} cm, and over time of the order of many atomic time unit 2.4189×10^{-17} sec., the results are almost the same as for an exactly uniform $\vec{B}$.

[2] The interaction energy with magnetic field is rather weak in general, say 3 T, and one obtains Zeeman splitting of the order of 3 wave-numbers $\approx$ 1Å for visible light. Then the perturbation method could describe the system to high accuracy.

a dimensionless parameter ξ by

$$\xi = \frac{B\mu_0}{\Delta E}, \tag{8-4}$$

where

$$\Delta E = E_+ - E_-. \tag{8-5}$$

The explicit matrix representation of the operator W in terms of u_+ and u_- can be written in the form

$$E = \frac{1}{2}(E_+ + E_-) + E', \qquad u = au_+ + bu_- \tag{8-6}$$

E', a and b are given by the eigenvalue equation (with g_s=2)

$$\begin{pmatrix} \frac{1}{2} + \xi\frac{2m(l+1)}{2l+1} & \xi\frac{\sqrt{(l+\frac{1}{2})^2-m^2}}{2l+1} \\ \xi\frac{\sqrt{(l+\frac{1}{2})^2-m^2}}{2l+1} & -\frac{1}{2} + \xi\frac{2ml}{2l+1} \end{pmatrix} \begin{pmatrix} a \\ b \end{pmatrix} = \frac{E'}{\Delta E} \begin{pmatrix} a \\ b \end{pmatrix} \tag{8-7}$$

The two possible eigenvalues E' are obtained by solving the determinant equation as,

$$E' = \Delta E \left[\xi m \pm \frac{1}{2}\sqrt{1 + \xi\frac{4m}{2l+1} + \xi^2} \right] \tag{8-8}$$

The normalized eigenfunctions corresponding to these two eigenvalues are then given by

$$\begin{aligned} a &= \sqrt{\tfrac{1}{2}(1+\gamma)}, \quad b = \sqrt{\tfrac{1}{2}(1-\gamma)} \quad \text{for the higher level,} \\ a &= -\sqrt{\tfrac{1}{2}(1-\gamma)}, \quad b = \sqrt{\tfrac{1}{2}(1+\gamma)} \quad \text{for the lower level,} \end{aligned} \tag{8-9}$$

where

$$\gamma = \frac{1 + \xi\frac{2m}{2l+1}}{\sqrt{1 + \xi\frac{4m}{2l+1} + \xi^2}}$$

.

Once the eigenfunctions and eigenvalues of the total Hamiltonian $(H_0 + \Sigma + W)$ are known, the radiative transition probabilities between these Zeeman levels are calculated. The line distribution of Li^{2+} $n = 5 \rightarrow n = 4$ transition are plotted in Figs. 1 and 2, where the upper levels are populated by the charge exchange recombination and radiative recombination, respectively.

9.0 Collisional-Radiative Model

In this chapter, we explain the kinetic equations and summarize the atomic data.

9.1 Kinetic equations

Let us consider minor impurity species, lithium in the present case, in a plasma which is composed of protons and electrons as major constituents. This plasma is in a magnetic field and heated by NBI. The population density of $Li^{2+}(i)$ is determined by collisions with electrons and protons, by spontaneous radiative decay and by the interaction with hydrogen atoms in the beam. The rate equation for the population density of the $Li^{2+}(i)$ state is given by

$$\begin{aligned}\frac{dn(i)}{dt} &= \{\sum_{j\neq i} n_e C_{ji} n(j) + \sum_{j>i} A_{ji} n(j)\} - \{\sum_{j\neq i} n_e C_{ij} n(i) + \sum_{j<i} A_{ij} n(i)\} \\ &\quad + \{n_e \alpha_i n_+ + n_{\mathrm{H}} \beta_i n_+\} - \{n_e S_i n(i)\}, \end{aligned} \tag{9-1}$$

where n_e, n_+ and n_{H} are the densities of electron, fully ionized Li^{3+} ions, and neutral hydrogen in the heating beam, respectively. C_{ji} is the collisional excitation/deexcitation rate coefficient and A_{ji} is the radiative transition probability from state j to i. S_i is the rate coefficient for electron impact ionization from the i state. α_i is the rate coefficient for recombination, $Li^{3+} + e^- \rightarrow Li^{2+}$, both by radiative and three-body recombination. β_i is the rate coefficient for charge exchange recombination of eq.(7-1). Proton collisions are included in the model for angular momentum changing transtions within the same n. The proton temperature is assumed equal to the electron temperature. In the text, i (or j) is the index of Li^{2+} levels, and $i = 1$ is used to label the ground state $Li^{2+}(1s)$.

According to the quasi-steady-state assumption [117–123], the densities of electrons, Li^{3+}, $Li^{2+}(1s)$ and H atoms are uncoupled. Thus the population density of Li^{2+} in an excited state i may be expressed as a sum of the three components,

$$n(i) = n_e E_i n(1) + n_e R_i n_+ + n_{\mathrm{H}} G_i n_+ \qquad i \geq 2, \tag{9-2}$$

where E_i, R_i and G_i may be called the effective population coefficients. The first term represents the contribution from the population flux originating from the ground

state ions by electron collisional excitation, the second term the flux originating from radiative recombination and three-body recombination of the fully ionized ions, and the last term the flux coming from charge exchange recombination. Substituting eq. (9-2) to eq. (9-1), the following three sets of equations for E_i,R_i, and G_i are obtained,

$$E_i = \frac{C_{1i} + \sum'_{j\neq i} n_e C_{ji} E_j + \sum_{j>i} A_{ji} E_j}{n_e S_i + \sum_{i\neq j} n_e C_{ij} + \sum_{i>j} A_{ij}}, \tag{9-3}$$

$$R_i = \frac{\alpha_i + \sum'_{j\neq i} n_e C_{ji} R_j + \sum_{j>i} A_{ji} R_j}{n_e S_i + \sum_{i\neq j} n_e C_{ij} + \sum_{i>j} A_{ij}}, \tag{9-4}$$

$$G_i = \frac{\beta_i + \sum'_{j\neq i} n_e C_{ji} G_j + \sum_{j>i} A_{ji} G_j}{n_e S_i + \sum_{i\neq j} n_e C_{ij} + \sum_{i>j} A_{ij}}, \tag{9-5}$$

where the primed sums extend only over excited states. Solving the three sets of equations with $i \geq 2$, we obtain the nl-resolved population densities of excited states.

Putting Eqs. (9-3) and (9-2) into the collisional-radiative model (9-1), then the rate equations for the ground state can be rewritten in terms of E_i, R_i and G_i, viz.

$$\frac{dn(1)}{dt} = -n_e S_{eff} n(1) + n_e \alpha_{eff} n_+ + n_h \beta_{eff} n_+ \tag{9-6}$$

$$= -n_e S_{cr} n(1) + n_e \alpha_{cr} n_+ \tag{9-7}$$

with

$$S_{eff} = S_1 + \sum_{j=2} C_{1j} - \sum_{j=2} [E_j (n_e C_{j1} + A_{j1})] \tag{9-8}$$

$$\alpha_{eff} = \alpha_1 + \sum_{j=2} [R_j (n_e C_{j1} + A_{j1})] \tag{9-9}$$

$$\beta_{eff} = \beta_1 + \sum_{j=2} [G_j (n_e C_{j1} + A_{j1})] \tag{9-10}$$

and

$$S_{cr} = S_{eff} \tag{9-11}$$

$$\alpha_{cr} = \alpha_{eff} + \frac{n_h}{n_e} \beta_{eff}. \tag{9-12}$$

Here, S_{cr} and α_{cr} are called collisional-radiative ionization and recombination rate coefficients, respectively, and represent the effective rate coefficients for ionization and recombination of the plasma. When $n_e S_{cr} n(1) = n_e \alpha_{cr} n_+$, ionization and recombination are balanced.

9.2 Atomic data

The accurate atomic data are essentially important to analyze the spectra. In our CR model in eq. (9-1) we included the nl resolved states up to $n = 20$. Thus a complete set of atomic data up to $n = 20$ are necessary for this CR calculation. However, accurate atomic data are not easy to obtain even for an H-like system. In this work, the electron-impact excitation ($n_i l_i \rightarrow n_f l_f$) data are calculated by the Coulomb-Born-Exchange (CBE) approximation for $1s \leq n_i l_i$,$n_f l_f \leq 5g$, by n^{-3} scaling law for $1s \leq n_i l_i \leq 4f$ and $6s \leq n_f l_f$, and by Mewe's semi-empirical formula [124] for transitions between high-lying states with $6s \leq nl$. The CBE calculation is carried out with the use of the ATOM code [125] and compared with the results by other methods of distorted wave (DW) [126, 127] and the R-matrix with pseudo-state (RMPS) [128]. Figure 9.1 shows examples of comparisons of the scaled collision strengths $Z^2\Omega$ for the 1s-2s and 1s-5s transitions, where Z is a charge of H-like ions and Ω is a collision strength. The calculations by CBE and DW are in good agreement with each other, say within 10% from threshold to high energy limit. However the results by RMPS for $1s - ns$ transitions are quite different from our results in low energy region; the discrepancy can be as large as by a factor of 2 near the threshold. The more detailed comparison is given in Ref. [129, 130].

The $l - mixing$ collisions by electrons and ions are important to determine the spectral profiles, and the corresponding rate coefficients are estimated by the Jacobs' formula [131]. The ionization rate coefficients from the ground state and all the excited states are estimated by Lotz's empirical formula [132]. The collisional de-excitation and three-body recombination rate coefficients are derived from the detailed balance relation using the excitation and ionization rate coefficients. The spontaneous radiative processes for all the allowed transitions and one forbidden transition, $2s(^2S) - 1s(^2S)$, are included. Radiative recombination rate coefficients are obtained from the detailed balance principle from the photo-ionization cross sections [133].

The direct charge exchange recombination rate coefficient to a state i is given as

$$\beta_i = v\sigma_i,$$

where v is the particle velocity of the beam and σ_i is the state-selective charge exchange cross section. Data for the state-selective cross sections are taken from the

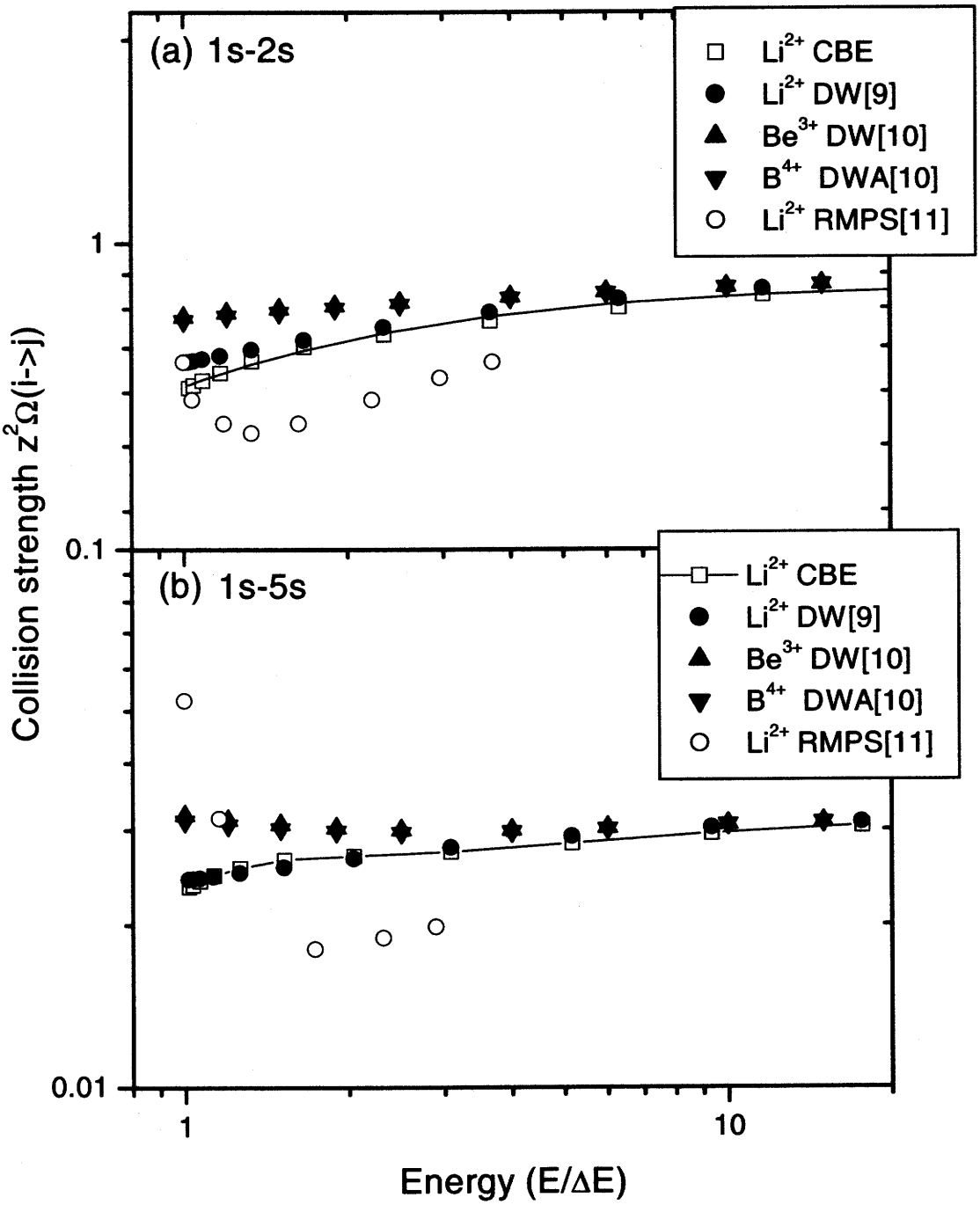

Figure 9.1 Scaled Electron-impact excitation collision strength $Z^2\Omega$ for the (a) $1s-2s$ and (b) $1s-5s$ transitions in hydrogen-like ions. The open squares with line denote the results by the ATOM code [125]; the solid circles, Hullac code [126]; the upward and downward triangles, Clark *et al.* (1996)[127]; the open circles, Badnell *et al.* (1997)[128]

recent literatures [134] up to $n = 5$. For extending the data to highly excited states, we assume an n^{-3} dependence with n higher than 5.

10.0 Spectra of Li^{2+} Ions in Magnetic Field

In this chapter, we show the calculated line intensities and compare to the experiment.

10.1 Calculated line intensities

In our calculation the line intensity can be separated into three components, as

$$I_{ji} = E_i A_{ji} n_e n(1) + R_i A_{ji} n_e n_+ + G_i A_{ji} n_{\mathrm{H}} n_+, \tag{10-1}$$

where the three terms represent the effective contributions from the ground state $n(1)$, the ion n_+ through recombination, and the ion n_+ through charge exchange, respectively. Then the spectra can be determined for arbitrary beam particle flux densities n_{H} and arbitrary ion abundance $n(1)$ and n_+. Since we solved CR model with resolved nl sublevels, we can estimate the line intensities between $nl - n'l'$ transitions by different three population mechanisms. The temperature dependence of the three population coefficients (E_i, R_i and G_i divided by statistical weights) for $5l$-state are shown in Figs. 10.1(a), (b) and (c).

Figure 10.2 shows line intensity ratios for Li^{2+} ions $\Delta n = 1$ transitions ($\sum_{ll'} nl - (n-1)l'$) to the resonance line ($2p - 1s$) at $T_e = 500$ eV and $n_e = 10^{13}$ cm^{-3}, where excitation, recombination, and charge exchange components have been plotted separately. We take the density and the kinetic energy of H atoms to be $n_h = 10^{-5} n_e$ and $E_h = 25$ keV/amu. The intensity ratios including these three components are also shown as the sum. In this figure, line intensities are normalized by Lyman α emission. From Fig. 10.2, one can see that the ratios $I(\Delta n = 1)/I(2p - 1s)$ of the excitation component decrease sharply with principal quantum number n. Although the excitation from the ground state populates np states more than other states, the line intensities for $\Delta n = 1$ are mainly emitted from the states with larger angular momentum. For example, the intensity for $n = 5 - 4$ is dominated by the $5f - 4d$ and/or $5g - 4f$ transitions. The ratio of charge exchange components decreases more slowly with n than that of the excitation components; that is because the nl distribution of charge exchange cross section over principal quantum number n and angular quantum number l for the beam energy $E_h = 25$ keV/amu are broader than

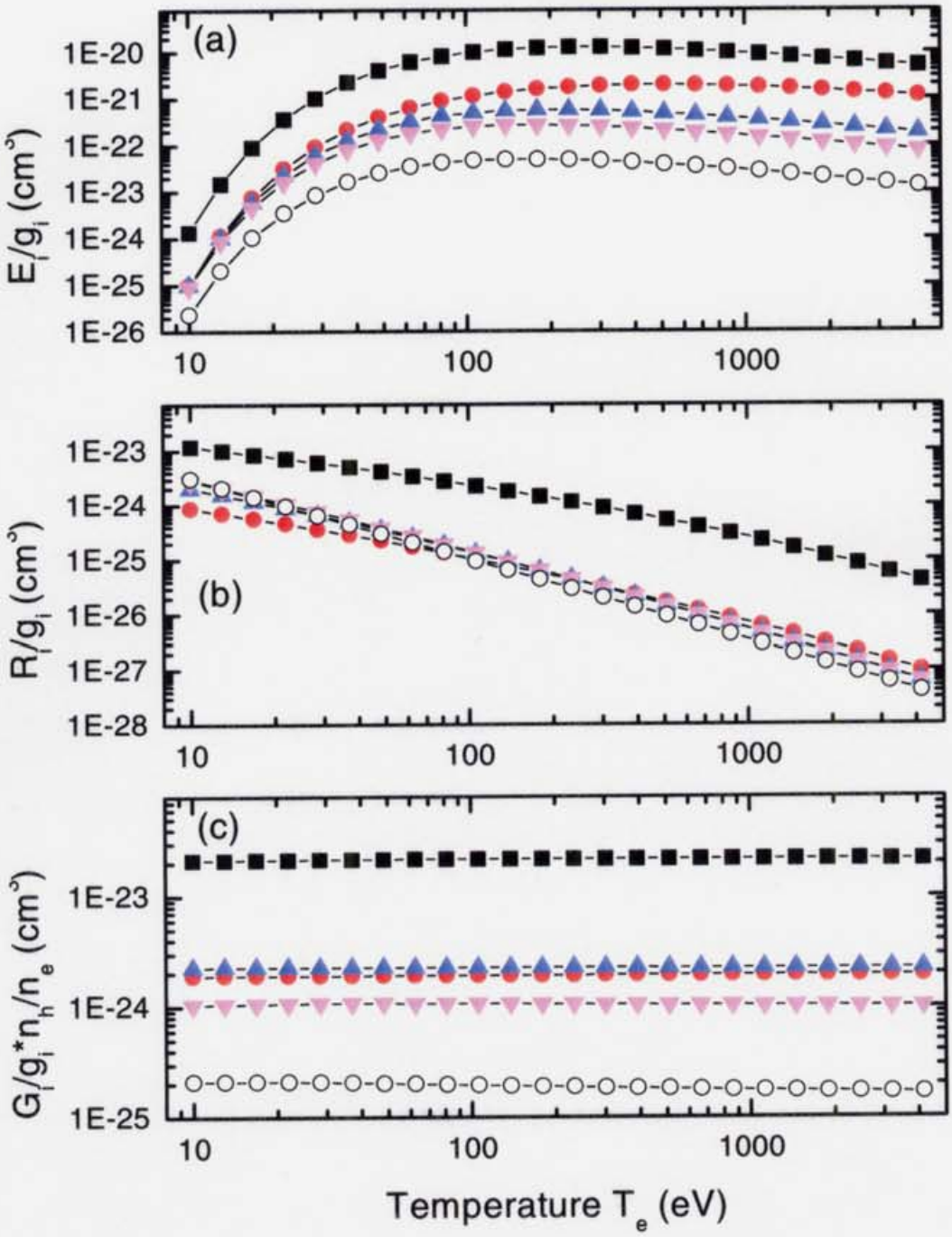

Figure 10.1 The temperature dependence of population coefficients (E_i, R_i, G_i) divided by statistical weights for $5l$ at $E_h = 25$ keV/amu and $n_h = 10^{-5}n_e$. The solid quadrangles are for $5s$; the circles, $5p$; the upward triangles, $5d$; the downward triangles, $5f$; the open circles, $5g$. E_i/g_i, R_i/g_i and G_i/g_i are shown in (a), (b) and (c) respectively.

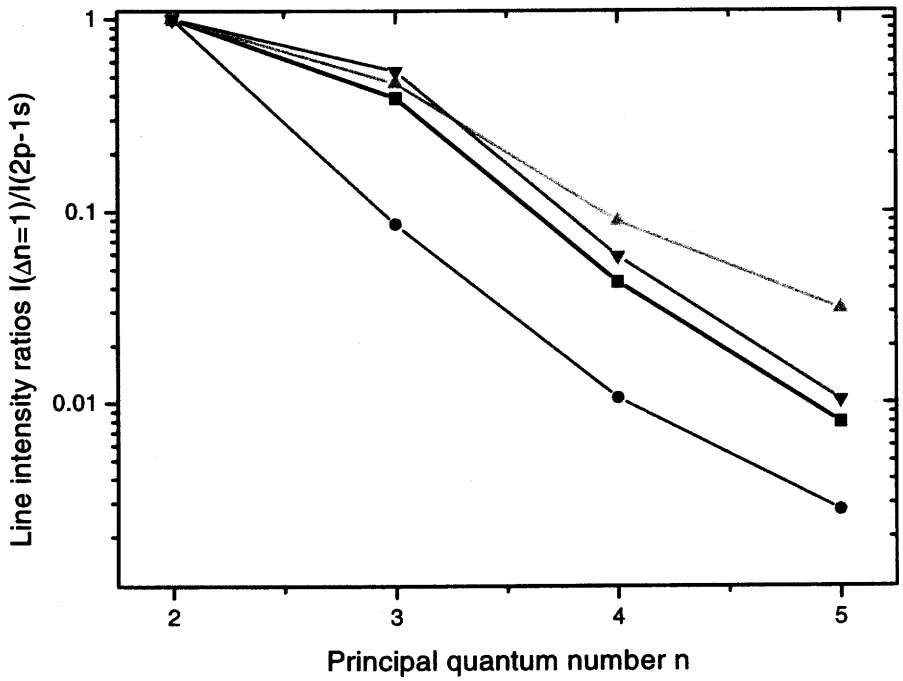

Figure 10.2 Line intensity ratios of Li III ions from $\Delta n = 1$ transitions and normalized on Lyman α vs principal quantum number of upper levels. The upper levels are populated by excitation (circle), recombination (upperward triangle) and charge exchange (downward triangle). The sum of these three components are for ionization equilibrium (square).

that of excitation from the ground state. From Fig. 10.2, we can see the line intensity ratios $I(\Delta n = 1)/I(2p - 1s)$ including three components in ionization equilibrium with $n_h/n_e = 10^{-5}$ are almost the same as the charge exchange component. Charge exchange is the main mechanism for producing excited H-like Li ions in the NBI.

The Li III emission lines from $n = 5$ to $n = 4$ transitions are in the visible range ($\sim$ 4499 Å) and they are often measured with high resolution spectroscopy. In order to estimate the spectral line profiles of ions in magnetic confined plasmas, we need to know the population densities of the resolved magnetic sublevels. After calculating the population densities of nl states by our CR model, we assume population densities are equal over the magnetic quantum number m. Thus the population density of Li^{2+}

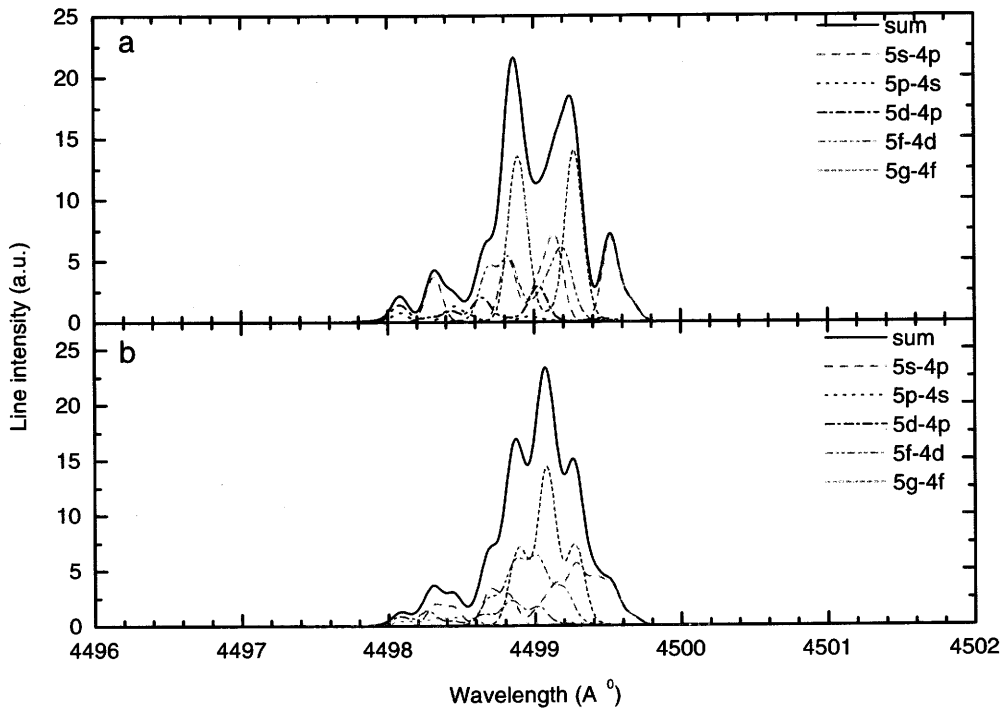

Figure 10.3 Spectral line profiles produced by excitation in magnetic field B=2 T, where the ion and electron temperatures are 1 eV and 500 eV, respectively. In the figures, (a) and (b) are spectral profiles observed in parallel and perpendicular directions to magnetic field, respectively.

in an excited magnetic sublevels (nlm) can be computed. In this section, we take magnetic field strength $B = 2$ T, and the quantization axis along the magnetic field.

Figures. 10.3, 10.4 and 10.5 show the spectral profiles, where the upper levels are populated by excitation from the ground state, by electron-ion recombination and by charge exchange with the H atoms in the beam, respectively. In these Figures, panels (a) and (b) show Zeeman splitting spectra observed in the perpendicular and the parallel direction to the quantization axis, respectively. We plotted spectral profiles by $5s-4p$, $5p-4s$, $5d-4p$, $5f-4d$ and $5g-4f$ transitions separately and the sum of them as indicated in Figures. The various Zeeman components are convoluted with

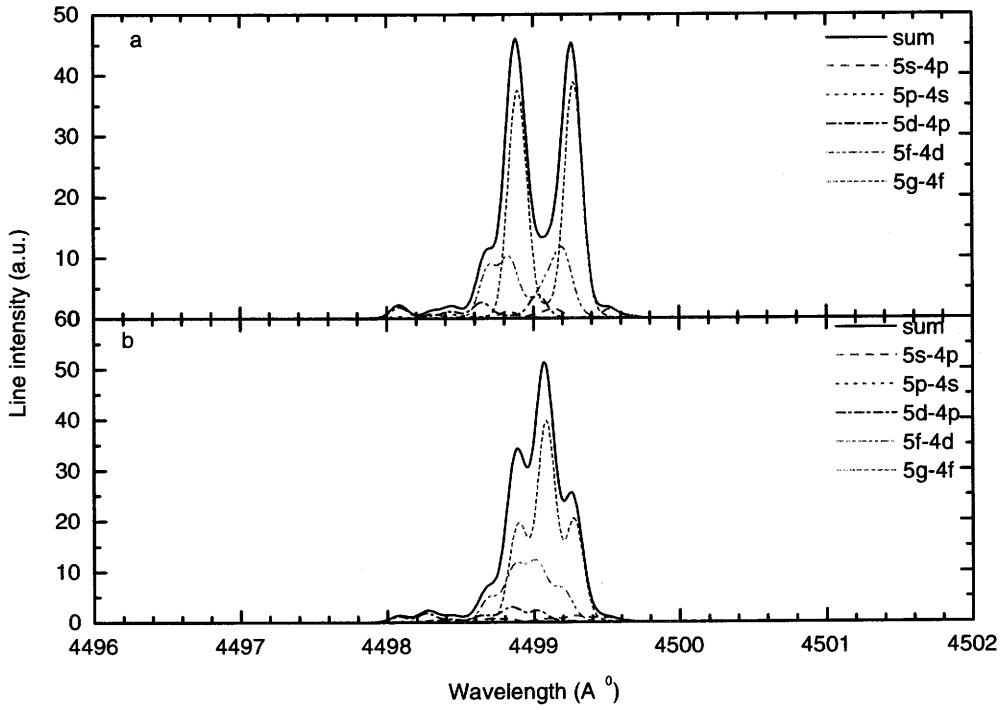

Figure 10.4 Spectral line profiles produced by radiative recombination in magnetic field B=2 T, where the ion and electron temperatures are 1 eV and 10 eV, respectively. In the figures, (a) and (b) are spectral profiles observed in parallel and perpendicular directions to magnetic field, respectively.

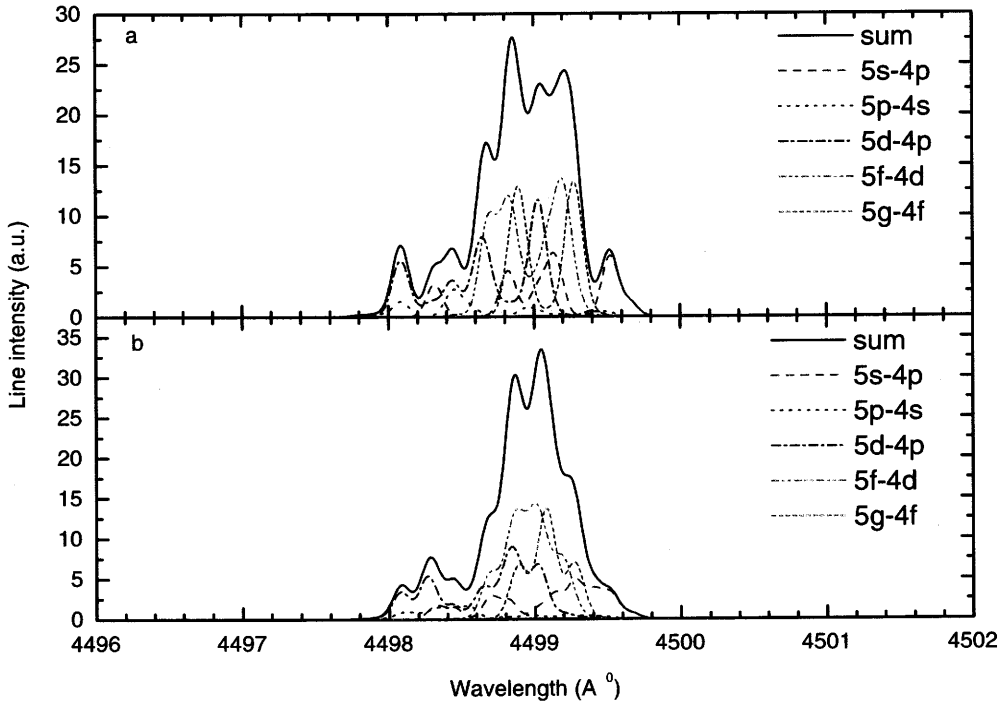

Figure 10.5 Spectral line profiles produced by charge exchange in magnetic field B=2 T, where the ion and electron temperatures are 1 eV and 500 eV, respectively. The kinetic energy of H atoms in beam is 25 keV/amu. In the figures, (a) and (b) are spectral profiles observed in parallel and perpendicular directions to magnetic field, respectively.

a Gaussian profile,

$$P(\lambda) = \frac{1}{\sqrt{\pi}\lambda_D} \exp(-\frac{(\lambda - \lambda_0)^2}{\lambda_D^2}), \tag{10-2}$$

where λ_0 is the photon wavelength and λ_D is the Doppler width,

$$\lambda_D = 4.634 \times 10^{-5} \lambda_0 \sqrt{T_i/A_i}, \tag{10-3}$$

where T_i is the ion temperature measured in eV, and A_i is the atomic mass number. A very low ion temperature $T_i = 1$ eV, corresponding Doppler width 0.079Å, is used in order to show the Zeeman effect on line shapes. Excitation spectra are mainly contributed by $5s - 4p$, $5f - 4d$ and $5g - 4f$ transitions. Most of the recombining lines come from $5g - 4f$ transition and also from $5f - 4d$. Charge exchange spectra are contributed by $5s - 4p$, $5d - 4p$, $5f - 4d$ and $5g - 4f$ transitions which are peaked at 4498.85Å and 4499.15Å for observing in the perpendicular direction, and peaked at 4498.75Å and 4499.25Å for measuring in the parallel direction. In excitation and charge exchange spectra, there is a weak peak at 4498.3Å which originates from a $5d_{3/2} - 4p_{1/2}$ transition. In recombination spectra, the peak $(5d_{3/2} - 4p_{1/2})$ is absent. The rather broader distribution of charge exchange spectra is due to the broader distribution of charge exchange cross sections over the angular momentum quantum number l. The spectra observed in the parallel direction to the magnetic field is broader than that observed in the perpendicular direction. This is because one can see only the σ components along the quantization axis. In many cases, l-distributions according to the statistical weights are assumed [111]. In this chapter we have taken into account the realistic l-distributions for different atomic processes (excitation, recombination and charge exchange) and found that the line profiles are much different from those following the statistical weights. The wavelength at the peak is also different from that by statistical weights. More detailed comparisons are shown in Ref. [129].

10.2 Comparison with the experiment

The comparison of our calculation with experimental measurements are shown in Figs. 7.1 and 7.2, where the experimental data are those measured from the Heliotron E plasma [111]. In these figures, the various Zeeman components are convoluted with

a Voigt profile,

$$P(X,Y)d\lambda = \frac{Y}{\pi\sqrt{\pi}\lambda_D}\int_0^\infty \frac{\exp(-T^2)}{(X-T)^2+Y^2}dTd\lambda, \tag{10-4}$$

where

$$\begin{aligned} Y &= (\Gamma/2)/\lambda_D, \\ X &= (\lambda-\lambda_0)/\lambda_D, \\ T &= (\lambda'-\lambda_0)/\lambda_D, \end{aligned}$$

where Γ is the Lorentzian factor which is dominated by the instrumental width in the experiment. Because the experimental system is designed for measuring spectra emitted by high temperature ions, the instrumental width slightly varies with pixels. At the moment, we take Γ equal to the average instrumental width 0.4 Å. It is also hard to decide the direction of the sight line with respect to the magnetic field, since the experiment was carried out on a helical type system. For simplicity, we assume the sight line is perpendicular to the magnetic field.

The spectra measured during the NBI are shown in Fig. 7.1 by squares. The ion temperature are obtained from fitting the calculated spectra profiles with the experimental measurements. The best fitted curves are shown by the solid lines in Fig. 7.1. We obtained the ion temperature (T_i) to be 200 ± 14 eV in the center plasma (Fig.7.1(a)), and 80 ± 9 eV in the edge plasma (Fig.7.1(b)). The measured electron temperature is above 400 eV in the center and 200 ± 10 eV in the edge [111]. The derived ion temperatures are lower than the electron temperatures during the NBI. The Doppler broadening due to ion temperature is too broad to separate the Zeeman splitting.

After the neutral heating beam is turned off, the plasma temperature drops rapidly and radiative recombination becomes a dominant atomic process for producing H-like Li ions. In this case, the ion temperature should be low, and these recombining spectra are considered to be good for investigating Zeeman effect on line shapes. In Fig. 7.2, we plot the spectra of H-like Li ions, which are emitted from the center and the edge plasma, respectively. The asymmetric experimental line shapes are clearly seen; this is due to the atomic fine structures, which are dependent on the population density distribution over the angular momentum quantum number l. The asymmetry is dependent on the electron temperature which determines the l-distribution of

the radiative recombination rate coefficients as shown in Fig.10.1(b). Now, we have two free parameters: electron temperature which accounts for the asymmetry of line shapes, and ion temperature which accounts for the line width. We optimize the two parameters to get the best agreement with the experimental results. Then we obtain that the electron and ion temperatures are $T_e = 30 \pm 5$ eV and $T_i = 8 \pm 2$ eV in the center plasma, and $T_e = 10 \pm 2$ eV and $T_i = 5 \pm 1$ eV in the edge plasma. In the figure, we also plot the spectra with the Zeeman effect ignored by the dashed line. In this case, we need $T_i = 15$ eV in the center and $T_i = 10$ eV in the edge to fit the experimental measurements. Thus we get the higher ion temperature by about a factor 2 if we do not take into account the Zeeman effect. The ion temperature derived by us is also lower than the electron temperature in this recombining phase.

Let us note at this point that the wavelength at the peak of the charge exchange spectra and of excitation spectra are shifted in the shorter wavelength than that of the recombing spectra by 0.1Å and 0.2Å , respectively. Line widths of the charge exchange spectra and of the excitation spectra are wider than that of the recombination spectra. This wavelength shift and spectral broadening are considered due to the difference of the l-distributions of charge exchange, excitation and recombination processes as shown in Fig. 10.1.

The spectral fitting with the assumption of the statistical weight l-distribution population densities is widely practiced to obtain ion temperatures from measurements such as in Ref. [111]. The line profile assuming the statistical weight l-distribution and without the Zeeman splitting are also shown in Fig. 7.1 and 7.2 by dash-dotted lines. Since the l-distributions of radiative recombination are fairly close to those of statistical weights, the radiative recombination spectra are in good agreement with the profiles obtained from the statistical weight distribution assumption. The charge exchange recombination spectra, however, are significantly different from the statistical weight spectra, i.e. they are broader than the latter and locate at the shorter wavelength side. These results show that we have to take into account the population mechanism and the Zeeman effect properly to obtain the correct ion temperatures from the spectral profiles.

In the above discussions, the direct excitation have been neglected for the plasma after the trun-off of NBI. From Fig. 10.1, we could see that the effective population coefficients of radiative recombination and excitation are of the same order of mag-

nitude for electron temperature at tens of eV. Thus, if an emission originating from excitation is comparable with radiative recombination, one must have the density ratio of H-like $Li^{2+}(1s)$ ions to fully ionized Li^{3+} ions to be nearly equal to unity. The plasma, however, should be recombining from a high temperature plasma, in which the density of Li^{3+} ions is much higher than that of $Li^{2+}(1s)$ ions. Even in the ionization balance, the abundance Li^{3+} ions is still almost one order of magnitude higher than of H-like $Li^{2+}(1s)$ ions at electron temperature $T_e = 20$ eV [129]. So the contribution from the direct excitation can be neglected safely.

We estimate here the motional Stark effect arising from the interaction with the confined magnetic field. Although Li^{2+} ions as impurities in plasma do not move directionally, we assume they are moving perpendicular to the magnetic field with the thermal velocity. The maximum of the Stark splitting for Li^{2+} ions with ion temperature of one hundred eV is 0.894 cm^{-1} of the outer components, $n1 = 4$, $n2 = 0$ and $n1 = 0$, $n2 = 4$, ($n1$ and $n2$ are the quantum numbers in a parabolic coordinate) for $n = 5$ in a magnetic filed $B = 2$ T. The minimum of Zeeman splitting is 0.934 cm^{-1}, which is still stronger than the motional Stark effects. Thus we may say that the motional Stark effects are not important in our case.

One more important fact is to be noted here: in our fitting procedure, we had to shift whole the calculated spectrum toward the shorter wavelength by 0.15 Å with respect to the measured one. Since the shift does not depend either on the location or on weather the neutral heating beam is turned on or off. We do not have any explanation and suggest an error in the wavelength calibration of the spectrometer.

11.0 Conclusion

We have presented the detail calculation of line profiles of H-like Li ions in a magnetic confined plasma. In our calculation, the population densities of nl resolved states of H-like Li ions are separated into three components, depending on excitation from the ground state, electron-ion recombination and charge exchange with neutral hydrogen. The energy levels and transition probabilities of the H-like system are calculated by diagonalizing the Hamiltonian with the magnetic interaction included.

Our calculations provide a fairly good description of the measured spectra [111], and we obtained the ion temperatures from the spectral profiles measured during NBI and after NBI turned off. Ion temperature derived by ignoring the Zeeman effect is two times higher than that obtained by including the Zeeman broadening. The present method is readily extended to He-like or Li-like ions.

APPENDIX A

APPENDIX A One-electron Diatomic-Molecular Orbital

The Hamiltonian of one electron moving in the field of two fixed charges Z_A and Z_B is given by Eq.(3-5), that is

$$h_{el} = -\frac{1}{2m}\nabla_r^2 - \frac{Z_A}{r_A} + \frac{Z_B}{r_B}. \tag{A-1}$$

In the prolate spheroidal coordinates this equation is separable, and we obtain:

$$\left[\frac{d^2}{d\phi^2} - \mu^2\right]\Omega(\phi) = 0 \tag{A-2}$$

$$\left[\frac{d}{d\xi}(\xi^2-1)\frac{d}{d\xi} - \frac{\mu^2}{\xi^2-1} + RZ_+\xi - c^2(\xi^2-1) + A\right]X(\xi,R) = 0 \tag{A-3}$$

$$\left[\frac{d}{d\eta}(1-\eta^2)\frac{d}{d\eta} - \frac{\mu^2}{1-\eta^2} + RZ_-\eta - c^2(1-\eta^2) - A\right]Y(\eta,R) = 0, \tag{A-4}$$

where c is the energy parameter, i.e. $\epsilon = -2c^2/R^2$ (discrete state) or $\epsilon = 2c^2/R^2$ (continuum state), Z_+ and Z_- are charge parameters given by $Z_+ = Z_B + Z_A$ and $Z_- = Z_B - Z_A$. Here μ and A are the separation constants. Solution of Eq. (A-2) gives $\Omega(\phi) = \exp(i\mu\pi)/\sqrt{2\pi}$. Finally, the electronic bound- and continuum-state wave function

$$\varphi_k(\vec{r};R) = \varphi_k(\xi,\eta,\phi;R)$$

can then be factorized and written as

$$\varphi_k(\xi,\eta,\phi;R) = C_k(R)X_k(\xi,R)Y_k(\eta,R)\exp(i\mu\pi)/\sqrt{2\pi} \tag{A-5}$$

where $C_k(R)$ is the normalization constant, and functions $X_k(\xi,R)$ and $Y_k(\eta,R)$ describe the quasi-radial and quasi-angular motions of electron, respectively. The index μ labels the component of electronic angular momentum on the $\vec{R}$ axis. Several methods have been developed through the years which can treat these kinds of differential equations (A-2,-3,and -4) in which the separation constant A and energy constant c are R dependent, e.g. Refs. [97, 98, 135–139].

The bound state wave functions both $X(\xi,R)$ and $Y(\eta,R)$ can be expanded in a suitable power series (there are several possibilities -see Refs. [97, 135, 138, 139]), obtaining recursion relations for the coefficients and solving them by matrix or infinite continued

fraction methods. In the present study, the "radial" wave function $\Lambda(\xi, R)$ is expanded in

$$X(\xi, R) = (\xi^2 - 1)^{\mu/2}(\xi + 1)^{\sigma} \exp(-c\xi) \sum_{t=0} g_t (\frac{\xi - 1}{\xi + 1})^t \tag{A-6}$$

with

$$\sigma = R/2c - \mu - 1$$

and the "angular" wave function $M(\eta, R)$ is expanded in

$$Y(\eta, R) = \exp(-c\eta) \sum_{l=\mu} d_l P_l^{\mu}(\eta). \tag{A-7}$$

Here $P_l^{\mu}(\eta)$ denotes the associated Legendre polynomials. The obtained three term recursion relations for g_t and d_l are then solved by infinite continued fraction method. Using this method it was possible to obtain the potential curves with accuracy better than 10 significant digits. To compute the electronic wave functions and couplings simply, the function $Y(\eta, R)$ is written as

$$Y(\eta, R) = \sum_{l=\mu} f_l P_l^{\mu}(\eta). \tag{A-8}$$

The same procedure can be used to calculate the separation constant and the angular wave function for the continuum states. However, the radial part must be calculated numerically. Integration starts from $\xi = 1$ with $|\Lambda(\xi = 1, R)| < +\infty$ to a sufficient larger value of $\xi_{\max}$ where $X(\xi, R)$ is accurately matching the asymptotic boundary condition,

$$X(\xi \to \infty, R) \to \frac{1}{c\xi} \sin(c\xi - \frac{RZ_+}{2c} \ln(2c\xi) - \frac{\lambda\pi}{2} + \delta_{\lambda\mu}), \tag{A-9}$$

where $\delta_{\lambda\mu}$ is the phase shift for the radial function.

I would like to note that A represents the eigenvalue of the constant of separation, which comes from the additional symmetry in two-center Coulomb system. This symmetry is described by the invariant operator $\hat{A}$ [137],

$$\hat{A} = L^2 - \frac{R^2}{4}(\Delta - \frac{\partial^2}{\partial z^2}) - R(\cos\theta_1 - \cos\theta_2) - p^2$$

, where $\vec{L}$ is the orbital angular momentum of electron. At the united-atom limit $R = 0$, $\hat{A}$ reduces to $-L^2$ and the corresponding eigenvalue is therefore $A = -\lambda(\lambda+1)$.

Finally, one sees that these one electron diatomic orbitals are labelled by two more quantum numbers λ, μ, in addition to energy. Bound states are denoted $\phi(n\lambda\mu;\vec{r};\vec{R})$, with energy eigenvalues $\epsilon(n\lambda\mu;R) < 0$, and continuum states $\phi(\epsilon\lambda\mu;\vec{r};\vec{R})$ with continuous eigenvalues $\epsilon > 0$. At each R these wave functions satisfy the orthogonality relations

$$\begin{aligned}
\langle\phi(n'\lambda'\mu';\vec{R})|\phi(n\lambda\mu;\vec{R})\rangle &= \delta_{n'n}\delta_{\lambda'\lambda}\delta_{\mu'\mu} \\
\langle\phi(\epsilon'\lambda'\mu';\vec{R})|\phi(n\lambda\mu;\vec{R})\rangle &= 0 \\
\langle\phi(\epsilon'\lambda'\mu';\vec{R})|\phi(\epsilon\lambda\mu;\vec{R})\rangle &= \delta(\epsilon'-\epsilon)\delta_{\lambda'\lambda}\delta_{\mu'\mu}.
\end{aligned} \tag{A-10}$$

The prolate spheroidal quantum numbers λ, μ are analogous to spherical polar quantum number l, m. Numerical calculations show the orthogonality relations are satisfied better than 8 significant digits for $R \leq 40$ for the wavefunctions used in this work.

APPENDIX B

APPENDIX B Separation of Angular Couplings

Here I apply the separation of angular couplings to the MO expansion, and derive the radial Schrödinger equation. This separation is made possible by transforming the coordinate system from a space-fixed coordinate system to a molecular-rotating coordinate system [32, 96].

Let $\vec{r} = (x, y, z)$ be the coordinate of electron in the space-fixed frame, while $\vec{r}' = (x', y', z')$ denotes the same vector in the rotating molecular frame. The relation between them is

$$x' = x\cos\Theta\cos\Phi + y\cos\Theta\sin\Phi - z\sin\Theta \tag{B-1}$$

$$y' = -x\sin\Phi + y\cos\Phi \tag{B-2}$$

$$z' = x\sin\Theta\cos\Phi + y\sin\Theta\sin\Phi + z\cos\Theta. \tag{B-3}$$

Here (Θ, ϕ) are the usual spherical polar angles of the vector $\vec{R}$ in the space-fixed frame. In spherical polar coordinates, the gradient $-i\vec{\nabla}^R$ (keeping $\vec{r}$ fixed) can be written

$$-i\vec{\nabla}_R = \vec{e}_R(-i\partial/\partial R)_{xyz} + \vec{e}_\Theta[R^{-1}(-i\partial/\partial\Theta)_{xyz}] + \vec{e}_\Phi[(R\sin\Theta)^{-1}(-i\partial/\partial\Phi)_{xyz}] \tag{B-4}$$

where $\vec{e}_R$, $\vec{e}_\Theta$ and $\vec{e}_\Phi$ are the unit vectors of the spherical polar system at $\vec{R}$ (they coincide with the z', x' and y', respectively). Using Eq. (B-1) the components of this operator can be rewritten

$$-i(\partial/\partial R)_{xyz} = -i(\partial/\partial R)_{x'y'z'} \tag{B-5}$$

$$-i(\partial/\partial\Theta)_{xyz} = -i(\partial/\partial\Theta)_{x'y'z'} - \hat{L}_{y'} \tag{B-6}$$

$$-i(\partial/\partial\Phi)_{xyz} = -i(\partial/\partial\Phi)_{x'y'z'} + [\sin\Theta\hat{L}_{x'} - \cos\Theta\hat{L}_{z'}], \tag{B-7}$$

where $\hat{L}_{x',y',z'}$ are the components of the electronic orbital angular momentum operator.

The $\vec{\mathbf{P}}$ is therefore expressed as [79]

$$\vec{P}_{k'k} = P^R_{k'k}\vec{e}_R + P^\Theta_{k'k}\vec{e}_\Theta + P^\Phi_{k'k}\vec{e}_\Phi, \tag{B-8}$$

where

$$\begin{aligned} P^R_{k'k} &= \langle\varphi_{k'}|(-i\partial/\partial R)|\varphi_k\rangle \\ P^\Theta_{k'k} &= -R^{-1}\langle\varphi_{k'}|\hat{L}_{y'}|\varphi_k\rangle \\ P^\Phi_{k'k} &= +R^{-1}\langle\varphi_{k'}|\hat{L}_{x'}|\varphi_k\rangle - \mu_k \end{aligned} \tag{B-9}$$

(and I have assumed that φ_k is an eigenstate of $\hat{L}_{z'}$, with eigenvalue $\mu_k\hbar$).

The corresponding form for $\vec{\mathbf{A}}$ is obtained simply by expressing the vector $\vec{s}$ in terms of its components on the x', y', z' axes:

$$\begin{aligned} A^R_{k'k} &= i(\epsilon_{k'} - \epsilon_k)\langle\varphi_{k'}|s_{z'}|\varphi_k\rangle \\ A^\Theta_{k'k} &= i(\epsilon_{k'} - \epsilon_k)\langle\varphi_{k'}|s_{x'}|\varphi_k\rangle \\ A^\Phi_{k'k} &= i(\epsilon_{k'} - \epsilon_k)\langle\varphi_{k'}|s_{y'}|\varphi_k\rangle. \end{aligned} \tag{B-10}$$

Given the components of $\vec{\mathbf{P}}$ and $\vec{\mathbf{A}}$ by Eqs. (B-9) and (B-10), we can construct explicit solutions to the close-coupled equations (3-19) for inelastic scattering in a finite manifold of molecular electronic states. Equations (3-19) can be reduced to one-dimensional (radial) equations by using a partial wave expansion.

Partial wave expansion in symmetric-top eigenfunctions takes the form:

$$F_k(\vec{R}) = R^{-1}\sum_{J=\Lambda_k}\sum_{M_J=J}^{J} G_k^{JM_J}(R)\Upsilon^{\Lambda_k}_{JM_J}(\Theta,\Phi). \tag{B-11}$$

Here it is assumed that the electronic basis state φ_k is the eigenstate of $\hat{L}_{z'}$ with eigenvalue Λ_k. The functions $\Upsilon^{\Lambda_k}_{JM_J}$ satisfy the differential equations

$$-\left[(\sin\Theta)^{-1}\frac{\partial}{\partial\Theta}\sin\Theta\frac{\partial}{\partial\Theta} + (\sin\Theta)^{-2}\left(\frac{\partial}{\partial\Phi} - i\Lambda_k\cos\Theta\right)^2 - \Lambda^2\right]\Upsilon^{\Lambda_k}_{JM_J} = J(J+1)\Upsilon^{\Lambda_k}_{JM_J} \tag{B-12}$$

and

$$-i\frac{\partial}{\partial\Phi}\Upsilon^{\Lambda_k}_{JM_J} = M_J\Upsilon^{\Lambda_k}_{JM_J}, \tag{B-13}$$

where J is the total angular momentum, and M_J its (lab frame) z-axis component, and Λ_k the figure-axis component. In this representation, the angular components of

$\vec{\mathbf{P}} + \vec{\mathbf{A}}$ couple states φ_k with different Λ_k but are diagonal in J, M_J, and a system of coupled radial equations arises for each J, which may be written as

$$\left\{\frac{1}{2\mu}\left[-i\frac{d}{dR} + \mathbf{P}^R + \mathbf{A}^R\right]^2 + \left[\frac{J(J+1)-\Lambda_k}{2\mu R^2}\right]\mathbf{1} + \frac{1}{2\mu}\left[\mathbf{D}-\mathbf{Q}\right]\right\} G_k^{JM_J}(R) = \left[\mathbf{1}E - \mathbf{U}(R)\right] G_k^{JM_J}(R), \quad \text{(B-14)}$$

where

$$D_{k'k} = (P^{\Theta}_{k'k} + A^{\Theta}_{k'k})^2 + (\widetilde{P}^{\Phi}_{k'k} + A^{\Phi}_{k'k})^2 \quad \text{(B-15)}$$

and

$$Q_{k'k} = \delta(\Lambda_{k'}, \Lambda_k \pm 1) R^{-1}[(J \mp \Lambda_k)(J \pm + \Lambda_k + 1)]^{1/2}[(P^{\Theta}_{k'k} + A^{\Theta}_{k'k}) \pm i(\widetilde{P}^{\Phi}_{k'k} + A^{\Phi}_{k'k})] \quad \text{(B-16)}$$

with

$$\widetilde{P}_{k'k} = R^{-1}\langle\varphi_k|\hat{L}_{x'}|\varphi_k\rangle. \quad \text{(B-17)}$$

The remainder of $\mathbf{P}^{\Phi}$ has been absorbed in the rotational kinetic energy. $\mathbf{Q}$ which couples states whose Λ values differ by ± 1, is the angular or "Coriolis" coupling; $\mathbf{D}$ is diagonal in $\Lambda(\Lambda_{k'} = \Lambda_k)$ and represents a small correction to the rotation kinetic energy.

Equations (B-14) can be reduced to a more conventional form,

$$\left\{\frac{1}{2\mu}\left[-i\frac{d}{dR} + \mathbf{P}^R + \mathbf{A}^R\right]^2 + \frac{K(K+1)}{2\mu R^2}\mathbf{1} + \frac{\sqrt{K(K+1)}}{\mu R}\left[\mathbf{P}^{\Theta} + \mathbf{A}^{\Theta}\right]\right\} \mathbf{G}(R) = \left[\mathbf{1}E - \mathbf{U}(R)\right] \mathbf{G}(R), \quad \text{(B-18)}$$

by taking into account that the angular momentum of heavy particles K is much greater than that of electron system (Λ), i.e., $K \approx J \gg \Lambda$.

BIBLIOGRAPHY

BIBLIOGRAPHY

[1] M. B. Shah, J. Geddes, B. M. McLaughlin, and H. B. Gilbody *J. Phys. B: At. Mol. Phys.*, vol. 31, p. L757, 1998.

[2] M. Pieksma, S. Y. Ovchinnikov, J. van Eck, W. B. Westerveld, and A. Niehaus *Phys. Rev. Lett.*, vol. 73, p. 46, 1994.

[3] E. Y. Sidky and C. D. Lin *Phys. Rev. A.*, vol. 65, p. 012711, 2001.

[4] N. Toshima *Phys. Rev. A.*, vol. 59, p. 1981, 1999.

[5] A. Kolakowska, M. S. Pindzola, and D. R. Schultz *Phys. Rev. A.*, vol. 59, p. 3588, 1999.

[6] M. Shah and H. B. Gilbody *J. Phys. B: At. Mol. Phys.*, vol. 14, p. 2361, 1981.

[7] M. Shah, D. S. Elliot, and H. B. Gilbody *J. Phys. B: At. Mol. Phys.*, vol. 20, p. 2481, 1987.

[8] M. Kimura and N. F. Lane *Adv. At. Mol. Opt. Phys.*, vol. 26, p. 79, 1990.

[9] H. P. Summers *Adv. At. Mol. Opt. Phys.*, vol. 33, p. 275, 1994.

[10] H. B. Gilbody *Adv. At. Mol. Opt. Phys.*, vol. 33, p. 149, 1994.

[11] C. J. Joachain and D. E. Post (editors), *Atomic and Molecular Physics of Controlled Thermonuclear Fusion.* New York, Plenum, 1982.

[12] R. K. Janev, "Summary report of iaea technical committe meeting on atomic and molecular data for fusion reactor technology." IAEA report INCD(NDS)-227, 1993.

[13] R. K. Janev, *Atomic and molecular processes in fusion edge plasmas.* Plenum Press, 1995.

[14] H. B. Gilbody, "Ion-atom collision measurements relevant to fusion plasmas," in *The Nineteenth Internayional Conference on the Physics of Electronic and Atomic Collisions* (L. J. Dubé *et al.*, ed.), p. 19, 1995.

[15] D. E. Post *J. Nucl. Mater.*, vol. 220-222, p. 143, 1995.

[16] R. J. Fonck, R. J. Goldston, R. Kaita, and D. E. Post *Appl. Phys. Lett.*, vol. 42, p. 239, 1983.

[17] K. Khlopenkov and S. Sudo *Plasma Phys. Control. Fusion*, vol. 43, p. 1547, 2001.

[18] A. V. Vinogradov and I. I. Sobel'man *Sov. Phys. JETP.*, vol. 36, p. 1115, 1973.

[19] R. C. Elton, *X-Ray Lasers.* Academic, 1990.

[20] F. V. Bunkin, V. I. Derziev, and S. I. Yakovlenko *Sov. J. Quantum Electron.*, vol. 11, p. 981, 1981.

[21] R. H. Dixon and R. C. Elton *Phys. Rev. Lett.*, vol. 38, p. 1977, 1072.

[22] H. J. Kunze, K. N. Koshelev, C. Steden, D. Uskov, and H. T. Wischebrink *Phys. Lett. A.*, vol. 193, p. 183, 1994.

[23] A. Engel, K. N. Koshelev, Y. V. Sidelnikov, S. S. Churilov, C. Gavrilescu, and R. Lebert *Phys. Rev. E.*, vol. 58, p. 7819, 1998.

[24] W. L. Fite, T. R. Brackmann, and W. R. Snow *Phys. Rev.*, vol. 112, p. 1161, 1958.

[25] D. Ciric, A. Brazuk, D. Dijkamp, F. J. de Heer, and H. Winter *J. Phys. B: At. Mol. Phys.*, vol. 18, p. 3629, 1985.

[26] G. J. Lockwood and E. Everhart *Phys. Rev.*, vol. 125, p. 567, 1962.

[27] J. T. Park, J. E. Aldag, and J. M. George *Phys. Rev. Lett.*, vol. 34, p. 1253, 1975.

[28] R. W. McCullough, F. G. Wilkie, and H. B. Gilbody *J. Phys. B: At. Mol. Phys.*, vol. 16, p. 1573, 1984.

[29] H. J. Kim and F. W. Meyler *Phys. Rev. A.*, vol. 26, p. 1310, 1982.

[30] J. H. Newman, J. D. COgan, J. D. Zeigler, D. L. Nitz, R. D. Rundel, K. A. Simth, and R. F. Stebbings *Phys. Rev. A.*, vol. 25, p. 2976, 1982.

[31] P. M. Koch and J. E. Bayfield *Phys. Rev. Lett.*, vol. 34, p. 448, 1975.

[32] B. H. Bransden and M. R. C. McDowell, *Charge Exchange and the Theory of Ion-Atom Collisions.* Oxford, 1992.

[33] D. R. Bates *Proc. R. Soc. Landon ser. A.*, vol. 245, p. 194, 1958.

[34] W. Fritsch and C. D. Lin *J. Phys. B: At. Mol. Phys.*, vol. 15, p. 1255, 1982.

[35] H. S. W. Massey and R. A. Smith *Proc. R. Soc. London ser. A*, vol. 142, p. 142, 1933.

[36] D. R. Bates and R. McCarroll *Proc. R. Soc. Landon ser. A.*, vol. 247, p. 175, 1958.

[37] M. Kimura and C. D. Lin *Phys. Rev. A.*, vol. 31, p. 590, 1985.

[38] M. Kimura and C. D. Lin *Phys. Rev. A.*, vol. 22, p. 1357, 1985.

[39] T. G. Winter and N. F. Lane *Phys. Rev. A.*, vol. 31, p. 2698, 1985.

[40] L. D. Landau *Phys. Z. Sow.*, vol. 1, p. 46, 1932.

[41] C. Zener *Proc. R. Soc. London, ser. A*, vol. 137, p. 696, 1932.

[42] N. Y. Demkov *Dokl. Akad. Nauk. S.S.S.R.*, vol. 166, p. 1076, 1966.

[43] H. Ryufuku and T. Watanabe *Phys. Rev. A.*, vol. 18, p. 2005, 1978.

[44] H. Ryufuku and T. Watanabe *Phys. Rev. A.*, vol. 19, p. 1838, 1979.

[45] H. Ryufuku and T. Watanabe *Phys. Rev. A.*, vol. 20, p. 1828, 1978.

[46] H. Ryufuku *Phys. Rev. A.*, vol. 25, p. 720, 1982.

[47] L. Preasnyakov and A. D. Ultantsev *Sov. J. Quantum Electron (Enhl. Trans.)*, vol. 4, p. 1320, 1975.

[48] L. Vainshtein, L. Presnyakov, and I. Sobel'man *Sov. Phys. JETP*, vol. 18, p. 1383, 1964.

[49] W. L. Fite, D. G. H. R. F. Stebbings, and R. T. Brackmann *Phys. Rev.*, vol. 119, p. 663, 1960.

[50] H. B. Gilbody and Ireland *Proc. R. Soc. Landon ser. A.*, vol. 277, p. 137, 1963.

[51] M. Shah, P. M. D. S. Elliot, and H. B. Gilbody *J. Phys. B: At. Mol. Opt. Phys.*, vol. 21, p. 2455, 1988.

[52] M. Pieksma, S. Y. Ovchinnikov, and J. H. Macek *J. Phys. B: At. Mol. Phys.*, vol. 31, p. 1267, 1998.

[53] B. M. Mclaughlin, T. G. Winter, and J. F. McCann *J. Phys. B: At. Mol. Phys.*, vol. 30, p. 1043, 1997.

[54] W. Fritsch and C. D. Lin *Phys. Rev. A.*, vol. 27, p. 3361, 1983.

[55] D. S. F. Crothers and J. F. McCann *J. Phys. B: At. Mol. Phys.*, vol. 16, p. 3229, 1983.

[56] S. Y. Zou, L. Pichl, M. Kimura, and T. Kato *Phys. Rev. A.*, vol. 66, p. 042707, 2002.

[57] R. E. Olson *Phys. Rev. A.*, vol. 27, p. 1871, 1983.

[58] W. Meckbach, P. J. Focke, A. R. Goni, S. Suarez, J. Macek, and M. G. Menendez *Phys. Rev. Lett.*, vol. 57, p. 1587, 1986.

[59] R. E. Olson, T. J. Gay, H. G. Berry, E. B. Hale, and V. B. Irby *Phys. Rev. Lett.*, vol. 59, p. 36, 1987.

[60] V. D. Irby, T. Gay, J. Edwards, E. Hale, M. McKenzie, and R. Olson *Phys. Rev. A.*, vol. 37, p. 3612, 1988.

[61] T. J. Gay, M. W. Gealy, and M. E. Rudd *J. Phys. B: At. Mol. Phys.*, vol. 23, p. L823, 1990.

[62] V. D. Irby, S. Datz, P. F. Ditmer, N. L. Jones, H. F. Krause, and C. R. Vane *Phys. Rev. A.*, vol. 47, p. 2957, 1993.

[63] G. Bernardi *et al. Phys. Rev. A.*, vol. 40, p. 6863, 1989.

[64] G. Bernardi, P. Fainstain, C. R. Garibotti, and S. Suarez *J. Phys. B: At. Mol. Phys.*, vol. 23, p. L139, 1990.

[65] W. Meckbach, S. Suarez, P. Focke, and G. Bernardi *J. Phys. B: At. Mol. Phys.*, vol. 24, p. 3763, 1991.

[66] S. Suarez *et al. Phys. Rev. A.*, vol. 48, p. 4339, 1993.

[67] R. D. DuBois *et al. Phys. Rev. A.*, vol. 48, p. 1123, 1993.

[68] R. D. DuBois *et al. Phys. Rev. A.*, vol. 50, p. 3071, 1994.

[69] T. G. Winter and C. D. Lin *Phys. Rev. A.*, vol. 29, p. 3071, 1984.

[70] T. Winter *Phys. Rev. A.*, vol. 37, p. 4556, 1988.

[71] L. F. Errea, C. Harel, C. Illescas, H. Jouin, L. Mendez, B. Pons, and A. Riera *J. Phys. B: At. Mol. Phys.*, vol. 31, p. 3199, 1998.

[72] E. Y. Sidky and C. D. Lin *Phys. Rev. A.*, vol. 60, p. 377, 1999.

[73] E. Y. Sidky, C. Illescas, and C. D. Lin *Phys. Rev. Lett.*, vol. 85, p. 1634, 2000.

[74] R. Dörner, H. Khemliche, M. Prior, C. Cocke, J. Gary, R. Olson, V. Mergel, J. Ullrich, and H. Schmidt-Bocking *Phys. Rev. Lett.*, vol. 77, p. 4520, 1996.

[75] M. Abdallah, C. Cocke, W. Wolff, H. Wolf, S. Kravis, M. Stockli, and E. Kamber *Phys. Rev. Lett.*, vol. 81, p. 3627, 1998.

[76] M. Abdallah, W. Wolff, H. Wolf, C. Cocke, and M. Stockli *Phys. Rev. A.*, vol. 58, p. R3379, 1998.

[77] F. Afaneh, R. Döner, L. Schmit, T. Weber, K. E. Stiening, O. Jagutzki, and H. Schmidt-Böcking *J. Phys. B: At. Mol. Phys.*, vol. 35, p. L229, 2000.

[78] V. SethuRaman, W. R. Thorson, and C. F. Lebeda *Phys. Rev. A.*, vol. 8, p. 1316, 1973.

[79] W. R. Thorson and J. B. Delos *Phys. Rev. A.*, vol. 18, p. 117, 1978.

[80] W. R. Thorson and J. B. Delos *Phys. Rev. A.*, vol. 18, p. 135, 1978.

[81] W. R. Thorson and G. Bandarage *Phys. Rev. A.*, vol. 37, p. 692, 1988.

[82] G. Bandarage and W. R. Thorson *Phys. Rev. A.*, vol. 37, p. 716, 1988.

[83] T. G. Winter and C. D. Lin *Phys. Rev. A.*, vol. 29, p. 567, 1984.

[84] J. Y. Kuang and C. D. Lin *J. Phys. B: At. Mol. Opt. Phys.*, vol. 29, p. 1207, 1996.

[85] J. Y. Kuang and C. D. Lin *J. Phys. B: At. Mol. Opt. Phys.*, vol. 29, p. 5443, 1996.

[86] G. J. N. Brown and D. S. F. Crothers, "On the efficacy of coupled-channel calculations in ion-atom collisions using continuum distorted-waves," in *The Twentieth Internayional Conference on the Physics of Electronic and Atomic Collisions* (F. Aumayr and H. Winter, eds.), p. 525, 1997.

[87] C. Illescas, I. Rabadan, and A. Riera *J. Phys. B: At. Mol. Opt. Phys.*, vol. 30, p. 1765, 1997.

[88] R. E. Olson and A. Salop *Phys. Rev. A.*, vol. 16, p. 531, 1977.

[89] R. E. Olson *Phys. Rev. A.*, vol. 18, p. 2464, 1978.

[90] G. Hose *Phys. Rev. A.*, vol. 56, p. 1364, 1997.

[91] D. R. Schultz, C. O. Reinhold, P. S. Krstic, and M. R. Strayer *Phys. Rev. A.*, vol. 65, p. 052722, 2001.

[92] D. R. Bates *et al Proc. R. Soc. Landon ser. A.*, vol. 216, p. 437, 1953.

[93] A. F. Ferguson *Proc. R. Soc. Landon ser. A.*, vol. 264, p. 540, 1961.

[94] A. F. Ferguson and R. McCarrol *Proc. R. Soc. Landon ser. A.*, vol. 264, p. 547, 1961.

[95] S. B. Schneidermann and A. Russek *Phys. Rev.*, vol. 181, p. 311, 1969.

[96] J. B. Delos *Rev. Mod. Phys.*, vol. 53, p. 287, 1981.

[97] G. Hunter and H. O. Pritchard *J. Chem. Phys.*, vol. 46, p. 2146, 1967.

[98] J. Rankin and W. R. Thorson *J. Comput. Phys.*, vol. 32, p. 437, 1979.

[99] D. Kleppner *Phys. Today*, vol. 52, p. 11, 1999.

[100] W. R. Thorson, J. H. C. M. Kimura, and S. K. Knudson *Phys. Rev. A.*, vol. 24, p. 1768, 1981.

[101] M. Kimura and W. R. Thorson *Phys. Rev. A.*, vol. 24, p. 1780, 1981.

[102] J. Rankin and W. R. Thorson *Phys. Rev. A.*, vol. 18, p. 1990, 1978.

[103] C. F. barnett *Oak ridge national Laboratory Report*, vol. 6086, p. 1, 1990.

[104] T. J. Morgan, J. Stone, and R. Mayo *Phys. Rev. A.*, vol. 22, p. 1460, 1980.

[105] M. Kimura and W. R. Thorson *Phys. Rev. A.*, vol. 24, p. 3019, 1981.

[106] R. Hoekstra, A. R. Schlatmann, F. J. de Heer, and R. Morgenstern *J. Phys. B: At. Mol. Opt. Phys.*, vol. 22, p. L603, 1989.

[107] R. Hoekstra, F. J. de Heer, and R. Morgenstern *J. Phys. B: At. Mol. Opt. Phys.*, vol. 24, p. 4025, 1991.

[108] D. Ciric, D. Dijkamp, E. Vlieg, and F. J. de Heer *J. Phys. B: At. Mol. Opt. Phys.*, vol. 18, p. L17, 1985.

[109] L. F. Errea, J. M. Gomez-Llorente, L. Méndez, and A. Riera *J. Phys. B: At. Mol. Opt. Phys.*, vol. 20, p. 6089, 1987.

[110] K. Rinn, F. Melchert, and E. Salzborn *J. Phys. B: At. Mol. Phys.*, vol. 18, p. 3783, 1985.

[111] K. Kondo and K. Ida *et al. J. Nucl. Mater*, vol. 241-243, p. 956, 1997.

[112] M. G. von Hellermann and W. Mandl, *et al. Rev. Sci. Instrum.*, vol. 61, p. 3479, 1990.

[113] K. Ida, S. Kado, and Y. Liang *Rev. Sci. Instrum.*, vol. 71, p. 2360, 2000.

[114] E. C. Eisner and W. L. Rowan *Rev. Sci. Instrum.*, vol. 72, p. 1004, 2001.

[115] J. Baldzuhn and W. Ohlendorf *Rev. Sci. Instrum.*, vol. 68, p. 1020, 1997.

[116] S. Sudo, N. Tamura, K. Khlopenkov, S. Muto, H. Funaba, I. Viniar, V. Sergeev, K. Sato, K. Ida, K. Kawahata, A. Komori, K. Matsuoka, K. Narihara, S. Okamura, N. Ohyabu, K. Tanaka, and O. Motojima *Plasma Phys. Control. Fusion*, vol. 44, p. 129, 2002.

[117] H. P. Summers *Mon. Not. R. Astron. Soc.*, vol. 178, p. 101, 1977.

[118] J. Spence and H. P. Summers *J. Phys. B: At. Mol. Opt.*, vol. 19, p. 3749, 1986.

[119] T. Fujimoto *J. Phys. Soc. Jpn.*, vol. 47, p. 265, 1979.

[120] T. Fujimoto *J. Phys. Soc. Jpn.*, vol. 47, p. 272, 1979.

[121] T. Fujimoto *J. Phys. Soc. Jpn.*, vol. 49, p. 1561, 1979.

[122] T. Fujimoto *J. Phys. Soc. Jpn.*, vol. 49, p. 1569, 1980.

[123] T. Fujimoto *J. Phys. Soc. Jpn.*, vol. 54, p. 2905, 1985.

[124] R. Mewe *Astron. Astrophys.*, vol. 20, p. 215, 1972.

[125] V. Shevelko and L. Vainshtein, *Atomic physics for hot plasmas.* Institute of Physics Pub., 1993.

[126] "The relativistic multiconfinguration hebrew university lawrence livermore atomic code (hullac)."

[127] E. H. Clark and J. Abdallah *Jr, Phys. Scr.*, vol. T62, p. 7, 1996.

[128] N. R. Badnell and T. W. Gorczyca *J. Phys. B: At. Mol. Opt. Phys.*, vol. 30, p. 2011, 1997.

[129] S. Zou, T. Kato, and I. Murakami *NIFS DATA*, vol. 69, p. 1, 2001.

[130] S. Zou, T. Kato, and I. Murakami *J. Phys. Soc. Jpn*, vol. 72, p. ****, 2003.

[131] V. L. Jacobs and J. Davis *Phys. Rev. A.*, vol. 18, p. 697, 1978.

[132] W. Lotz *Physik*, vol. 216, p. 1679, 1968.

[133] A. Burgess *Mem. R. Astron. Soc.*, vol. 69, p. 1, 1964.

[134] N. Toshima and H. Tawara *NIFS DATA*, vol. 26, p. 1, 1995.

[135] M. Aubert, N. Bessis, and G. Bessis *Phys. Rev. A.*, vol. 10, p. 51, 1974.

[136] D. R. Bates and T. R. Carson *Proc. Roy. Soc. Lond. A.*, vol. 234, p. 207, 1956.

[137] K. Helfrich and H. Hartmann *Theor. Chem. Acta.*, vol. 16, p. 263, 1970.

[138] T. G. Winter, M. D. Duncan, and N. F. Lane *J. Phys. B: At. Mol. Phys.*, vol. 10, p. 285, 1977.

[139] L. I. Ponomarev and L. N. Somov *J. Comput. Phys.*, vol. 20, p. 183, 1976.

[140] A. Ainsworth *et al. Plasma Phys. Control. Fusion*, vol. 28, p. 1211, 1986.

[141] J. Baldzuhn, H. M. M. Kick, and the W7-AS Team *Plasma Phys. Control. Fusion*, vol. 40, p. 967, 1998.

[142] D. R. Bates and R. McCarroll *Adv. Phys.*, vol. 11, p. 39, 1962.

[143] A. Boileau, M. V. Hellermann, L. D. Horton, J. Spence, and H. P. Summers *Plasma Phys. Control. Fusion*, vol. 31, p. 779, 1989.

[144] J. F. Bonnal, G. Bracco, C. Breton, C. de. Michelis, J. Bruaux, M. Mattioli, R. Oberson, and J. Ramette *J. Phys. D: Appl. Phys.*, vol. 15, p. 805, 1982.

[145] E. Busche, H. Euringer, and R. Jaspers *Plasma Phys. Control. Fusion*, vol. 39, p. 1327, 1997.

[146] J. B. Coorks and M. E. Rudd *Phys. Rev. Lett.*, vol. 25, p. 1599, 1970.

[147] S. Cvejanovic and F. H. Raed *J. Phys. B: At. Mol. Phys.*, vol. 7, p. 1841, 1974.

[148] D. H. Drawin *Phys. Repoerts*, vol. 37, p. 125, 1978.

[149] L. F. Errea, L. Méndez, and A. Riera *J. Phys. B: At. Mol. Phys.*, vol. 15, p. 101, 1982.

[150] L. F. Errea, C. Harel, H. Jouin, L. Méndez, B. pons, and A. Riera *J. Phys. B: At. Mol. Phys.*, vol. 27, p. 3603, 1994.

[151] F. Engelmann and A. Nocentini *Nucl. Fusion*, vol. 17, p. 995, 1977.

[152] M. Fujiwara *et al. Nucl. Fusion*, vol. 41, p. 1355, 2001.

[153] A. Gibson *Nucl. Fusion*, vol. 16, p. 546, 1976.

[154] W. R. Hess, J. L. Farjon, and R. Guirlet *Rev. Sci. Instrum.*, vol. 73, p. 1775, 2002.

[155] E. Hinnov and M. Matioli *Phys. Lett. A.*, vol. 66, p. 109, 1978.

[156] J. T. Hogan and H. C. Howe *J. Nucl. Matter.*, vol. 63, p. 561, 1976.

[157] J. Hogan *Phys. Reports*, vol. 37, p. 83, 1978.

[158] R. C. Isler, R. V. Neidigh, and R. D. Cowan *Phys. Lett. A.*, vol. 63, p. 295, 1977.

[159] R. C. Isler and E. C. Crume *Phys. Rev. Lett.*, vol. 41, p. 1296, 1978.

[160] D. Kato and S. Watanabe *Phys. Rev. A.*, vol. 56, p. 3687, 1997.

[161] Y. K. Kim and M. E. Rudd *Phys. Rev. A.*, vol. 50, p. 3954, 1994.

[162] H. Klar *Z. Phys. A.*, vol. 30, p. 75, 1982.

[163] S. Kravis *et al. Phys. Rev. A.*, vol. 54, p. 1394, 1996.

[164] J. Y. Kuang and C. D. Lin *J. Phys. B: At. Mol. Opt. Phys.*, vol. 30, p. 101, 1997.

[165] J. H. Macek *Phys. Rev. A.*, vol. 1, p. 235, 1970.

[166] J. H. Macek and S. Y. Ovchinnikov *Phys. Rev. Lett.*, vol. 80, p. 2298, 1998.

[167] W. Mandl, K. Burrell, R. Groebner, J. Kim, R. Seraydarian, M. Wade, and J. Scoville *Nucl. Fusion*, vol. 35, p. 347, 1995.

[168] C. McCaig and D. S. F. Crothers *J. Phys. B: At. Mol. Phys.*, vol. 33, p. 3555, 2000.

[169] R. McCarroll and D. S. F. Crothers *Adv. At. Mol. Opt. Phys.*, vol. 32, p. 253, 1994.

[170] D. M. Meade *Nucl. Fusion*, vol. 14, p. 289, 1974.

[171] A. M. Messian *et al. Plasma Phys. Control. Fusion*, vol. 35, p. A15, 1993.

[172] M. Nagami *Rept. JAERI-M*, vol. Dec, p. 7432, 1977.

[173] S. Y. Ovchinnikov and J. H. Macek *Phys. Rev. Lett.*, vol. 75, p. 2474, 1995.

[174] J. T. Park, J. E. Aldag, J. M. George, J. L. Peacher, and J. H. McGuire *Phys. Rev. A.*, vol. 15, p. 508, 1977.

[175] J. T. Park *Adv. At. Mol. Opt. Phys.*, vol. 19, p. 67, 1983.

[176] L. I. Ponomarev and S. I. Vinitsky *J. Phys. B: At. Mol. Phys.*, vol. 12, p. 567, 1979.

[177] L. I. Ponomarev, S. I. Vinitsky, and F. R. Vukajlovic *J. Phys. B: At. Mol. Phys.*, vol. 13, p. 847, 1980.

[178] L. I. Ponomarev, L. N. Somov, and F. R. Vukajlovic *J. Phys. B: At. Mol. Phys.*, vol. 14, p. 591, 1981.

[179] R. F. Post *Plasma. Phys.*, vol. 3, p. 273, 1961.

[180] D. E. Post, R. V. Jensen, C. B. Tarter, W. H. Grasberger, and W. A. Lokke *Plasma. Phys.*, vol. 3, p. 273, 1961.

[181] M. E. Rudd, Y. K. Kim, D. H. Madison, and J. W. Gallagher *Rev. Mod. Phys.*, vol. 57, p. 965, 1985.

[182] M. E. Rudd, Y. K. Kim, D. H. Madison, and T. J. Gay *Rev. Mod. Phys.*, vol. 64, p. 441, 1992.

[183] M. Shah, D. S. Elliot, and H. B. Gilbody *J. Phys. B: At. Mol. Phys.*, vol. 20, p. 3501, 1987.

[184] A. Samain and F. Werkoff *Nucl. Fusion*, vol. 17, p. 53, 1977.

[185] R. P. Schorn, E. Wolfrum, F. Aumayr, E. Hintz, H. Rusbüldt, and H. Winter *Nucl. Fusion*, vol. 32, p. 35, 1992.

[186] G. Wannier *Phys. Rev.*, vol. 90, p. 817, 1953.

[187] D. Whyte, M. Wade, D. Finkenthal, K. Burrell, P. Monier-Garbet, B. Rice, D. Schissel, W. West, and R. Wood *Nucl. Fusion*, vol. 38, p. 387, 1998.

[188] R. Wilhelm *Plasma Phys. Control. Fusion*, vol. 40, p. A1, 1998.

[189] H. Vernickl and J. Bohdanski *Nucl. Fusion*, vol. 18, p. 1467, 1977.